

N69-17947  
NASA CR-73955

NATIONAL AERONAUTICS AND SPACE ADMINISTRATION

*Space Programs Summary 37-54, Vol. II*

*The Deep Space Network*

For the Period September 1 to October 31, 1968

**CASE FILE  
COPY**

**JET PROPULSION LABORATORY  
CALIFORNIA INSTITUTE OF TECHNOLOGY  
PASADENA, CALIFORNIA**

November 30, 1968

NATIONAL AERONAUTICS AND SPACE ADMINISTRATION

*Space Programs Summary 37-54, Vol. II*

*The Deep Space Network*

For the Period September 1 to October 31, 1968

JET PROPULSION LABORATORY  
CALIFORNIA INSTITUTE OF TECHNOLOGY  
PASADENA, CALIFORNIA

November 30, 1968

**SPACE PROGRAMS SUMMARY 37-54, VOL. II**

Copyright © 1969  
Jet Propulsion Laboratory  
California Institute of Technology  
Prepared Under Contract No. NAS 7-100  
National Aeronautics and Space Administration

## Preface

The Space Programs Summary is a multivolume, bimonthly publication that presents a review of technical information resulting from current engineering and scientific work performed, or managed, by the Jet Propulsion Laboratory for the National Aeronautics and Space Administration. The Space Programs Summary is currently composed of four volumes:

- Vol. I. *Flight Projects* (Unclassified)
- Vol. II. *The Deep Space Network* (Unclassified)
- Vol. III. *Supporting Research and Advanced Development* (Unclassified)
- Vol. IV. *Flight Projects and Supporting Research and Advanced Development* (Confidential)

## Foreword

Volume II of the *Space Programs Summary* reports the results of work performed by the Deep Space Network (DSN). Information is presented, as appropriate, in the following categories:

### Introduction

- Description of the DSN
- Description of DSN Systems

### Mission Support

- Introduction
- Interplanetary Flight Projects
- Planetary Flight Projects
- Manned Space Flight Project

### Advanced Engineering

- Tracking and Navigational Accuracy Analysis
- Communications Systems Research
- Tracking and Data Acquisition Elements Research
- Supporting Research

### Network Development and Operations

#### Facility Development and Operations

- Space Flight Operations Facility
- Ground Communications Facility
- Deep Space Instrumentation Facility

#### Design and Implementation of Technical Structures and Utilities

In each issue, the section entitled "Description of DSN Systems" reports the current configuration of one of the six DSN systems (tracking, telemetry, command, monitoring, simulation, and operations control). The fundamental research carried out in support of the DSN is reported in Vol. III.

# Contents

<b>I. Introduction</b>	1
A. Description of the DSN	1
B. Description of DSN Systems: Simulation System <i>H. C. Thorman</i>	3
<b>II. Mission Support</b>	8
A. Introduction	8
B. <i>Mariner Mars 1971 Missions</i> <i>D. J. Mudgway</i>	9
C. <i>Mariner V Extended Mission Operations</i> <i>D. J. Mudgway</i>	11
<b>III. Advanced Engineering:</b>	
<b>Tracking and Navigational Accuracy Analysis</b>	13
A. Introduction <i>T. W. Hamilton and D. W. Trask</i>	13
B. High-Resolution Gravimetric Map of the Mare Imbrium Region <i>P. M. Muller and W. L. Sjogren</i>	14
C. Continuous Estimation of the State of a Distant Spacecraft During Successive Passes of Data: Twin Tracking Station Results <i>J. F. Jordan</i>	16
D. Dynamic Programming Approach to Optimal Stochastic Orbit-Transfer Strategy <i>T. Nishimura</i>	21
E. Some Numerical Results Using the Multirevolution Integration Program LEAP <i>D. Boggs and R. Leavitt</i>	27
<b>IV. Advanced Engineering:</b>	
<b>Communications System Research</b>	31
A. Phase Jitter Measurement of Programmed Oscillators <i>R. F. Emerson</i>	31
B. Computer Interrupter <i>L. C. Constenla</i>	34
<b>V. Advanced Engineering:</b>	
<b>Tracking and Data Acquisition Elements Research</b>	36
A. High-Vacuum Evaporation Techniques for Thick Metallic Film Deposition on Large Cylinders <i>H. Erpenbach and C. Finnie</i>	36
B. Broadband Microwave Waveguide Window <i>C. T. Stelzried, D. L. Mullen, and J. C. Chavez</i>	39

## Contents (contd)

C. Noise Temperatures of a Receiving System Containing Mismatched Two-Port Networks <i>T. Y. Otoshi</i>	42
D. Operating Noise Temperature Calibrations of the JPL Research Cones <i>C. T. Stelzried</i>	46
E. JPL System Checkout of S-Band Multifrequency Cone (SMF SN1 Mod 1) <i>C. T. Stelzried, T. Y. Otoshi, and K. B. Wallace</i>	48
<b>VI. Advanced Engineering:</b>	
<b>Supporting Research</b>	56
A. 210-ft Antenna Primary Reflector Structure Distortions Due to Thermal Differences and Wind Loadings <i>M. S. Katow</i>	56
B. Survey Technique for the 210-ft Antenna Azimuth Bull Gear <i>W. R. Bollinger, S. R. Paine, and C. C. Valencia</i>	58
C. Electron-Beam Welding Test for Large Hydrostatic Bearing Runner Plates <i>C. J. McCaul, H. P. Phillips, and R. A. Zanteson</i>	62
D. Voltage-Controlled Phase Shifter <i>C. E. Johns</i>	63
E. Venus DSS Activities <i>R. M. Gosline, M. A. Gregg, and E. B. Jackson</i>	66
F. 500-kW Motor-Generator for X-Band Time Synchronization Transmitter <i>R. E. Arnold</i>	67
<b>VII. Network Development and Operations</b>	71
A. High-Rate Telemetry Project <i>R. C. Tausworthe</i>	71
B. Test Equipment <i>R. I. Greenberg</i>	71
C. Digital Equipment <i>H. C. Wilck</i>	72
D. Software Teletype Output Routines <i>P. H. Schottler</i>	74
E. System Verification Tests <i>R. W. Burt</i>	77
F. Effect of Variation in Subcarrier Loop Parameters on Telemetry Subcarrier Demodulator Performance <i>M. H. Brockman</i>	77
<b>VIII. DSIF Development and Operations</b>	82
A. Time-Synchronization System Performance <i>H. W. Baugh</i>	82
B. Station Control and Data Equipment <i>E. Bann, A. Burke, J. Woo, D. Hersey, and P. Harrison</i>	84

## Contents (contd)

C. Rapid Generation of Monitor Criteria Data	
<i>M. Thomas</i> . . . . .	85
D. DIS Monitor Calibration Computer Program	
<i>W. Roach and T. Lewis</i> . . . . .	86
E. Fiber Optics Boresight Telescope	
<i>C. Lundy and F. Stoller</i> . . . . .	89
F. Theoretical Phase Characteristics of Klystron Amplifiers	
<i>R. L. Leu</i> . . . . .	91
G. 500-kW Klystron Development	
<i>C. P. Wiggins</i> . . . . .	93
H. Traveling-Wave Tube Amplifier	
<i>B. W. Harness</i> . . . . .	94
I. Equipment Maintenance Facilities	
<i>R. Smith</i> . . . . .	96
J. Workmanship Assurance Program	
<i>R. Durham</i> . . . . .	97
<b>IX. Development and Implementation of Technical Structures and Utilities</b> . . . . .	98
A. Cebreros DSS Antenna Reflector Damage and Repair	
<i>V. B. Lobb</i> . . . . .	98
B. Pioneer DSS Antenna Mechanical Upgrade	
<i>J. Carpenter and J. Carlucci</i> . . . . .	102

# 1. Introduction

## A. Description of the DSN

The Deep Space Network (DSN), established by the NASA Office of Tracking and Data Acquisition under the system management and technical direction of JPL, is responsible for two-way communications with unmanned spacecraft traveling approximately 10,000 mi from earth to interplanetary distances. It supports, or has supported, the following NASA deep space exploration projects: *Ranger*, *Surveyor*, *Mariner Venus 1962*, *Mariner Mars 1964*, *Mariner Venus 67*, *Mariner Mars 1969*, *Mariner Mars 1971*, and *Mariner V* extended mission operations (JPL); *Lunar Orbiter* (Langley Research Center); *Pioneer* (Ames Research Center); and *Apollo* (Manned Spacecraft Center), as backup to the Manned Space Flight Network (MSFN). The DSN is distinct from other NASA networks such as the MSFN, which has primary responsibility for tracking the manned spacecraft of the *Apollo* Project, and the Space Tracking and Data Acquisition Network (STADAN), which tracks earth-orbiting scientific and communications satellites. With no future unmanned lunar spacecraft presently planned, the primary objective of the DSN is to continue its support of planetary and interplanetary flight projects. Future activities may include support of certain foreign deep-space flight projects.

To provide this support of flight projects, the DSN simultaneously performs advanced engineering on components and systems, integrates proven equipment and methods into the network,<sup>1</sup> and performs the following three basic functions in direct support of the flight projects through radio communications with spacecraft:

- (1) *Tracking*: locating the spacecraft; measuring its distance, velocity, and position; and following its course.
- (2) *Data acquisition*: recovering information from the spacecraft in the form of telemetry, namely, engineering measurements and scientific data.
- (3) *Command*: sending coded signals to the spacecraft to activate equipment to initiate spacecraft functions.

To accomplish these functions, six DSN systems have been established: (1) tracking, (2) telemetry, (3) command, (4) monitoring, (5) simulation, and (6) operations control.

---

<sup>1</sup>When a new piece of equipment or new method has been accepted for integration into the network, it is classed as Goldstone duplicate standard (GSDS), thus standardizing the design and operation of identical items throughout the network.

The DSN can be characterized as being comprised of three facilities: the Deep Space Instrumentation Facility (DSIF), the Ground Communications Facility (GCF), and the Space Flight Operations Facility (SFOF).

## 1. Deep Space Instrumentation Facility

*a. Tracking and data acquisition facilities.* A world-wide set of deep space stations (DSSs) with large antennas, low-noise phase-lock receiving systems, and high-power transmitters provide radio communications with spacecraft. The DSSs and the deep space communications complexes (DSCCs) they comprise are given in Table 1.

Radio contact with a spacecraft usually begins when the spacecraft is on the launch vehicle at Cape Kennedy, and it is maintained throughout the mission. The early part of the trajectory is covered by selected network stations of the Air Force Eastern Test Range (AFETR) and the MSFN of the Goddard Space Flight Center.<sup>2</sup> Normally, two-way communications are established between the spacecraft and the DSN within 30 min after the spacecraft has been injected into lunar, planetary, or interplanetary flight. A compatibility test station at Cape Kennedy (discussed later) monitors the spacecraft continuously dur-

ing the launch phase until it passes over the local horizon. The deep space phase begins with acquisition by either the Johannesburg, Woomera, or Tidbinbilla DSS. These and the remaining DSSs given in Table 1 provide radio communications to the end of the flight.

To enable continuous radio contact with spacecraft, the DSSs are located approximately 120 deg apart in longitude; thus, a spacecraft in deep space flight is always within the field-of-view of at least one station, and for several hours each day may be seen by two stations. Furthermore, since most spacecraft on deep space missions travel within 30 deg of the equatorial plane, the DSSs are located within latitudes of 45 deg north or south of the equator. All DSSs operate at S-band frequencies: 2110–2120 MHz for earth-to-spacecraft transmission and 2290–2300 MHz for spacecraft-to-earth transmission.

To provide sufficient tracking capability to enable useful data returns from around the planets and from the edge of the solar system, a 210-ft-diam-antenna network will be required. Two additional 210-ft-diam-antenna DSSs are being established at Madrid and Canberra, starting in 1969. These DSSs, scheduled to be operational by early-1973, will operate in conjunction with the Mars DSS to provide this capability.

*b. Compatibility test facilities.* In 1959, a mobile L-band compatibility test station was established at Cape Kennedy to verify flight-spacecraft/DSN compatibility prior to the launch of the *Ranger* and *Mariner* Venus 1962

<sup>2</sup>The 30-ft-diam-antenna station established by the DSN on Ascension Island during 1965 to act in conjunction with the MSFN orbital support 30-ft-diam-antenna station was transferred to the MSFN in July 1968.

Table 1. Tracking and data acquisition stations of the DSIF

DSCC	Location	DSS	Antenna		Year of initial operation
			Diameter, ft	Type of mounting	
Goldstone	California	Pioneer	85	Polar	1958
		Echo <sup>a</sup>	85	Polar	1962
		(Venus) <sup>b</sup>	(85)	(Az–El)	(1962)
		Mars	210	Az–El	1966
Canberra	Australia	Woomera <sup>c</sup>	85	Polar	1960
		Tidbinbilla <sup>c</sup>	85	Polar	1965
—	South Africa	Johannesburg <sup>c</sup>	85	Polar	1961 <sup>d</sup>
Madrid	Spain	Robledo <sup>c</sup>	85	Polar	1965
		Cebreros <sup>c</sup>	85	Polar	1967

<sup>a</sup>Established in 1959 to support NASA's Echo Project to explore the feasibility of transcontinental two-way communications using a passive satellite; the Echo DSS was originally configured with an 85-ft-diam Az–El-mounted antenna. In 1962, when the need arose for a second 85-ft-diam polar-mounted antenna at the Goldstone site, the 85-ft-diam Az–El-mounted antenna was moved to the Venus DSS, and an 85-ft-diam polar-mounted antenna was constructed at the Echo DSS.

<sup>b</sup>A research-and-development facility used to demonstrate the feasibility of new equipment and methods to be integrated into the operational network. Besides the 85-ft-diam Az–El-mounted antenna, the Venus DSS has a 30-ft-diam Az–El-mounted antenna that is used for testing the design and operation of the feed system for the Mars DSS 210-ft-diam antenna.

<sup>c</sup>Normally staffed and operated by government agencies of the respective countries (except for a temporary staff at the Madrid DSCC), with some assistance of U.S. support personnel.

<sup>d</sup>Between 1958 and 1962, a temporary mobile tracking station was located near Johannesburg to provide L-band communications required by the *Ranger* and *Mariner* Venus 1962 spacecraft.

spacecraft. Experience revealed the need for a permanent facility at Cape Kennedy for this function. An S-band compatibility test station with a 4-ft-diam antenna became operational in 1965. In addition to supporting the preflight compatibility tests, this station monitors the spacecraft continuously during the launch phase until it passes over the local horizon.

Spacecraft telecommunications compatibility in the design and prototype development phases was formerly verified by tests at the Goldstone DSCC. To provide a more economical means for conducting such work and because of the increasing use of multiple-mission telemetry and command equipment by the DSN, a compatibility test area was established at JPL in 1968. In all essential characteristics, the configuration of this facility is identical to that of the 85- and 210-ft-diam-antenna stations.

The JPL compatibility test area is used during spacecraft system tests to establish the compatibility with the DSN of the proof test model and developmental models of spacecraft, and the Cape Kennedy compatibility test station is used for final flight spacecraft compatibility validation testing prior to launch.

## **2. Ground Communications Facility**

The GCF, using, in part, facilities of the worldwide NASA Communications Facility (NASCOM),<sup>3</sup> provides voice, high-speed data, and teletype communications between the SFOF and all DSSs, except those of the Goldstone DSCC. Communications between the Goldstone DSCC and the SFOF are provided by a microwave link leased from a common carrier. Early missions were supported with voice and teletype circuits only, but increased data rates necessitated the use of wide-band circuits from all DSSs.

## **3. Space Flight Operations Facility**

Network and mission control functions are performed by the SFOF at JPL. (Prior to 1964, these functions were performed in temporary facilities at JPL.) The SFOF receives data from all DSSs and processes that information required by the flight project to conduct mission operations. The following services are provided: (1) real-time processing and display of tracking data; (2) real-time and non-real-time processing and display of telemetry data; (3) simulation of flight operations; (4) near-real-time evaluation of DSN performance; (5) operations control, and status and operational data display; and (6) general

support such as internal communications by telephone, intercom, public address, closed-circuit TV, documentation, and reproduction of data packages. Master data records of science data received from spacecraft are generated. Technical areas are provided for flight project personnel who analyze spacecraft performance, trajectories, and generation of commands.

The SFOF is equipped to support many spacecraft in flight and those under test in preparation for flight. Over a 24-hour period in 1967, as many as eight in-flight spacecraft or operational-readiness tests for flight were supported by the SFOF.

## **B. Description of DSN Systems: Simulation System, H. C. Thorman**

### **1. Function**

The DSN simulation system serves to generate and insert into the DSN simulated tracking, telemetry, and system checkout support data to prepare DSN and flight project personnel for the successful support of mission operations.

### **2. System Elements**

The data-flow capabilities provided by the simulation system are shown in Fig. 1. The heart of the system is the simulation data conversion center (SDCC), which includes an ASI 6050 computer, associated input/output devices, special operations consoles for controlling the simulation data, teletype equipment, and tape recorders. Elements of the GCF are used to route and process data for distribution to the SFOF and/or the DSIF.

Each DSS is provided with an FR 1200 tape recorder used to play back telemetry simulation tapes for insertion into the telemetry data stream. For a particular flight project, mission-dependent equipment may be provided at the DSS to process the simulation data prior to insertion into the data stream. At several DSSs (Echo, Woomera, Johannesburg, and Cebreros), the capability exists to receive high-speed data in real time from the SDCC (via the DSIF/GCF interface of the DSIF communications terminal subsystem) for insertion into the data stream and return to the SFOF. The points at which simulated data may be entered into the data stream are listed in Table 2 and illustrated in Fig. 1. Once inserted, the simulated data are identical in format to the real data and may be processed and routed in the usual manner by the components of the telemetry or tracking system.

<sup>3</sup>Managed and directed by the Goddard Space Flight Center.

**Table 2. DSN simulation system data insertion information<sup>a</sup>**

Insertion point	Insertion data type/source	Output data type/destination
<b>Deep Space Instrumentation Facility—telemetry data</b>		
(1) DSS receiver/exciter subsystem	RF carrier modulated by mission-dependent-equipment subcarrier simulator, with PCM data stream from DSIF/GCF interface or analog tape	Data streams into telemetry processor
(2) DSS telemetry and command subsystem	Data streams from DSIF/GCF interface or analog tape via integrator of mission-dependent-equipment simulator	(a) ADSS data blocks to DSIF communications terminal subsystem for transmission to SFOF (b) Teletype to DSIF communications terminal subsystem for transmission to SFOF
<b>Ground Communications Facility—telemetry data</b>		
(1) GCF SFOF communications terminal subsystem	(a) ADSS formatted blocks of spacecraft telemetry from simulation data conversion center (b) Same as (a), plus DSS function data	(a) Modulated data for high-speed transmission to DSIF (b) Modulated data for insertion into SFOF data processing system
(2) Transmit modem of SDCC communications terminal	EDED-like output from simulation data conversion center	SFOF data-processing-system-compatible telemetry data stream plus DSS function data
(3) Communications processor of GCF SFOF communications terminal subsystem	Teletype data directly from ASI 6050 computer in simulation data conversion center	Teletype to page printers of GCF SFOF internal communications and to user areas in SFOF
<b>Ground Communications Facility—tracking data</b>		
(1) Tape readers of GCF DSIF communications terminal subsystem	Baudot-coded punched paper tape	Teletype to SFOF via GCF
(2) Input communications processor of GCF SFOF communications terminal subsystem	Teletype data from punched paper tape or directly from ASI 6050 computer	Teletype to SFOF data processing system and teletype page printers of GCF SFOF internal communications
<b>Space Flight Operations Facility—telemetry data</b>		
(1) IBM 7044 data communications channel	SFOF data-processing-system-compatible telemetry and DSS function data	Normal SFOF data-processing-system output

<sup>a</sup>ADSS: automatic data switching system, EDED: error detector/encoder-decoder, and PCM: pulse-code-modulated.

Procedures-training for DSIF personnel is conducted in the JPL compatibility test area, which has the same capabilities as the DSSs except that the data from the SDCC are received in PCM bit-stream form via direct cable pairs. The primary function of the compatibility test area is that of receiving live data from the JPL spacecraft assembly facility and entering them into the GCF via the high-speed data line.

### 3. System Operation

An executive-type program (SIMSYS) in the ASI 6050 computer provides modular, mission-independent functions such as console input/output, commutation, and teletype formatting. Either tracking or telemetry simulation data may be produced by taking advantage of the program blocks available in SIMSYS. At present, tracking and telemetry data cannot be produced simultaneously.

The tracking data program is mission-independent, and telemetry programs are mission-dependent. However, uti-

lizing SIMSYS and the modular structure of the existing mission-dependent telemetry program, new spacecraft telemetry programs can be produced more easily by modifying existing programs.

*a. Tracking data.* Simulated tracking data are produced by first running the mission-dependent orbit determination program, which produces a tape containing simulated ephemeris data points for a given period. This tape is then used as the input to an ASI 6050 computer program controlled from the operator's console. The program produces formatted tracking data for up to four DSSs, with the additional capabilities of adding a variable amount of noise and/or bias to the data and realistically simulating one-, two-, and three-way doppler data. The teletype output of the ASI 6050 computer program is normally inserted directly into the SFOF communications processor for use in real time by the flight path analysis and control team, but it may be stored on paper tapes for playback at the SDCC or a DSS.

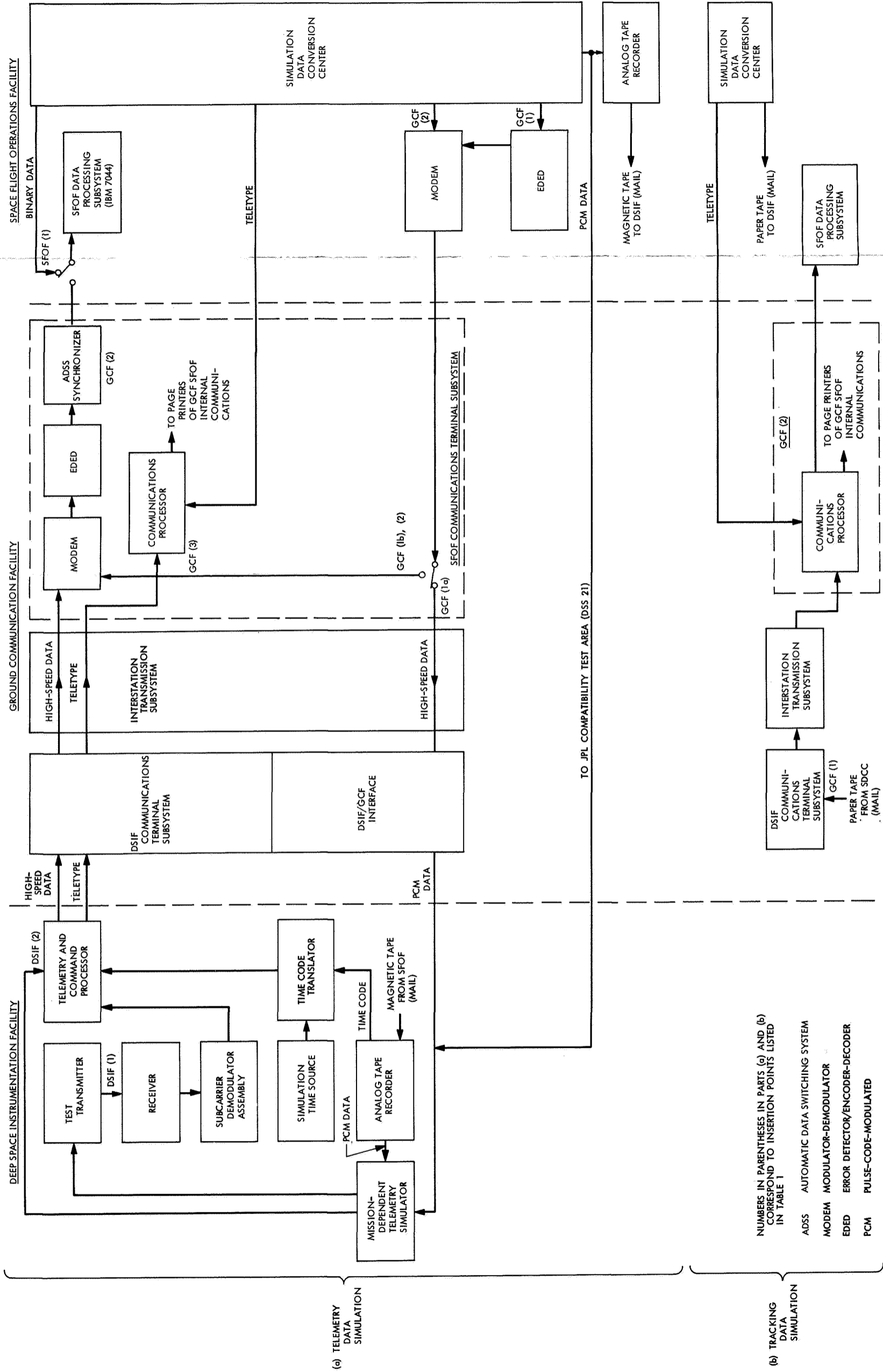


Fig. 1. DSN simulation system data-flow diagram



As backup for use when the ASI 6050 computer is being used for telemetry data simulation, a program exists for operation on the SFOF data processing system IBM 7094 computer that also ultimately produces paper tapes for playback at a DSS or the SDCC. This program (SIM 94) utilizes a save-tape from the PREDIX program and produces a digital magnetic tape. The content of the digital tape is, in turn, converted to paper-tape form by a special translation device.

**b. Telemetry data.** Several programs currently exist for the generation of mission-dependent engineering and science telemetry data streams. One reads spacecraft data analog recordings and simulates the teletype output of the telemetry and command processor at bit rates from 8 to 512 bits/s (for the *Pioneer* Project). Another produces two separate simultaneous telemetry streams: an engineering stream at 8½ or 33½ bits/s, and a science stream at 66½ or 270 bits/s (for the *Mariner* Mars 1969 Project).

Either cards or live or recorded spacecraft data are utilized as the inputs, and the data may be modified for data "cleanup" or fault simulation from the console.

More realistic simulation data are produced by another ASI 6050 computer program. This program consists of mathematical models of the various spacecraft subsystems and is responsive to commands, faults, and the normal time progression of the spacecraft model. Output in the form of high-speed data or teletype is contained in two separate engineering and science telemetry data streams.

**c. System checkout support data.** Additional ASI 6050 computer programs are used as data sources for checkout of other DSN elements, such as IBM 7044 mission-independent and mission-dependent computer programs, IBM 7094 computer programs, and telemetry and command processor programs.

## II. Mission Support

### A. Introduction

The DSN, as part of the Tracking and Data System (TDS) for a flight project, is normally assigned to support the space-flight phase of each mission. Thus far, responsibility for providing TDS support from liftoff until the end of the mission has been assigned to the JPL Office of Tracking and Data Acquisition. A TDS Manager, appointed by the Office of Tracking and Data Acquisition for each flight project, works with the JPL technical staff at the AFETR to coordinate the support of the AFETR, MSFN, and NASCOM with certain elements of the DSN needed for the near-earth-phase support. A DSN Manager and DSN Project Engineer, together with appropriate personnel from the DSIF, GCF, and SFOF, form a design team for the planning and operational phases of flight support. A typical functional organization chart for operations was shown in SPS 37-50, Vol. II, Fig. 1, p. 16.

Mission operations design is accomplished in a closely coordinated effort by the Mission Operations System (MOS) and TDS Managers. Mission operations, an activity distinct from the management element MOS, includes: (1) a data system, (2) a software system, and (3) an operations system.

The data system includes all earth-based equipment provided by all systems of the flight project for the receipt, handling, transmission, processing, and display of spacecraft data and related data during mission operations. Except for relatively small amounts of mission-dependent equipment supplied by the flight project, all equipment is provided and operated by the DSN. In the near-earth phase, facilities of the AFETR and the MSFN are included. The DSN also operates and maintains the mission-dependent equipment.

The software system includes all computer programs and associated documentation. The mission-independent software is provided as part of the DSN support. The mission-dependent software developed by the flight project is operated and maintained for the project by the DSN.

The operations system includes the personnel, plans, and procedures provided by both the MOS and TDS which are required for execution of the mission operations. The mission operations design organization is supported by the DSN in the manner shown in Fig. 2, p. 17, in SPS 37-50, Vol. II. The DSN Project Engineer heads a design team composed of project engineers from various elements of the DSIF, GCF, and SFOF. This team is

primarily concerned with the data system defined above. The designs of the other systems are the responsibilities of the software system design team and the mission operations design team. The DSN supports these activities through its representative, the DSN Project Engineer.

The mission operations design process which the DSN supports was shown in Fig. 3, p. 18, in SPS 37-50, Vol. II. From the Project Development Plan and the Mission Plan and Requirements are derived the guidelines for operational planning and the project requirements for TDS support. The mission operations design team formulates system-level functional requirements for the data, software, and operations systems. From these requirements, as well as from the TDS support requirements, the DSN design team formulates the DSN configuration to be used in support of the project. It also supports, through the DSN Project Engineer, the activities of the software and mission operations design teams in designing the software and operations systems. The interface definitions are accomplished by working groups from these design teams.

The TDS support required by the project is formulated in the Support Instrumentation Requirements Document (SIRD) and the Project Requirements Document (PRD). The PRD states project requirements for support by the U.S. Department of Defense through the AFETR. The NASA Support Plan (NSP) responds to the SIRD in describing the DSN, NASCOM, and MSFN support.

## B. Mariner Mars 1971 Missions, D. J. Mudgway

The *Mariner* Mars 1971 TDS support has been planned on the basis of a baseline mission design study and is con-

sistent with the long-term development plans for the DSN Mark III data system. A DSN capabilities planning team has been established to consider matters related to the SIRD and the NSP. After these documents have been prepared, a DSN interface design team will continue support through the implementation, testing, and mission operations phases.

Various possible telemetry and command modes are being evaluated in terms of the DSN resources required to support them. These modes, given in Table 1, led to the estimate of DSN capability given below:

The DSIF can provide support through the Mars DSS (210-ft-antenna); the Echo, Woomera, and Cebreros DSSs (85-ft antennas); the launch-support compatibility test station at Cape Kennedy; and the development-support compatibility test area at JPL.

Support by the GCF will be provided using four 100-word/min teletype (as backup to the high-speed data lines), two 2400-bit/s high-speed data lines (four-channel multiplex), one voice circuit, and one 96-kHz channel (Goldstone DSCC only).

In the SFOF, the space science analysis and command and the spacecraft performance analysis and command assigned areas will be for the exclusive use of *Mariner* Mars 1971 mission control personnel. The flight path analysis and command area will be shared with other projects as required. The IBM 7044-shared disc-IBM 7094 processor will be used with backup support provided. An IBM 7040-IBM 7094 direct couple will be used for the double-precision orbit determination program.

Table 1. *Mariner* Mars 1971 telemetry and command modes under study

Subcarrier	Type of link	85-ft-antenna DSSs		210-ft-antenna DSS	
		Option 1	Option 2 <sup>a</sup>	Option 1	Option 2
Engineering telemetry	PCM/uncoded				
Number of subcarriers		2	2	2	2
Bit rate, bits/s		8-32	8-32	8-32	8-32
Command	PCM/uncoded				
Number of subcarriers		1	1	2	2
Bit rate, bits/s		1	1	1	1
Science telemetry	PCM/uncoded				
Number of subcarriers		2	—	2	—
Bit rate, bits/s		32-2000	—	32-2000	—
Video	PCM/block coded				
Number of subcarriers		—	2	—	2
Bit rate, bits/s		—	2000	—	16,000

<sup>a</sup>Capability to be negotiated.

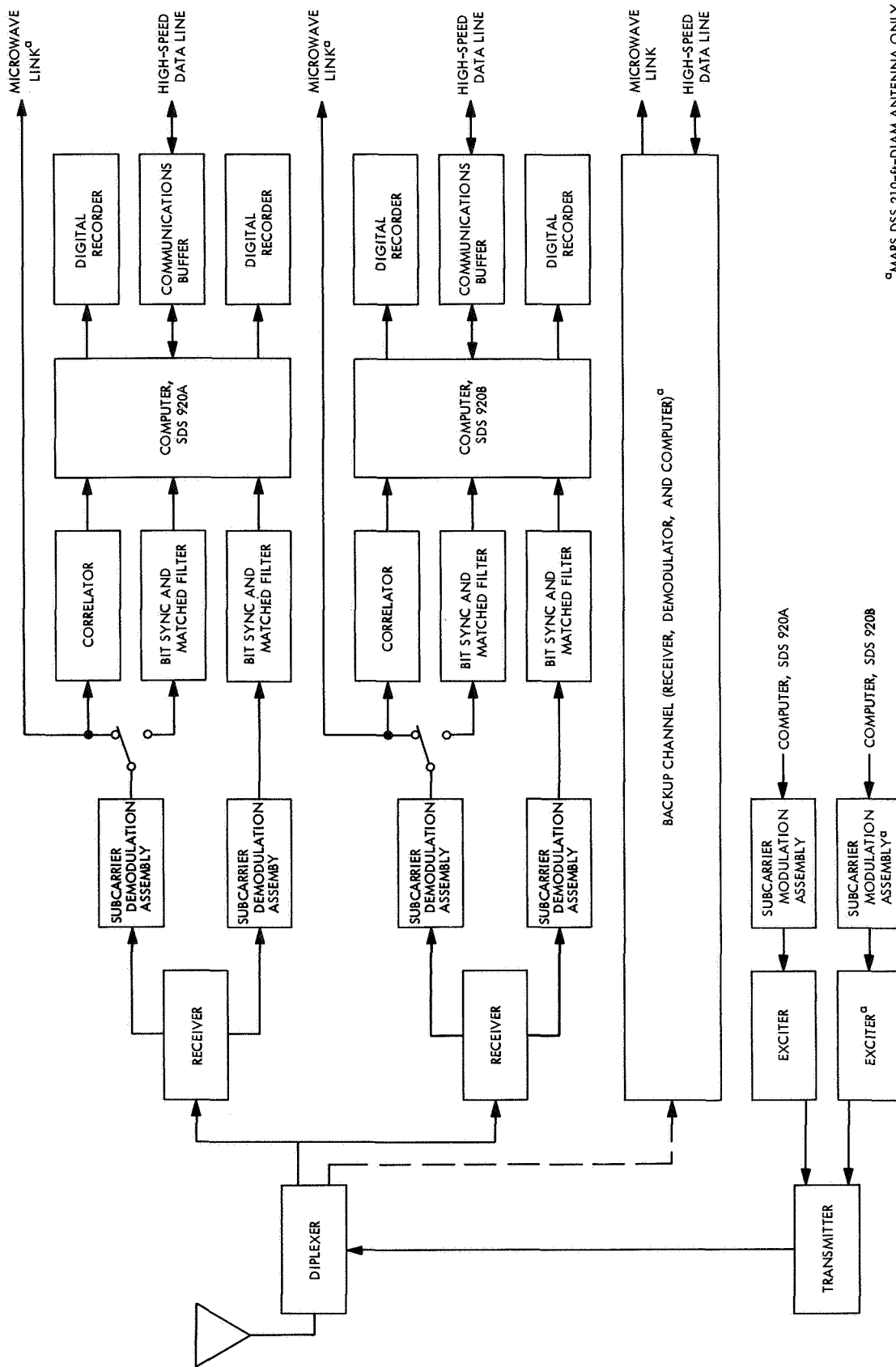


Fig. 1. DSS telemetry and command configuration for two simultaneous Mariner Mars 1971 spacecraft channels

The required DSS configuration for the above capability is shown in Fig. 1. It should be noted that this configuration implies a spacecraft variable-bit-rate capability on the video channel to allow for the difference in telecommunications performance between the 210-ft antenna and the 85-ft antennas.

The capability of the DSN to support certain critical portions of the missions is subject to some constraints. Particular attention is being paid to the role of the single 210-ft antenna (at Mars DSS) during the critical video sequences.

New interfaces between the TDS and the flight project have been defined for the *Mariner* Mars 1971 Project to minimize mission-dependent elements in various DSN systems and to more clearly identify the remaining interfaces. These interfaces are given in Table 2.

**Table 2. *Mariner* Mars 1971 Project and TDS interfaces**

DSN system functions	Responsibility <sup>a</sup>
<b>Telemetry system (real-time)</b>	
Subcarrier demodulation	T
Detection (bit synchronization and monitoring)	T
Decommulation/formatting at DSS	T
Decommulation/alarm/display at SFOF	P, T
Master-data-record production	T
Video reconstruction/display for mission operations	P, T
Special-purpose telemetry software (SFOF)	P
<b>Tracking system</b>	
Data editing (preliminary and final)	T
Orbit determination for DSS acquisition	P, T
Orbit position determination for mission operations	P
Postflight orbit data analysis and master data record	P
Guidance maneuvers and command	P
<b>Command system</b>	
Subcarrier modulation	T
Waveform generation and verification at DSS	T
SFOF/DSS command operations	T
Master-data-record production	T
Command decision/initiation at SFOF	P
<b>Simulation system</b>	
General-purpose simulation data conversion center and DSS equipment	T
General-purpose simulation data conversion center software	T
Special-purpose equipment and software	P
Command/guidance maneuvers	P
Command/responsive telemetry	P
<sup>a</sup> P: Office of Space Science and Applications/Project, T: Office of Tracking and Data Acquisition/TDS.	

## C. *Mariner V* Extended Mission Operations,

D. J. Mudgway

The DSN preparation for support of *Mariner V* extended mission operations was described in SPS 37-51, Vol. II, pp. 20, 21. Reacquisition of *Mariner V* was predicted to be possible on July 22, 1968, when the spacecraft would be within range of the 210-ft antenna at the Mars DSS. At that time, the nominal signal level was expected to be -170 dBm, with a range from earth of approximately 90 million mi.

Several weeks prior to July 22, special spectral analysis techniques were used at the Venus DSS on a research-and-development basis to try to verify the existence of a spacecraft signal. No indication of a spacecraft signal appeared at the predicted frequency or signal power level. By the time the spacecraft came within the range of the 210-ft antenna, it had been decided that the scope of the search activities should be widened to include broad frequency searches, angle searches, and attempts to establish an uplink to the spacecraft. None of these activities revealed the presence of a spacecraft signal.

Since predictions showed that in early-August it would be possible to command the spacecraft, commands were sent at that time in the hope that the spacecraft could be commanded out of a possible failure mode into an operational condition. This activity also failed to show any evidence of a spacecraft signal.

Activity of this kind continued at regular intervals until late-September. At that time, it was decided to continue searching at less-frequent intervals until the end of October, at which time the spacecraft would have reached closest approach (approximately 25 million mi) and the signal level should have reached its maximum (-148 dBmW).

During the twenty-first search attempt at the Mars DSS on October 14, a weak spacecraft signal was finally detected and quickly confirmed as originating from *Mariner V*. However, the signal was very unstable in frequency and power level. The frequency generally varied about a point approximately 30 kHz above the predicted value, and the power level was about 10 dB lower than expected. The nature of the instability precluded the possibility of obtaining any telemetry data by use of the ground telemetry system.

The signal tended to show some improvement in stability through several days of observation, but it remained

approximately 10 dB below the predicted power level and approximately 30 kHz above the predicted frequency.

On October 20, two-way lock was obtained, but the down-link signal continued to exhibit the same characteristics as previously. Attempts to send commands brought no response from the spacecraft. Observation of the down-link signal at the Mars DSS confirmed that no telemetry sidebands were present.

The frequency instability and offset, and the lower-than-predicted power level, are considered as the main factors that prevented an earlier acquisition of the signal. It is planned to continue observation of the spacecraft signal at regular intervals in an effort to understand and, if possible, resolve the present anomaly. Unless the anomaly can be resolved prior to the spacecraft's closest approach in late-October, DSN support of the *Mariner V* reacquisition activity will be terminated.

### III. Advanced Engineering: Tracking and Navigational Accuracy Analysis

#### A. Introduction, T. W. Hamilton and D. W. Trask

The DSN Inherent Accuracy Project was formally established by the DSN Executive Committee in July 1965. The objectives of the project are:

- (1) Determination (and verification) of the inherent accuracy of the DSN as a radio navigation instrument for lunar and planetary missions.
- (2) Formulation of designs and plans for refining this accuracy to its practical limits.

Achievement of these goals is the joint responsibility of the Telecommunications and Systems Divisions of JPL. To this end, regular monthly meetings are held to coordinate and initiate relevant activities. The project leader and his assistant (from the Systems and Telecommunications Divisions, respectively) report to the DSN Executive Committee, and are authorized to task project members to (1) conduct analyses of proposed experiments, (2) prepare reports on current work, and (3) write descriptions of proposed experiments. The project is further authorized to deal directly with those flight projects using the DSN regarding data-gathering procedures that bear on inherent accuracy.

The various data types and tracking modes provided by the DSIF in support of lunar and planetary missions are discussed in SPS 37-39, Vol. III, pp. 6-8. Technical work directly related to the Inherent Accuracy Project is presented in SPS 37-38, Vol. III, and in subsequent *Deep Space Network* SPS volumes, and is continued in the following sections of this volume.

Previously, it was shown that *Lunar Orbiter* residuals after an orbit program fit, using single orbits of data over a triaxial or point mass moon, accurately represent the high-frequency gravitational perturbations introduced by anomalies in the lunar potential field. *Section B* extends this work to present an improved map of the Mare Imbrium region to allow a more detailed analysis of this large mascon.

In *Section C*, analysis on the continuous estimation of the state of a distant spacecraft is extended to the effect of multiple tracking stations; previous work analyzed the dependency of the estimation accuracies on the number of completed passes of the earth-probe geometry. The present article analyzes the accuracy obtainable from two tracking stations at various longitude separations and with various switching strategies. Although two-way doppler

tracking can be obtained from only one station at a time, these switching strategies are compared against a hypothetical situation where both stations can obtain tracking during the overlap of the view periods. It is found that the switching logic which most closely matches this hypothetical case is the one which maximizes the amount of tracking data obtained at low-elevation angles.

A dynamic programming approach to optimal stochastic orbit transfer, such as may be essential while tracking pictures of a planet surface from an orbiter, is presented in *Section D*. It is assumed that the performance index can be represented by a quadratic function. However, because of the highly nonlinear nature of the orbital transition matrix, the quadratic approximation does not hold over a wide region and a technique must be designed to detect several local minima on the contour map of the performance index. This index puts a premium on angular pointing errors but is insensitive to fuel expended subject to an upper bound. The resultant optimal two-maneuver strategy is shown to be superior to the classical Hohmann transfer (minimum energy) case.

In *Section E*, preliminary results are presented from the computer program LEAP which implements the algorithm for the numerical integration of orbital satellite "lifetime" trajectories in multirevolution steps. Although sketchy and inconclusive, the results indicate that the algorithm provides an accurate integration of many-orbit trajectories and that the program will be a powerful tool for long-range predictions of an orbital satellite's position.

## **B. High-Resolution Gravimetric Map of the Mare Imbrium Region, P. M. Muller and W. L. Sjogren**

### **1. Introduction**

Reference 1 and SPS 37-51, Vol. II, pp. 28-37 document the methods used to prove that the *Lunar Orbiter* residuals after an orbit program fit, using single orbits of data, represent the high-frequency gravitational perturbations introduced by anomalies in the lunar potential field. Reference 2 and SPS 37-53, Vol. II, pp. 10-16 contain a gravimetric map of the lunar earthside hemisphere derived from 74 orbits of *Lunar Orbiter V* data. This map revealed, without exception, the presence of large gravity anomalies in each circular mare (including Mare Orientale as well).

This correspondence between ringed seas and large anomalies obviously suggests a relationship between the

phenomena. It is the purpose of this article to present an improved map of the Mare Imbrium region, which should permit more detailed analysis of a large mascon.

### **2. Nature of the Data**

The same data given in Ref. 2 and SPS 37-53, Vol. II were used, namely values of spacecraft acceleration (normalized to 100 km) obtained from processing *Lunar Orbiter V* data. In the present map, these data have been smoothed by hand, and plotted to a contour increment of 10 mgal ( $0.1 \text{ mm/s}^2$ ). Figure 1 covers the area bounded between longitudes 10 and  $-40$  deg, and latitudes 10 to 60 deg.

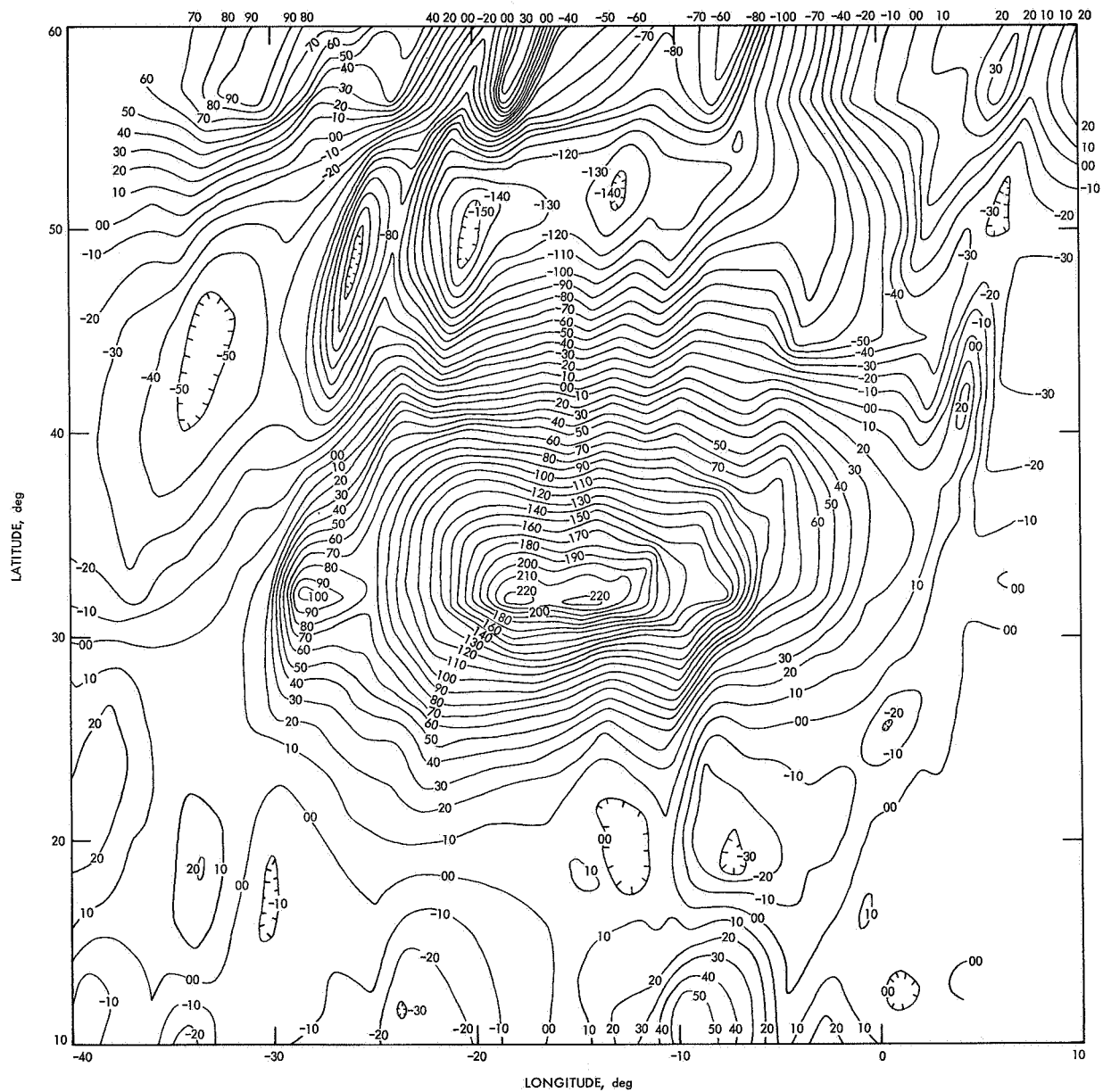
The hand smoothing involved two operations: (1) data judged inconsistent or bad was eliminated; (2) irregularities in the data stream as read in an east-west direction (perpendicular to the spacecraft trajectories) were smoothed by interpolation. These two procedures tended to eliminate deep contours caused by slight skewness in adjacent orbits.

Uncertainties in the absolute values of the gravitational anomalies still fall in the range of 20-30%. This is less precise than current knowledge of the earth's field as deduced from earth satellites. This uncertainty will remain until we are able to process more substantial quantities of data involving orbiters at varying altitudes above the surface. As Professor William Kaula (private communication) of U.C.L.A. has suggested, our estimates are likely to be low rather than high, because the least-squares fitting process will tend to reduce the residual signatures (by taking up the largest effects to some degree in the constants of integration, etc.). We therefore expect to find future improvements tending to increase slightly the largest effects, and for these reasons believe that the quoted uncertainties are realistic.

Of more interest to the selenologist, however, are questions concerning the relative variations in the gravity field. In this context, we expect that our errors will fall within approximately 3 mgal/deg on the surface. These localized errors are due primarily to the patched cubic fit to the residuals, as documented in SPS 37-53, Vol. II. Resolution of adjacent features should be possible for separations in excess of approximately 5 deg on the surface (150 km).

### **3. Observations**

We noted previously (SPS 37-53, Vol. II) that the Imbrium mascon was not circular in shape, and the elongated nature of the anomaly shows graphically in Fig. 1.



**Fig. 1. Higher resolution gravimetric map of the Mare Imbrium region**

The negative acceleration in Sinus Iridum, a unique feature on the moon, should give rise to considerable discussion as to its cause. The deeper negative area(s) north of Imbrium were originally thought to be wholly or partly due to spurious effects inherent in the least-squares fitting procedures. It is our current opinion (analysis is soon to follow) that these effects are real. Once again, interpretation of possible causes and/or significance may prove valuable. The extremely smooth profiles of Oceanus Procellarum are clearly evident on the southern border of Fig. 1. The Apennines mountain range between Mare Imbrium and Mare Serenitatis appears rather smooth with little gravity anomaly.

### References

1. Muller, P. M., and Sjogren, W. L., *Consistency of Lunar Orbiter Residuals with Trajectory and Local Gravity Effects*, Technical Report 32-1307. Jet Propulsion Laboratory, Pasadena, Calif., Sept. 1, 1968.
2. Muller, P. M., and Sjogren, W. L., "Mascons: Lunar Mass Concentrations," *Science*, Vol. 161, No. 3842, pp. 680-684, Aug. 16, 1968.

## C. Continuous Estimation of the State of a Distant Spacecraft During Successive Passes of Data: Twin Tracking Station Results, J. F. Jordan

### 1. Introduction

In SPS 37-52, Vol. II, pp. 37-44, the accuracy of the continuous minimum variance estimate of the state of a distant space probe was observed over a span of time that included several successive 12-h passes of two-way integrated range-rate data from a single tracking station, located on the earth's equator. The dependency of the estimation accuracies on the number of completed passes and the earth-probe geometry was noted, and, in particular, sensitivities of the results to the lateral velocity of the probe were observed.

In this article, the results given in SPS 37-52, Vol. II are generalized to include the behavior of the estimation accuracies when more than one tracking station are available for making observations of the probe. In particular, this presentation deals with the time history of the covariance matrix of errors in the probe states estimates, when the probe is being observed in succession by two stations located on the earth's equator, whose respective longitudes differ by an angle  $\phi$ . Sensitivities of the state uncertainties to both  $\phi$  and the station tracking switching strategy are noted.

## 2. Theoretical Development

The theory coincides with that presented in SPS 37-52, Vol. II. A space vehicle with geocentric position components  $x$ ,  $y$ , and  $z$ , and constant velocity components  $u$ ,  $v$ , and  $w$  is observed by two stations located on the earth's equator, each capable of completing 12-h passes of data.

The data type obtained by each station is counted doppler, or integrated range-rate, contaminated by stationary exponentially correlated noise. Hence, the observable  $\phi(t)$  can be expressed as

$$\phi(t) = \int_0^t \dot{\rho}(\tau) d\tau + \eta(t) \quad (1)$$

where  $\dot{\rho}$  is the range rate of change and  $\eta(t)$  is exponentially correlated noise having the following statistical properties.

$$E[\eta(t)] = 0$$

$$E[\eta(t_1)\eta(t_2)] = \sigma_\eta^2 \exp\left(-\frac{1}{\tau}|t_2 - t_1|\right) \quad (2)$$

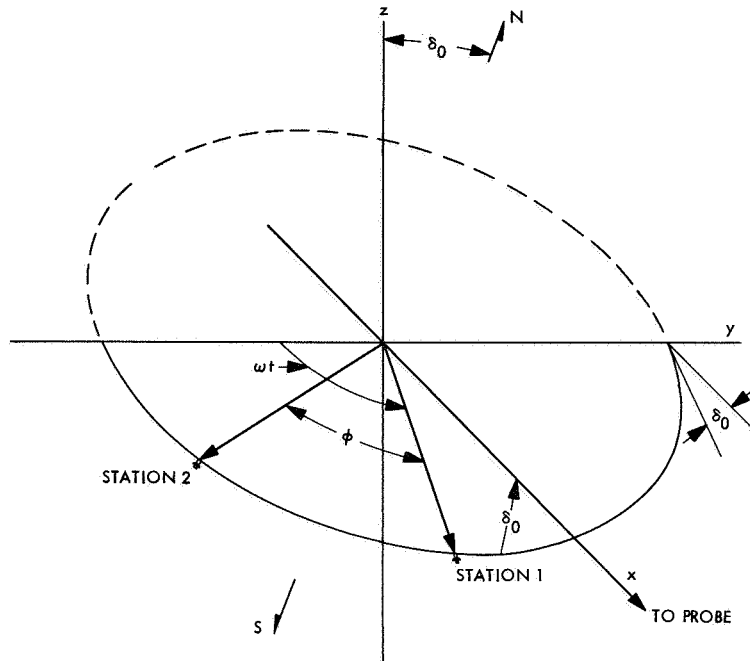
The  $(7 \times 7)$  covariance matrix of the errors in the six-dimensional state and data noise can be found from the solution of the matrix Riccati differential equation given in Eq. (13), SPS 37-52, Vol. II, pp. 37-44.

It was seen in SPS 37-52, Vol. II that the primary parameter that can be estimated from the tracking data is the probe's velocity component along the *a priori* earth-probe line  $u$ . There is also secondary estimation capability for the lateral velocities  $v$  and  $w$ , and the lateral positions  $y$  and  $z$ . The range  $x$  cannot be effectively estimated unless the lateral velocity of the probe is large.

The results presented in this article relate to a space probe at a distance of  $10^8$  km from the earth, travelling directly away from the earth. The geocentric declination of the probe is 20 deg. The solar gravitational effects on the probe are assumed negligible over the time span during which tracking occurs. The standard deviation of the data noise is 1 m and the correlation time is  $10^3$  s.

### 3. Results of Two Tracking Stations Whose Longitudes Differ by 60 deg

Consider two tracking stations located on the earth's equator whose respective longitudes differ by an angle



**Fig. 2. Geometry of probe and stations location**

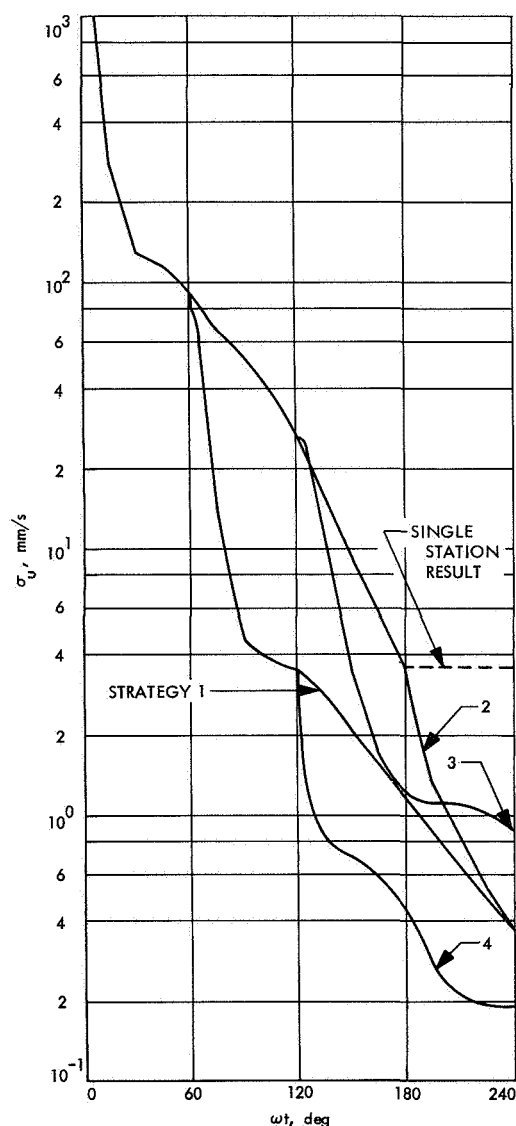
$\phi = 60$  deg. The stations are capable of successively observing the probe over a combined time span of 16 h per single pass since the earth turns through an angle of  $4\pi/3$  from the point at which the probe becomes visible to station 1 until the probe ceases being visible to station 2 (Fig. 2).

Since only one station can obtain two-way counted doppler tracking data from the space probe at any given time, consideration must be given to the length of time which is allocated to each station for tracking. In this presentation, four tracking time allocation strategies will be considered. The strategies are listed and illustrated in the following diagrams.

Figure 3 illustrates the time history of the uncertainties of the inertial range-rate estimate for the four listed station switching strategies, over a time span which includes a single combined pass of data. The accuracy of a single station pass is included (see SPS 37-52, Vol. II for a more comprehensive description of single-station results). The major conclusions which can be derived from the results shown in Fig. 3 can be summarized as follows.

Soon after a tracking switch, the uncertainty in the range-rate estimate decreases noticeably. This is due to the separation of the estimated variables. This same separation occurs at the beginning of the second pass of data in the single station (SPS 37-52, Vol. II) analysis. Note

	1. SWITCH THE TRACKING TO STATION 2 AT THE EARLIEST POSSIBLE TIME, $\omega t = \phi$
	2. SWITCH THE TRACKING TO STATION 2 AT THE LATEST POSSIBLE TIME, $\omega t = \pi - \phi$
	3. ALLOT EQUAL TIME TO EACH STATION WHILE MAXIMIZING HIGH ELEVATION TRACKING
	4. ALLOT EQUAL TIME TO EACH STATION WHILE MAXIMIZING LOW ELEVATION TRACKING



**Fig. 3. Range-rate uncertainty time history for strategies 1 to 4 ( $\phi = 60$  deg)**

that strategies 1 and 2 yield the same uncertainty at the completion of the combined pass, since the two strategies yield symmetric passes. It appears that strategy 4, which places emphasis on low-elevation tracking, is the best of the considered strategies since it produces the most favorable results over the duration of the pass, as well as at the end.

#### 4. Results of Two Tracking Stations Separated by Various Angles

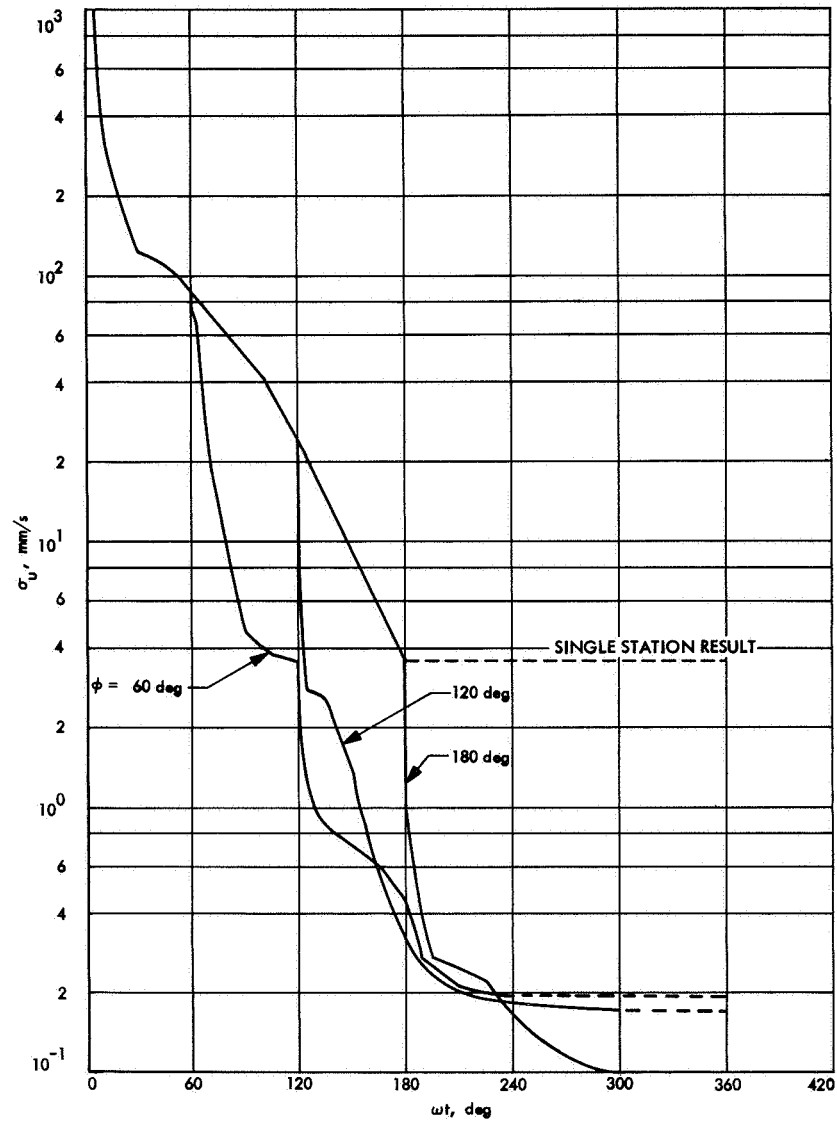
The results of *Subsection 3* indicate that the state estimate uncertainties over a single pass of data can be

markedly decreased if two stations are available for tracking. It is interesting to note how the positioning of the two stations affects the two-station accuracies. Figure 4 illustrates the time history of the inertial range-rate uncertainty over a single combined pass of data for two stations whose respective longitudes differ by the various values of  $\phi$ . Curves are shown for  $\phi = 60, 120$ , and  $180$  deg. Note that tracking switching strategy 4 is employed.

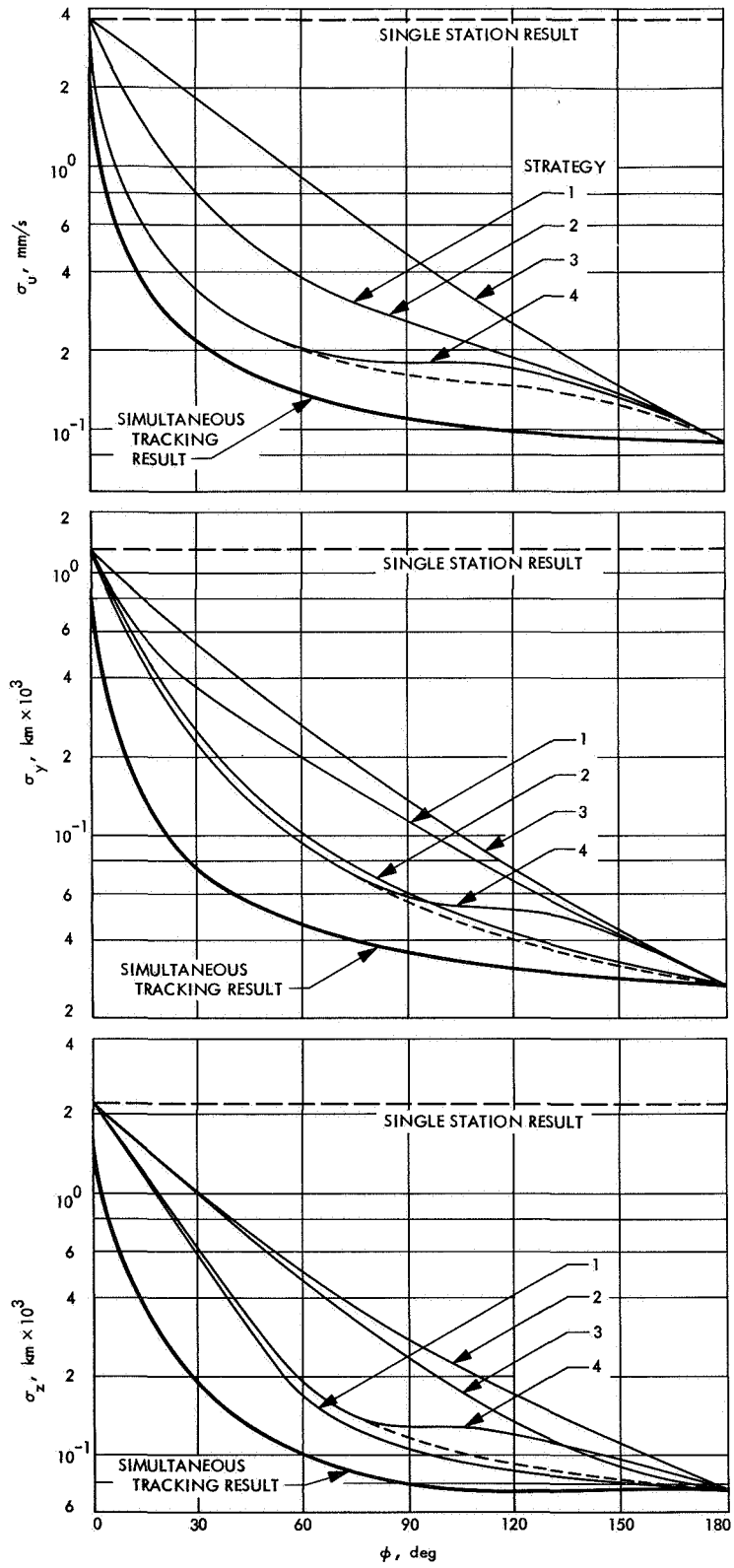
The results shown in Fig. 4 again demonstrate the rapid decrease in the state estimate uncertainties after a tracking station switch. In addition, increasing the longitude difference between the station tends to increase the effect of the tracking switching, thus the state uncertainties for a station separation of  $180$  deg are smaller than in the  $\phi = 60$  deg and  $\phi = 120$  deg configurations. Also, separating the stations increases the total tracking time in a combined single pass to such an extent that the final uncertainties in the  $\phi = 180$  deg configuration compare favorably with the single-station two-pass results (SPS 37-52, Vol. II).

To illustrate more completely the relationships between the state uncertainties, the station separation angle, and the tracking switching strategy, plots of the state uncertainties at the end of a combined pass versus  $\phi$ , for the four tracking strategies, are shown in Fig. 5. Curves are shown for the range-rate uncertainty  $\sigma_u$ , the position uncertainty in the right ascension direction  $\sigma_y$ , and the position uncertainty in the declination direction  $\sigma_z$ . In all cases, the state uncertainties are compared to the single-station one-pass results (dashed line) and the unrealistic state uncertainty obtained if both stations can simultaneously track the probe (heavy line). The curves indicate the advantage of low-elevation tracking for estimating the state variables shown. It should be noted, however, that the low-elevation tracking strategy involves three station switches in rapid succession if  $\phi$  is near  $180$  deg. In this case, the value of the low-elevation tracking is reduced somewhat due to the loss of the data noise estimate at the time of each switch. This loss has the effect of reducing the advantage of strategy 4 if  $\phi$  is near  $180$  deg. If the estimate of the data noise is assumed to be retained over the final station switch, the strategy 4 results are somewhat improved. In Fig. 5, these results are shown by a dotted line.

It appears, then, that the correlation properties of the data noise may have an effect on the choice of switching strategy; however, the choice of switching strategy, if the stations are widely separated, doesn't appear to be as critical as when the stations are closer together.



**Fig. 4. Range-rate uncertainty time history for strategy 4  
( $\phi = 60, 120, 180 \text{ deg}$ )**



**Fig. 5. Final state uncertainties vs  $\phi$  for various switching strategies**

## 5. Conclusions

Results of the study indicate that if an estimate of the state is desired within 24 h of the initiation of tracking, the utilization of two stations rather than one can improve considerably the estimate accuracies. The major factors contributing to the improvement are (1) the separation of state variables, due to data from two stations, which has stronger effect as the angular separation of the stations is increased, and (2) the increased tracking time possible with more than one station, which also increases with increasing station separation.

Four tracking station switching strategies were considered and the advantage of low-elevation tracking has been shown. The sensitivity to the tracking strategy appears to be minimal, however, if the stations are widely separated.

The results indicate that two stations placed 180 deg apart would be the most desirable configuration unless an estimate of the state is required from less than 12 h of tracking data.

## D. Dynamic Programming Approach to Optimal Stochastic Orbit-Transfer Strategy, T. Nishimura

### 1. Introduction

A general description of the single-stage and two-stage optimal stochastic transfer programs was given in SPS 37-49, Vol. II, pp. 34-43. These are the IBM 7094 computer programs which yield one or two optimal impulsive trimming maneuvers for an orbiter around a target planet subject to stochastic execution errors. The maximum fuel expenditure is limited by a prescribed amount.

The optimal corrections are derived through the following steps:

- (1) Find an optimal control  $\Delta \bar{u}_0^*$  at a fixed true anomaly  $\theta_0$  by means of Newton's method.
- (2) Find an optimal true anomaly  $\theta_0^*$  (location of maneuver point) through the two-table method—one with a rough mesh  $\Delta\theta$ , the other with a fine mesh  $\Delta\Delta\theta$ . This heuristic approach is taken in order to avoid a convergence to certain local minima with respect to  $\theta_0$  which are different from the optimal one.

The single-stage optimization program involving the optimization steps (1) and (2) is described mathematically:

$$p_1(\bar{x}_0) = \min_{\theta_0, \Delta \bar{u}_0} J_1(\bar{x}_0, \Delta \bar{u}_0, \theta_0) \quad (1)$$

where  $J_1$  is an expected value of the quadratic cost function associated with a weighting matrix  $W$ .

$$J_1(\bar{x}_0, \Delta \bar{u}_0, \theta_0) = E[(\bar{x}_1 - \bar{x}_d)^T W (\bar{x}_1 - \bar{x}_d)] \quad (2)$$

Also,  $\bar{x}_0$ ,  $\bar{x}_1$ , and  $\bar{x}_d$  are, respectively, state vectors of an initial, first (after one correction), and target orbit. For example,

$$\bar{x}_0 = \begin{bmatrix} T_0 \\ h_{p0} \\ \omega_0 \end{bmatrix} = \begin{bmatrix} \text{orbital period} \\ \text{periapsis altitude} \\ \text{periapsis argument} \end{bmatrix} \left\{ \begin{array}{l} \text{of an initial} \\ \text{orbit} \end{array} \right. \quad (3)$$

These orbital parameters are illustrated in Fig. 6.

The control  $\Delta \bar{u}$  is composed of two components:  $\Delta v$ , an increment of speed and  $\Delta \gamma$ , an increment of path angle.

$$\Delta \bar{u} = \begin{bmatrix} \Delta v \\ \Delta \gamma \end{bmatrix} \quad (4)$$

For stochastic execution errors, a scale factor error in the direction of correction and a pointing error normal to the correction vector, where both are proportional to the magnitude of correction, are taken into consideration.

When two maneuvers  $\Delta \bar{u}_0$  and  $\Delta \bar{u}_1$  are permitted, the control strategy is to minimize the expected value of weighted sum of distances between the final state  $\bar{x}_2$  and the target  $\bar{x}_d$ . In this case, when resorting to the dynamic programming approach, the cost function is first minimized with respect to  $\Delta \bar{u}_1$  and  $\theta_1$  (final stage control) by using the single-stage program described above.

$$\begin{aligned} p_2(\bar{x}_0) &= \min_{\theta_0, \Delta \bar{u}_0, \theta_1, \Delta \bar{u}_1} J_1(\bar{x}_1, \Delta \bar{u}_1, \theta_1) \\ &= \min_{\theta_0, \Delta \bar{u}_0} p_1(\bar{x}_1) \end{aligned} \quad (5)$$

The basic assumption adopted in this article is that the performance index thus minimized can be approximately represented (at least locally) in a quadratic form.

$$\begin{aligned} p_{1i}(\bar{x}_1) &\cong (\bar{x}_1 - \tilde{\bar{x}}_{1i})^T \tilde{W}_{1i} (\bar{x}_1 - \tilde{\bar{x}}_{1i}) + \beta_{1i}, \\ i &= 1, 2, \dots, m \end{aligned} \quad (6)$$

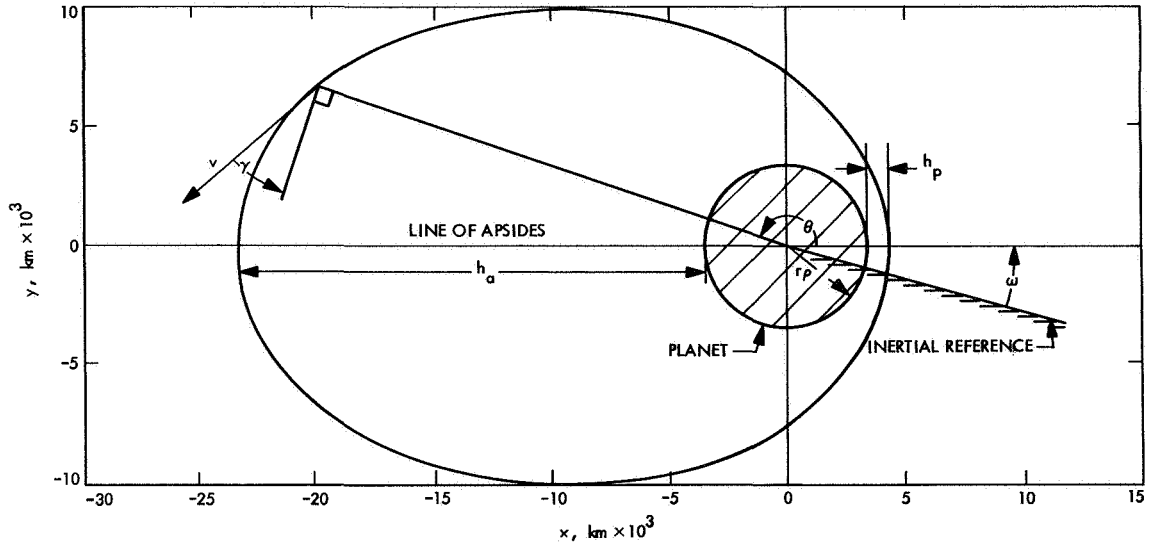


Fig. 6. Definition of orbital parameters

When Eq. (6) is substituted into Eq. (5), the entire optimization process is reduced to

$$p_2(\bar{x}_0) = \min_{\theta_0, \Delta \bar{x}_0, i} [(\bar{x}_1 - \tilde{\bar{x}}_{1i})^T \tilde{W}_{1i} (\bar{x}_1 - \tilde{\bar{x}}_{1i}) + \tilde{\beta}_{1i}] \quad (7)$$

Therefore, the third, fourth, and fifth steps of the two-stage program are as follows:

- (3) Apply the single-stage program for a sufficient number of times to find a collection of the performance index  $p_1(\bar{x}_1)$  over the  $\bar{x}_1$  parameter space and compute the new weighting matrix  $\tilde{W}_{1i}$ , target vector  $\tilde{\bar{x}}_{1i}$ , and constant term  $\tilde{\beta}_{1i}$  in Eq. (6) by means of the least-squares method.
- (4) Apply the single-stage program once more to compute the two-stage optimization strategy as described in Eq. (7).

- (5) Repeat step (4) for every  $i = 1, 2, \dots, m$  to find the overall optimal strategy.

## 2. Reachable Region

In carrying out the optimization process of Eq. (7) with respect to  $i$ , namely, with respect to every local minimum point, it is useful to predetermine the reachable region from the initial orbit  $\bar{x}_0$  by means of a single correction. The boundary surface on the  $\bar{x}_1$  parameter space of such a reachable region from the orbit  $\bar{x}_0$  can be derived from the condition of tangency between the two orbits  $\bar{x}_0$  and  $\bar{x}_1$ . This can be seen from the fact that if one of the parameters of  $\bar{x}_1$  is changed slightly from the state of tangency two orbits may get intersections, while a change in the opposite direction will make two orbits untouched to each other. The condition of tangency is described by the following equation in terms of the parameters of this article.<sup>1</sup>

$$a_1 = \frac{\{(h_{p1} + r_p)^2 + 2(a_0 - h_{p0} - r_p) \cos(\omega_1 - \omega_0) - [2a_0 - (h_{p0} + r_p)](h_{p0} + r_p)\}}{2[h_{p1} + r_p + (a_0 - h_{p0}) \cos(\omega_1 - \omega_0) - a_0]}, \quad a_1 > 0; h_{a0} > h_{p1} > 0 \quad (8)$$

where  $r_p$  is the radius of the planet,  $h_{a0}$  is the apoapsis distance of orbit  $\bar{x}_0$ , and  $a_1$  is the semimajor axis of orbit  $\bar{x}_1$ , which is related to its period  $T_1$  by

$$T_1 = 2\pi \left( \frac{a_1^3}{\mu} \right)^{1/2} \quad (9)$$

where  $\mu$  is the gravitational constant of the planet.

A small computer program for the IBM 7094 has been developed (reachable region program) which yields the cross section of the boundary surface with the  $T_1 - h_{p1}$  plane, using  $\omega_1$  as a parameter. One example is shown

<sup>1</sup>Nishimura, T., *Cotangential Orbital Transfer Strategy and Reachable Region by Single Maneuver*, July 10, 1968 (JPL internal document).

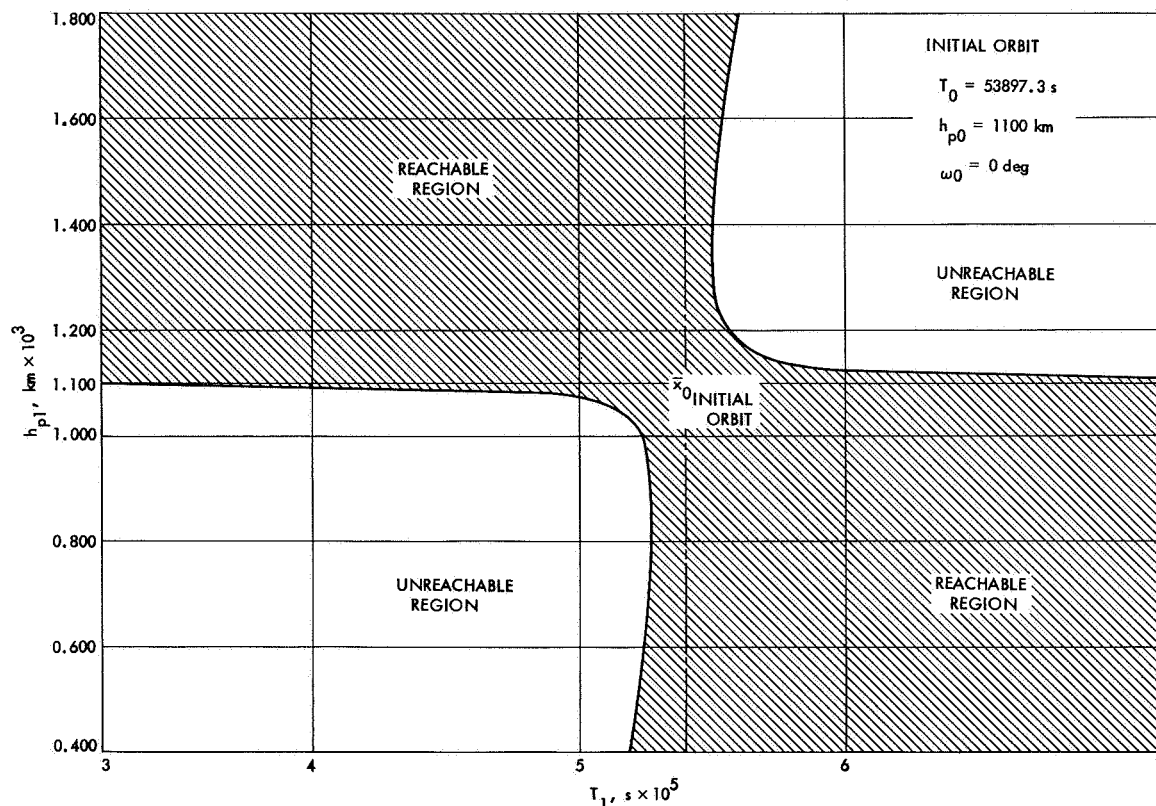


Fig. 7. Example of reachable region

in Fig. 7, in that the interior region of two curves is the reachable region from the initial orbit  $\bar{x}_0$ , which is located at the center of the figure.

This program is used to support the two-stage program in classifying the local minima of performance index of the final-stage control, depending on whether they belong to the reachable region or not. If they do not, it is useless to try to get there by single impulse. Hence, they are eliminated from consideration in finding the optimal initial control, thus making it possible to save a considerable amount of computer time as well as memory space.

### 3. Transfer Between Nonintersecting Orbits

A *Voyager*-type mission around the planet Mars was used as an example of a transfer between two nonintersecting orbits for the two-stage orbit-transfer program. The initial orbit, target orbit, and fuel data, the standard deviations of execution errors, and the weighting matrix are listed in Table 1.

The choice of the weighting matrix was made in such a way that a very heavy weight was imposed on the

Table 1. Two-stage orbit input data

Parameter	Value
<b>Initial orbit</b>	
$T_0, s$	53897.3
$h_{p0}, km$	1100
$\omega_0, deg$	0
<b>Target orbit</b>	
$T_d, s$	49551
$h_{pd}, km$	1000
$\omega_d, deg$	0
<b>Fuel</b>	
$c, m/s$	150
<b>Execution error deviation</b>	
$\sigma_s$	0.003
$\sigma_p$	0.015
<b>Weighting matrix of final stage</b>	
$W_{11}$	$10^{-3}$
$W_{22}$	$10^{-2}$
$W_{33}$	$10^2$
$W_{12}$	0
$W_{13}$	0
$W_{23}$	0

period  $T$ , while a medium weight was placed on the periaresis altitude  $h_p$ . The weight on the periaresis argument  $\omega$  was made very small. Then the deviations  $\Delta T$ ,

$\Delta h_p$ , and  $\Delta \omega$  that give a unity contribution to the performance index become, respectively,  $\Delta T = 31.6$  s,  $\Delta h_p = 10$  km, and  $\Delta \omega = 0.1$  rad = 5.7 deg.

For the sake of simplicity, the estimation error was ignored and the assigned propellant budget was chosen as  $c = 150$  m/s so that practically no constraint was imposed on the correction capability at every stage. For execution errors, a relatively large pointing error (1.5%) was used while the scale factor error was kept at 0.3%.

Figure 8 is an example of the minimized performance index  $p$  and the stochastic dispersion factor  $f$  along the orbit for the single-stage maneuver. Three local maxima and three local minima, in all six extremum points for  $p$ , are observed. This is why the heuristic search method of making two tables was employed (see *Subsection 1*): to exclude the possibility of reaching a local extremum point by searching over the entire range of  $\theta$ , instead of using a more analytical approach such as the gradient technique.

Figure 9 is one cross section of the performance index surface where  $\omega_1$  is kept at 1.3 deg. The contours indicate the corresponding performance index on the  $T_1 - h_{p1}$  plane ( $\omega_1 = 1.3$  deg). When the plane is divided by the vertical

and horizontal center lines whose intersection corresponds to the target orbit  $\bar{x}_d$ , the second quadrant becomes the region where  $T_1 < T_d$  but  $h_{p1} > h_d$ , while the fourth quadrant becomes the region where  $T_1 > T_d$  but  $h_{p1} < h_d$ . These two quadrants are essentially the areas where two orbits  $\bar{x}_1$  and  $\bar{x}_d$  have intersections (reachable). Therefore, the optimal maneuver normally takes place at one of the intersections and the direction of the correction vector is closer to the normal direction to the uncorrected velocity vector than to the tangential direction.

This drastically increases the contribution from the pointing error to the deviations, especially in period, so that large values of PI (performance index) result in these areas. On the other hand, very small values of PI are seen in the first and third quadrants where, respectively,  $T_1 > T_d$ ,  $h_{p1} > h_{pd}$  and  $T_1 < T_d$ ,  $h_{p1} < h_{pd}$ , so that two orbits have no intersections (unreachable) in most part. When the orbit  $\bar{x}_1$  lies in these regions, a correction which is almost tangential to the  $\bar{u}_1$  vector will carry the  $\bar{x}_1$  orbit close to the target  $\bar{x}_d$ , probably with a slight rotation of the line of apsides. Since the first-order contribution to the orbital period of the pointing error will be nullified by the tangential correction, the major error source will vanish under the policy of putting a heavy weight on the period, as in this example.

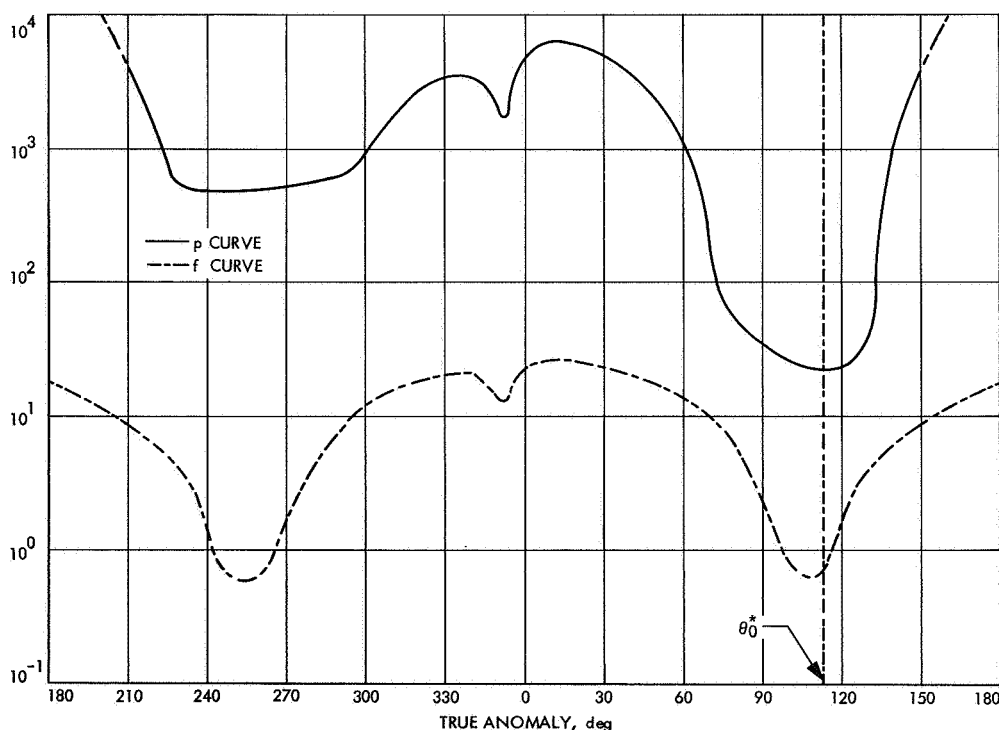
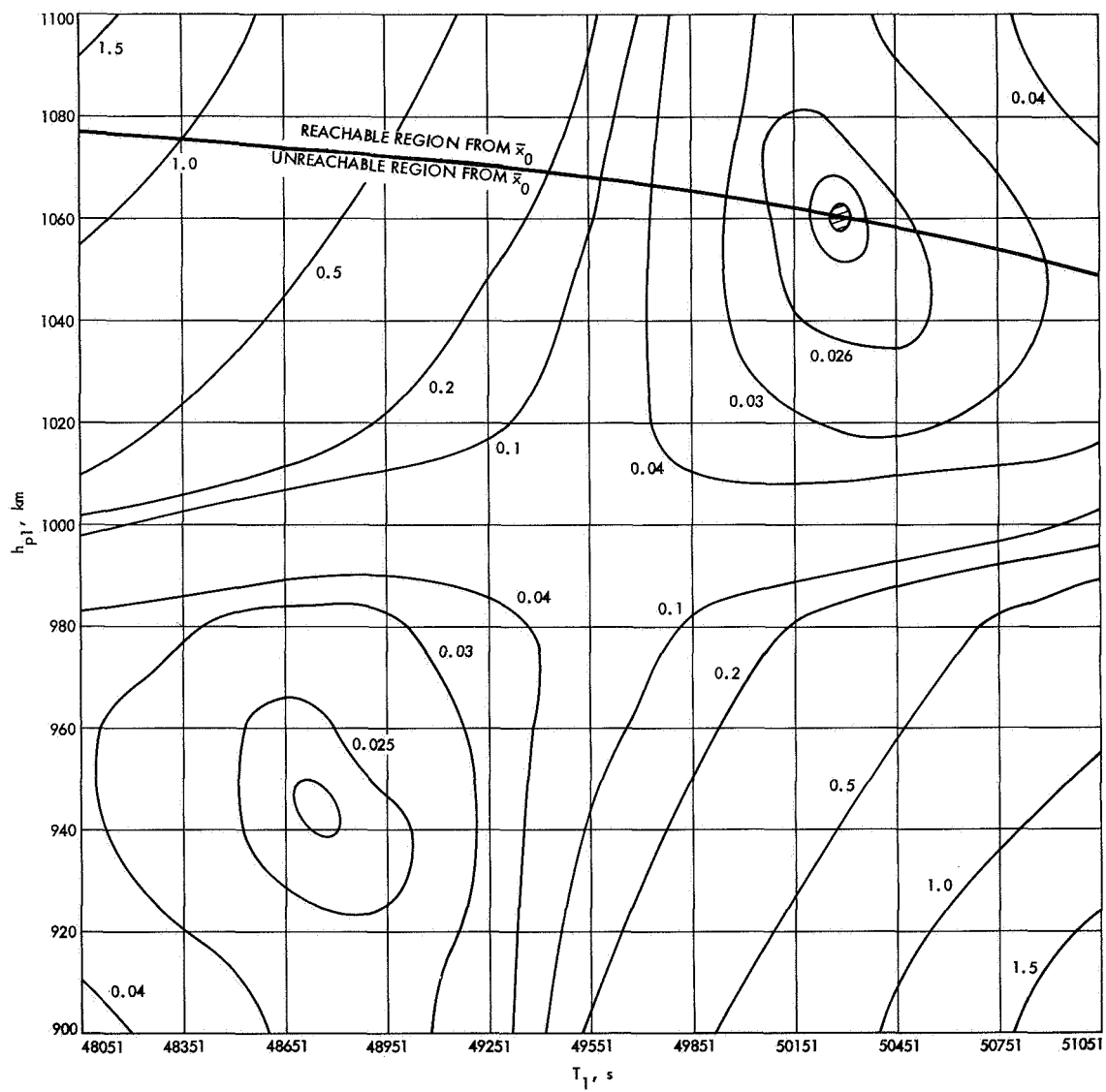


Fig. 8. Minimized performance index  $p$  and stochastic dispersion factor  $f$  ( $\omega_0 = 5$  deg)



**Fig. 9. Performance index contour map ( $\omega_1 = 1.3$  deg)**

Local minima are observed in the first quadrant as well as in the third quadrant. However, the latter was discarded from consideration because it was unreachable from the initial orbit  $\bar{x}_0$  by means of a single correction because it lay outside the boundary indicating the reachable region from  $\bar{x}_0$  (solid-line curve across the upper part of Fig. 9). Therefore, the former local minimum point was used as the intermediate target orbit  $\bar{x}_1$  and the two-stage program was applied. The results are tabulated in Tables 2 and 3, respectively, for the initial and final maneuver and are depicted in Fig. 10.

As indicated in Fig. 10, the optimal intermediate orbit  $\bar{x}_1$  is an ellipse which is almost cotangential to both  $\bar{x}_0$  and  $\bar{x}_d$  (but shallowly intersecting with them) and whose line of apsides is slightly inclined ( $\omega_1 = 1.32$  deg, while  $\omega_0 = \omega_d = 0$ ). It is interesting to compare this transfer with the Hohmann transfer from the apogee of  $\bar{x}_0$  to the perigee of  $\bar{x}_d$ . The latter is known as the transfer consuming the smallest amount of propellant ( $v_{c0} = 6.9$  m/s,  $v_{c1} = 19.5$  m/s, total = 26.4 m/s, Ref. 1). The overall PI of the former is 0.026 whereas the PI of the final maneuver at the perigee of  $\bar{x}_d$  is already 0.171. This is due to the scaling factor errors that result from the large correction at the final stage (19.5 m/s), even though the pointing

error contribution is minimized by means of the tangential maneuver (SPS 37-47, Vol. II, pp. 27-35). Since the overall PI of the latter transfer should exceed 0.171, it may be determined as inferior to the transfer of this example.

The standard deviations  $\sigma_T$ ,  $\sigma_{h_p}$ , and  $\sigma_\omega$  in Table 2 describe the 1- $\sigma$  range of uncertainty due to the initial maneuver. Also, a 3- $\sigma$  ellipsoid is depicted in Fig. 9. This is very small compared to the range where the curve fitting technique was applied to evaluate the new weighting matrix. Hence, the stochastic averaging using this  $\bar{W}$  can be justified.

#### 4. Conclusion

In this article, a dynamic programming strategy to the stochastic orbit-transfer problem has been formulated.

The optimal imbedding of the dynamic programming technique was realized through a representation of the final-stage performance index in a quadratic function. The major advantage of this assumption lies in the fact that the single-stage optimization program can be used for the initial-stage maneuver because of the quadratic form of

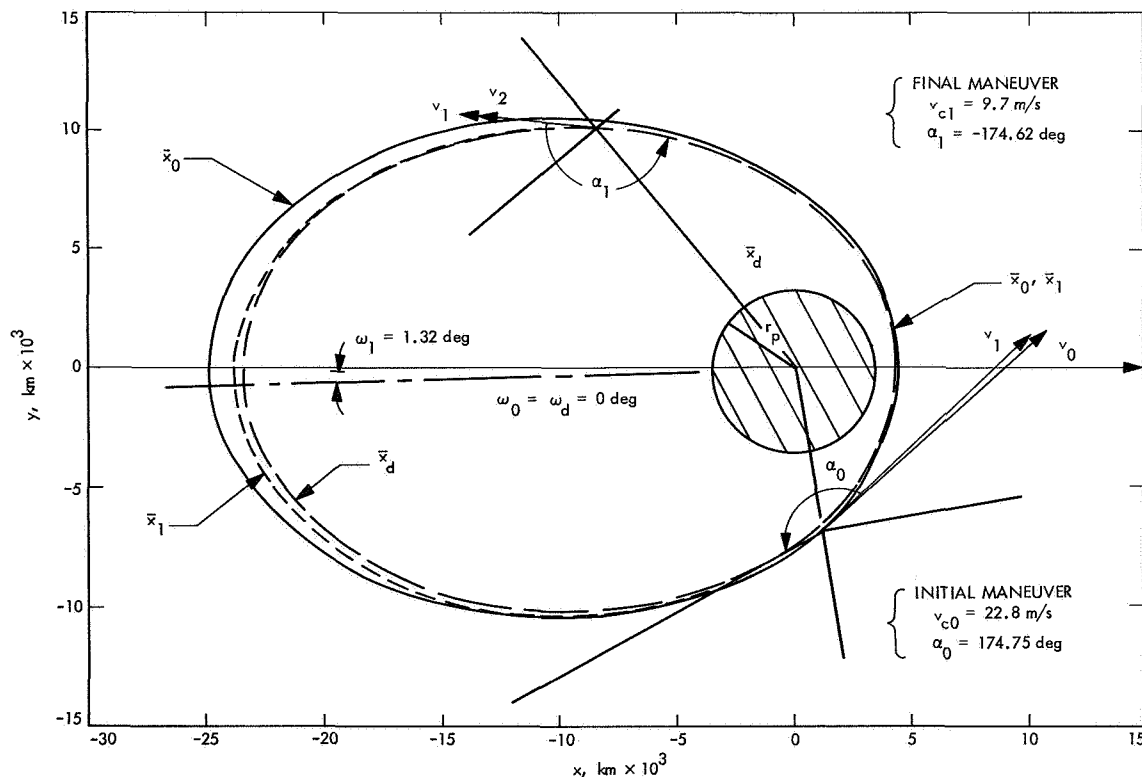


Fig. 10. Example of two-stage optimal maneuvers

**Table 2. Results of initial maneuver**

Parameter	Value	Parameter	Value
$T_0, s$	53897	$\tilde{W}_{11}$	$0.536 \times 10^{-1}$
$T_1, s$	50318	$\tilde{W}_{22}$	$0.603 \times 10^{-5}$
$\tilde{T}_{1s}, s$	50731.5	$\tilde{W}_{33}$	$0.701 \times 10^2$
$h_{p0}, km$	1100	$\tilde{W}_{12}$	$-0.275 \times 10^{-6}$
$h_{p1}, km$	1059	$\tilde{W}_{18}$	$-0.114 \times 10^{-2}$
$\tilde{h}_{p1}, km$	1059	$\tilde{W}_{23}$	$-0.700 \times 10^{-2}$
$\omega_0, deg$	0	$v_{c0}, m/s$	22.8
$\omega_1, deg$	1.32	$\alpha_0, deg$	174.8
$\tilde{\omega}_1, deg$	1.32	$\theta_0, deg$	276.0
$p_0(\bar{x}_0)$	0.026	$\theta_1, deg$	274.7
$\beta_0$	0.026	$\sigma_{T_0}, s$	12.58
$f_0$	$0.18 \times 10^{-4}$	$\sigma_{h_{p0}}, km$	0.76
		$\sigma_{\omega_0}, deg$	0.012

**Table 3. Results of final maneuver**

Parameter	Value	Parameter	Value
$T_1, s$	50318	$p_1(\bar{x}_1)$	0.026
$T_2, s$	49551	$f_1$	0.014
$T_d, s$	49551	$v_{c1}, m/s$	9.7
$h_{p1}, km$	1059	$\alpha_1, deg$	-174.6
$h_{p2}, km$	1000	$\theta_1, deg$	137.0
$h_{pd}, km$	1000	$\theta_2, deg$	137.7
$\omega_1, deg$	1.32	$\sigma_{T_0}, s$	2.5
$\omega_2, deg$	0.63	$\sigma_{h_{p0}}, km$	0.85
$\omega_d, deg$	0	$\sigma_{\omega_0}, deg$	0.004

the new cost function, which is an enormous saving of computer time as well as memory space compared to the table-formulating method.

Because of the highly nonlinear nature of the orbital transition matrix, the quadratic approximation of the performance index does not hold over a wide range of the  $\bar{x}_1$  vector space. Therefore, it is necessary to detect several local minima on the contour map of PI, then apply the minimization process of Eq. (7) locally and finally to determine the overall optimal two-stage policy.

An extensive computer program implementing the above approach has been developed for the IBM 7094. Although this computer program is quite flexible and is capable of handling various combinations of mission objectives, the experimental results are reported specifically on the maneuver achieving the desired orbital period, with high precision subject to a relatively large pointing error. This is essential to the picture-taking mission of the planet surface from the orbiter. Regions of low penalty as well as high penalty are indicated on the  $T - h_p$  plane, using  $\omega$  as a parameter. An optimal two-maneuver

strategy was compared with the classical Hohman transfer. It was shown that the Hohman transfer was decisively inferior.

## Reference

1. Lawden, D. F., "Impulsive Transfer Between Elliptical Orbits," in *Optimization Techniques*, pp. 323-351. Edited by G. Leitmann. Academic Press, New York, 1962.

## E. Some Numerical Results Using the Multirevolution Integration Program LEAP, D. Boggs and R. Leavitt

### 1. Introduction

An algorithm for the numerical integration of orbital satellite "lifetime" trajectories in multirevolution steps was recently reported (SPS 37-50, Vol. II, pp. 104-110). Later (SPS 37-52, Vol. II, pp. 44-46), the computer program LEAP (lifetime element advancing program) which implements the algorithm was described. The use of this program (IBM 7094 double-precision Fortran IV) and its outputs were briefly discussed.

In this article, some preliminary numerical results obtained from the program are summarized, and some conclusions are drawn concerning the accuracy of the algorithm. Studies comparing LEAP's computations against other integration methods have not yet been completed; thus, the results shown here may appear sketchy and inconclusive. These results nonetheless indicate that the algorithm provides an accurate integration of many-orbit trajectories, and suggest that the program will be a powerful tool for studies which require long-range predictions of an orbital satellite's position.

### 2. Review of Algorithm and Program Use

The algorithm is based on the assumption that many-orbit trajectories can be computed without actually integrating every revolution about the primary. Basically, the change in the Keplerian orbital elements during one revolution (defined as the interval between successive passages of periapsis) is determined by conventional Cowell integration of the equations of motion; this secular change then serves as the basis for a multirevolution integration step. This large integration step then advances the state elements  $m$  revolutions forward with the result that only one out of  $m$  orbits is integrated with the costly standard stepwise integrator. Thus, the computer time necessary

to calculate a long orbital trajectory is reduced to approximately  $1/m$  of that needed for conventional integration of the same trajectory.

The increments  $\Delta a$  in the orbital elements over one orbit are computed at every  $m$ th revolution by DPTRAJ, JPL's double-precision trajectory integration program.<sup>2</sup> The trajectory is advanced in  $m$ -orbit steps by an  $N$ th-order first-sum backward-difference integration (extrapolation) scheme. This integration and interpolation to intermediate orbits is performed with a set of difference equations derived in SPS 37-50, Vol. II. The multi-orbit integration can be done in any one of three modes on option: (1) predict-only (P), (2) predict-pseudo correct (P-PC), and (3) predict-correct (P-C). All of these modes are described in detail both analytically and operationally in SPS 37-50, Vol. II. The important difference in the modes is that DPTRAJ integrates one orbit per multi-revolution step in the (P) and (P-PC) modes, but must integrate twice per step in the (P-C) mode. The expense of a DPTRAJ integration (well over 90% of the total computer time required for a multirevolution step) and the relatively small gain in accuracy by the use of (P-C) over (P-PC) will normally restrict the use of the (P-C) mode to parameter optimization studies.

The time, like the orbital elements, must be computed as a function of the independent variable  $k$ , the revolution number, since the anomalistic period of the perturbed trajectory is not constant and since not every orbit is computed by DPTRAJ. As described in SPS 37-50, Vol. II, the time is computed through the intermediate variable  $\nu$ , defined as a secularly varying parameter and integrated along with the other standard Kepler elements  $a$ ,  $e$ ,  $i$ ,  $\Omega$ ,  $\omega$ . Any error incurred in the computation of time can be immediately translated into an in-track error in the calculated position of the orbiter at a periapsis. Thus, the accuracy maintained in the integration of  $\nu$  is important in determining the overall success of the multi-revolution integration algorithm.

The program user may set the parameters controlling the integration ( $m$ ,  $N$ , and integration mode) at any value over the following ranges:  $2 \leq m < \infty$ ,  $1 \leq N \leq 15$ , and mode = (P, P-PC, or P-C). There is no upper limit to the values of  $m$ , the orbit-skipping index, but the magnitude of the perturbations considered, the integration mode, and the order of integration  $N$  usually dictate a sensible

number of orbits that can be jumped. In practice,  $m$  ranges between 2 and 100 revolutions.

### 3. Comparison Studies

Preliminary accuracy studies of the algorithm consisted of comparing LEAP results (varying the parameters  $m$  and  $N$ ) with those obtained by an independent computation by DPTRAJ alone. The particular trajectory used was an earth orbiter with the following initial conditions (at a closest approach):

semimajor axis  $a = 7790.3571$  km

eccentricity  $e = 0.10145632$

inclination  $i = 44^\circ 999444$

longitude ascending node  $\Omega = -0^\circ 28331245$

argument of perifocus  $\omega = 0^\circ 30214317$

The perturbations considered were  $n$ -body effects (all solar planets plus moon), oblateness terms (zonal only) corresponding to the earth's nonspherical gravity field, and solar pressure acting on the spacecraft. The path was such that the orbiter passed in and out of the earth's shadow during every revolution. The resulting trajectory was computed by LEAP, using the parameter values  $m = 8, 16, 32$ ,  $N = 5$ , and all integration modes P, P-PC, and P-C. The fifth-order integration was found to be a good compromise; in fact, higher orders appeared to degrade the results. (Computer time costs limited further investigation into the effects of varying the integration order.) The number of revolutions integrated by LEAP varied from case to case over the range 80-1600 orbits. The comparison trajectory integrated by DPTRAJ, however, extends only to orbit number 300 after epoch. This trajectory represents a time interval of approximately 24 days. Comparison studies which have not yet been completed will involve longer trajectories.

Table 4 gives the results of the DPTRAJ computation at revolution numbers  $k = 100, 200$ , and  $300$ . In Table 5, the discrepancies, i.e., the difference between the LEAP solution and the DPTRAJ solution for the case  $m = 8$ , integration mode = (P) are summarized. The relative discrepancy is a measure of the significant digit in which the difference occurs. Tables 6 and 7 contain similar data for the same orbit-skipping case ( $m = 8$ ) as Table 5, but for different integration modes: (P-PC) and (P-C). Table 8 summarizes the results for  $m = 16$  and for both modes (P-PC) and (P-C) through orbit number 200.

<sup>2</sup>Warner, M. R., et al., *Double Precision Orbit Determination Program*, June 1967 (JPL internal document).

Completing the comparisons, Table 9 is a tabulation of the case  $m = 32$ . The integration order  $N$  is five for all cases. Zero entries in the tables represent agreement in the computations to eight significant places.

**Table 4. Results of DPTRAJ integration<sup>a</sup>**

Element	$k = 100$	$k = 200$	$k = 300$
$a$ , km	7787.5290	7781.4830	7778.6705
$e$	0.10149217	0.10114719	0.10096032
$i$ , deg	44.939943	44.878527	44.851919
$\omega$ , deg	29.250033	60.457728	89.124582
$\Omega$ , deg	332.50158	302.96847	275.67147
$t$ , s	43.219	45.876	83.622

<sup>a</sup>The values shown here for the time  $t$  are the five least significant figures in the representation of the corresponding epoch in seconds-past-1950. Computer time  $\approx 317$  min.

Table 5 reveals the accuracy of the multistep method; the "error" in the semimajor axis is only 7.4 m after 300 revolutions for the  $m = 8$ , mode = (P) case. The other Kepler elements are in similar agreement. The discrepancy in the time  $t$ , however, is somewhat significant. At orbit number 100, this difference is only 0.004 s, which corresponds to an in-track error of about 24 m (since the average orbital velocity  $\approx 6$  km/s. By orbit 300, the discrepancy in time has grown to about 1.7 s. It is not presently clear whether this "error" is a typical result of the multistep method or whether it is due to the particular perturbations that were considered. It is not even clear that the discrepancy is due to the algorithm, since a certain amount of truncation and round-off error is inherent in the DPTRAJ integration. Further investigation with different types of orbits and different integration orders

**Table 5. LEAP results:  $m = 8$ , mode = (P)<sup>a</sup>**

Element	$k = 100$		$k = 200$		$k = 300$	
	Discrepancy	Relative discrepancy	Discrepancy	Relative discrepancy	Discrepancy	Relative discrepancy
$a$ , m	-3.2	$-4 \times 10^{-7}$	7.7	$1 \times 10^{-6}$	7.4	$1 \times 10^{-6}$
$e$	$-6.2 \times 10^{-7}$	$-6 \times 10^{-6}$	$-2.1 \times 10^{-7}$	$-2 \times 10^{-6}$	$-1.8 \times 10^{-7}$	$-2 \times 10^{-6}$
$i$ , deg	$3.6 \times 10^{-5}$	$8 \times 10^{-7}$	$-15 \times 10^{-5}$	$-3 \times 10^{-6}$	$6.4 \times 10^{-5}$	$1 \times 10^{-6}$
$\omega$ , deg	$-5.8 \times 10^{-5}$	$-2 \times 10^{-6}$	$72 \times 10^{-5}$	$1 \times 10^{-5}$	$42 \times 10^{-5}$	$5 \times 10^{-6}$
$\Omega$ , deg	0	0	$7 \times 10^{-5}$	$2 \times 10^{-7}$	$12 \times 10^{-5}$	$4 \times 10^{-7}$
$t$ , s	0.004	—	1.016	—	1.748	—

<sup>a</sup>The discrepancy is in the sense LEAP-DPTRAJ. The order of integration  $N$  is 5. The difference in the semimajor axis  $a$  is given in meters. The relative discrepancy is the discrepancy divided by the magnitude of the parameter. Computer time  $\approx 78$  min.

**Table 6. LEAP results:  $m = 8$ , mode = (P-PC)**

Element	$k = 100$		$k = 200$		$k = 300$	
	Discrepancy	Relative discrepancy	Discrepancy	Relative discrepancy	Discrepancy	Relative discrepancy
$a$ , m	1.6	$2 \times 10^{-7}$	6.8	$9 \times 10^{-7}$	7.4	$1 \times 10^{-6}$
$e$	$-2.7 \times 10^{-7}$	$-3 \times 10^{-6}$	$-2.9 \times 10^{-7}$	$-3 \times 10^{-6}$	$-1.9 \times 10^{-7}$	$-2 \times 10^{-6}$
$i$ , deg	$3.4 \times 10^{-5}$	$8 \times 10^{-7}$	$-1.9 \times 10^{-5}$	$-4 \times 10^{-7}$	$3.7 \times 10^{-5}$	$8 \times 10^{-7}$
$\omega$ , deg	$8.9 \times 10^{-5}$	$3 \times 10^{-6}$	$54 \times 10^{-5}$	$9 \times 10^{-6}$	$43 \times 10^{-5}$	$5 \times 10^{-6}$
$\Omega$ , deg	0	0	$6 \times 10^{-5}$	$2 \times 10^{-7}$	$12 \times 10^{-5}$	$4 \times 10^{-7}$
$t$ , s	0.004	—	1.016	—	1.748	—

**Table 7. LEAP results:  $m = 8$ , mode = (P-C)**

Element	$k = 100$	$k = 200$	$k = 300$
$a$ , m	1.6	6.9	7.4
$e$	$-2.6 \times 10^{-7}$	$-2.8 \times 10^{-7}$	$-1.8 \times 10^{-7}$
$i$ , deg	$3.4 \times 10^{-5}$	$-1.9 \times 10^{-5}$	$3.7 \times 10^{-5}$
$\omega$ , deg	$6.4 \times 10^{-5}$	$52 \times 10^{-5}$	$39 \times 10^{-5}$
$\Omega$ , deg	0	$6 \times 10^{-5}$	$12 \times 10^{-5}$
$t$ , s	-0.007	0.671	1.592

**Table 8. LEAP results:  $m = 16$ , mode = (P-PC), (P-C)**

Element	$k = 100$		$k = 200$	
	(P-PC)	(P-C)	(P-PC)	(P-C)
$a$ , m	4.9	4.9	13.9	13.9
$e$	$-1.3 \times 10^{-7}$	$-1.3 \times 10^{-7}$	$-2.6 \times 10^{-7}$	$-2.6 \times 10^{-7}$
$i$ , deg	$3.2 \times 10^{-5}$	$3.2 \times 10^{-5}$	$-7 \times 10^{-5}$	$-7 \times 10^{-5}$
$\omega$ , deg	$28.4 \times 10^{-5}$	$28.4 \times 10^{-5}$	$117 \times 10^{-5}$	$117 \times 10^{-5}$
$\Omega$ , deg	0	0	$10 \times 10^{-5}$	$11 \times 10^{-5}$
$t$ , s	-0.102	-0.004	1.771	1.866

Table 9. LEAP results:  $m = 32$ , mode = (P-PC), (P-C)

Element	$k = 100$		$k = 200$		$k = 300$	
	(P-PC)	(P-C)	(P-PC)	(P-C)	(P-PC)	(P-C)
$a, m$	4.9	4.9	38.4	38.1	38.7	38.5
$e$	$-1.3 \times 10^{-7}$	$-1.3 \times 10^{-7}$	$-1.0 \times 10^{-7}$	$-1.2 \times 10^{-7}$	$0.3 \times 10^{-7}$	$0.1 \times 10^{-7}$
$i, \text{deg}$	$3.2 \times 10^{-5}$	$3.2 \times 10^{-5}$	$-19 \times 10^{-5}$	$-19 \times 10^{-5}$	$-26 \times 10^{-5}$	$-26 \times 10^{-5}$
$\omega, \text{deg}$	$28.4 \times 10^{-5}$	$28.3 \times 10^{-5}$	$341 \times 10^{-5}$	$322 \times 10^{-5}$	$395 \times 10^{-5}$	$357 \times 10^{-5}$
$\Omega, \text{deg}$	0	0	$-2 \times 10^{-5}$	$6 \times 10^{-5}$	$6 \times 10^{-5}$	$19 \times 10^{-5}$
$t, s$	-0.102	0.01	1.98	2.41	6.81	7.38

should reveal the nature of this time computation problem.

Tables 6 and 7 show that the use of integration modes (P-PC) and (P-C) do not significantly affect the results for the case  $m = 8$ . In particular, the slight improvement due to the full corrector (P-C) mode (which requires twice as many single-orbit integrations) makes its use here unnecessary. The time discrepancy is only insignificantly reduced by this mode. The computer time required for the  $m = 8$ , mode = (P) case is about  $\frac{1}{4}$  of that necessary for the DPTRAJ integration. For longer trajectories this factor will approach  $\frac{1}{m}$ , or, in general,  $1/m$ .

Table 8 reveals that doubling the orbit-skipping index to 16 approximately doubles the discrepancy in the semi-major axis. Again there is no significant advantage gained by the (P-C) mode over the (P-PC) mode. Table 9 indicates that increasing  $m$  to 32 caused a further error growth. The discrepancy in  $a$  is still only about 38 m at orbit 300, however. The significant increase in the time

difference probably means that a 32-orbit jump is too great for this particular case if the in-track error is required to be small.

#### 4. Conclusions

The accuracy attained by the multistep algorithm in the cases summarized here would appear to justify its use as a many-orbit integrator. For a given type of orbit, it should be possible to choose an appropriate (maximum) value for the index  $m$  such that the resulting integration error would lie within a required tolerance. In-track error bounds may prove to be the most important determinant in the selection of a value for  $m$ . Hopefully, further investigation will show that, in general, the in-track error is not as dependent on  $m$  as the cases summarized in *Subsection 3* would indicate. These results may serve as a guideline for the selection of a proper value of  $m$ , but as a rule this choice will be heavily dependent on the types of perturbations considered.

## IV. Advanced Engineering: Communications System Research

### A. Phase Jitter Measurement of Programmed Oscillators, R. F. Emerson

#### 1. Introduction

An experiment was conducted to measure the phase jitter introduced by the programmed oscillator (PO). The experimental setup is shown in Fig. 1. The measurements were taken from a variety of signal sources, but the process remained the same.

#### 2. Procedure

A signal was generated at 31.84 MHz, multiplied up to 2.388 GHz, and transmitted to an open-loop receiver the reference for which was derived from a signal source at 31.44 MHz multiplied up to 2.358 GHz. The 30-MHz IF signal was further detected to 455 kHz and was then processed by a correlator to produce a frequency spectrum of the combined signals.

Three different signal sources were used. The first was the output of the central frequency synthesizer (CFS) at 31.84 MHz. The second source was the PO located at

Venus DSS driven by the 1-MHz output of the CFS and controlled in a closed loop by an SDS 910 computer program (SPS 37-43, Vol. III, pp. 92-106). The third signal source was the PO located at Mars DSS driven by the CFS 1-MHz output through the microwave link and a "clean-up" loop and controlled in a closed loop by an SDS 920 computer program (SPS 37-39, Vol. III, pp. 71-76). The CFS was used as a reference in all cases.

The above measurement configuration included several sources of phase jitter which could not be separated from those of the POs. The transmitter, receivers, multipliers, and the free-space paths each added a component of phase jitter. This did not invalidate the measurements, because the magnitude of these components was small.

The experiment was conducted in three phases. In phase 1 each PO was compared against the output of the CFS. The Venus DSS PO was operating at 31.44 MHz and the Mars DSS PO at 31.84 MHz when the comparison was made. Figures 2a and b show the block diagrams for the measurements of parts 1 and 2 of this phase. In addition, the PO at Venus DSS was compared with the PO at Mars DSS with a constant frequency (2.388-GHz

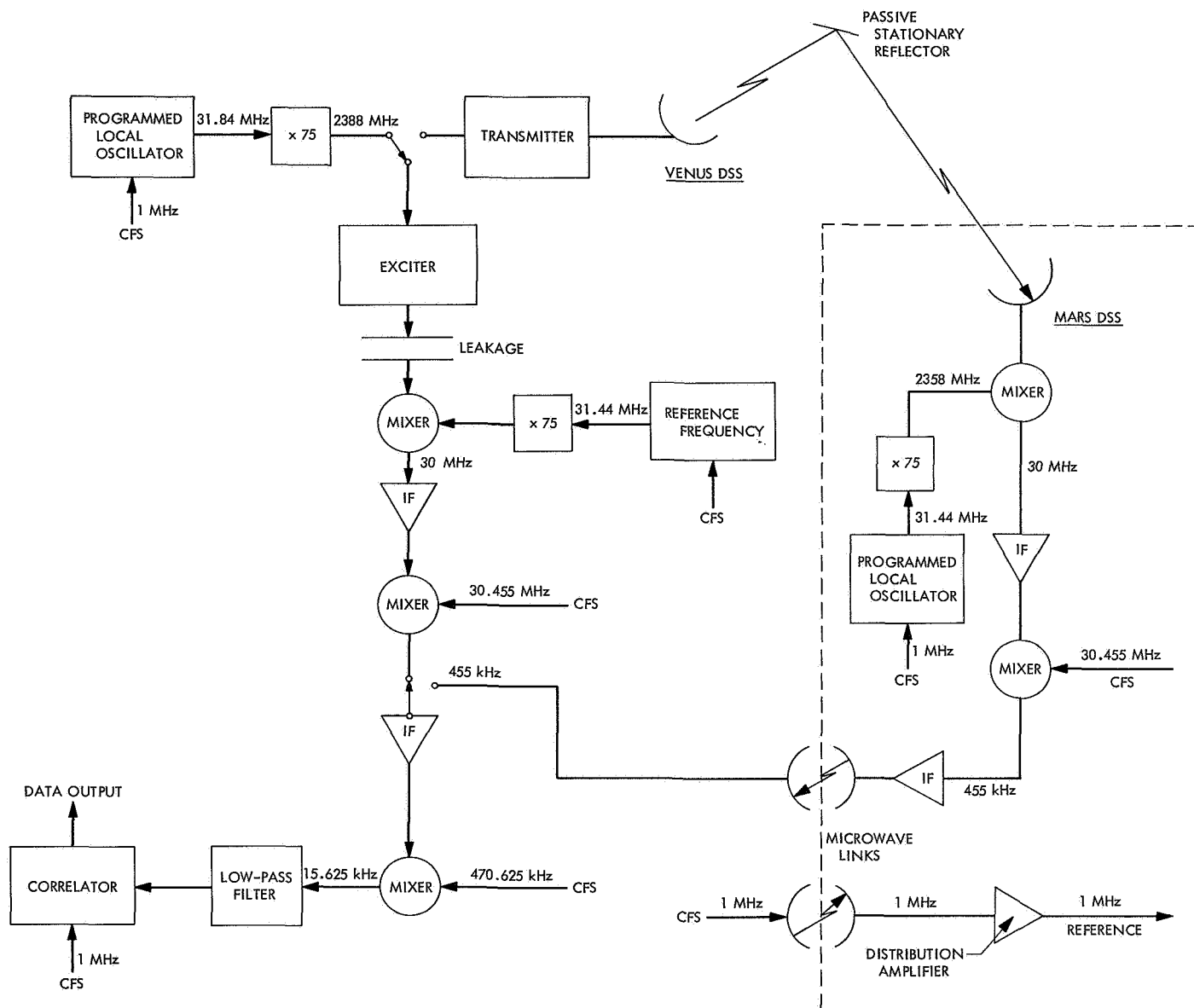


Fig. 1. Phase jitter measurement experiment configuration

transmitter frequency). Figure 2c presents the connections required for this measurement and those of phases 2 and 3. In phase 2 the two POs were compared with each other using a normal frequency ramp simulating typical doppler drive conditions. In phase 3 the two POs were compared using a frequency ramp ten times the normally expected doppler rate.

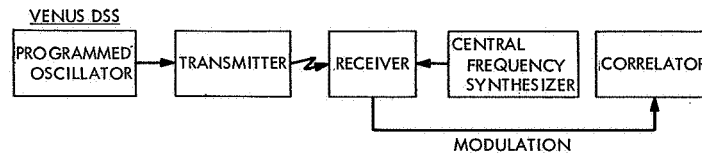
In addition to these measurements, a precalibration measurement was made of the filters used in the correlator. The best filter (i.e., maximally flat) was selected for the experiments.

### 3. Results

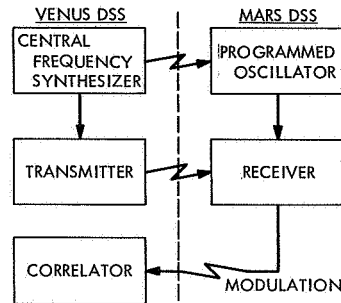
After each measurement, the results were recorded on paper tape for subsequent computer use and on an  $x-y$  plotter for visual inspection. The measurements were composed of not less than four runs, each lasting approximately 12 min. With the sampling rate set at 4.912 samples/s, approximately 16,000 samples constituted one measurement.

The results were almost identical for each phase. A typical spectrum curve is given in Fig. 3. This spectrum

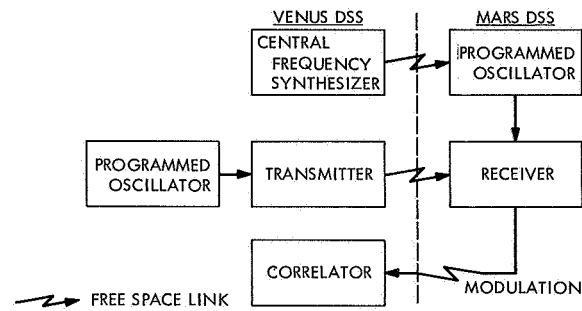
(a) PHASE 1, PART 1



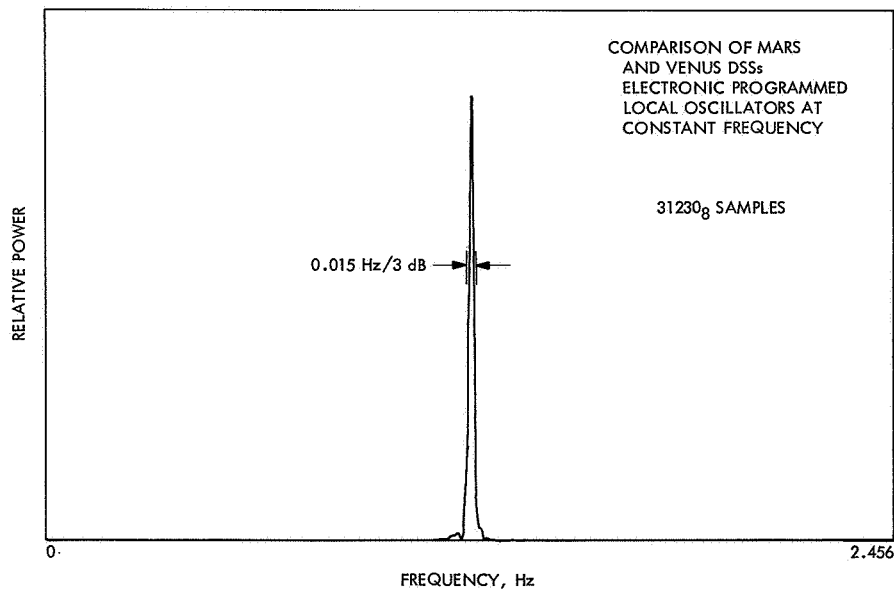
(b) PHASE 1, PART 2



(c) PHASES 2 AND 3



**Fig. 2. Measurement configurations**



**Fig. 3. Typical measured spectrum**

is that of the two POs at a constant frequency. Measured at the 3-dB point the spectral line width is less than 0.015 Hz. It should be noted that the resolution of the system (459 lags over a spectrum width of 2.456 Hz) is about 0.01 Hz.

It was possible to set only an upper bound on the phase jitter using these measurement techniques. To obtain a measurement of the lower bound of the phase jitter, it is estimated that at least 20,000 samples would have to be taken at a rate not to exceed 1 sample/10 s. Such a measurement would require about 50 h. It is not practical to make such a measurement, nor is there any present useful application.

## **B. Computer Interrupter, L. C. Constenla**

### **1. Introduction**

A free-standing unit was developed to interrupt the SDS 900 series computers at a very precise frequency rate. This allows the computer to sample an analog signal with an interrupt-rate accuracy required for high-resolution spectral analysis.

The main purpose of the computer interrupter (Figs. 4 and 5) is to provide a standard interrupt pulse for every negative-going zero-crossing of a synthesizer signal. The interrupt pulse is used in the computer to set a flip-flop as a flag that will cause a transfer of command from the main program to the interrupt routine at the proper time. This transfer of command will give priority for access to the input/output channel selected.

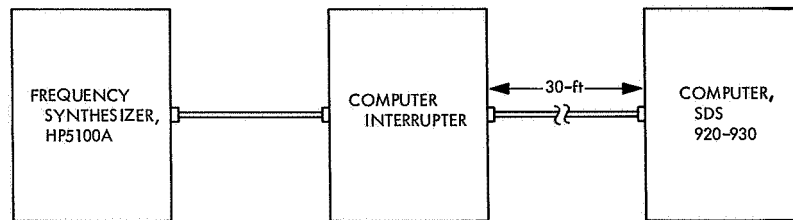
### **2. Description**

The unit is driven by a frequency synthesizer. The input signal is detected by the Schmitt trigger, and its output is differentiated and used to trigger the one-shot multivibrator. The one-shot multivibrator, in turn, is used to produce a 2.5 or 12.5  $\mu$ s pulse width. Selection of the pulse width is made manually. A 12.5- $\mu$ s pulse width is required for the SDS 920 computer and a 2.5- $\mu$ s pulse width is required for the SDS 930 computer. The interrupter is connected to the computer by a 30-ft coax cable.

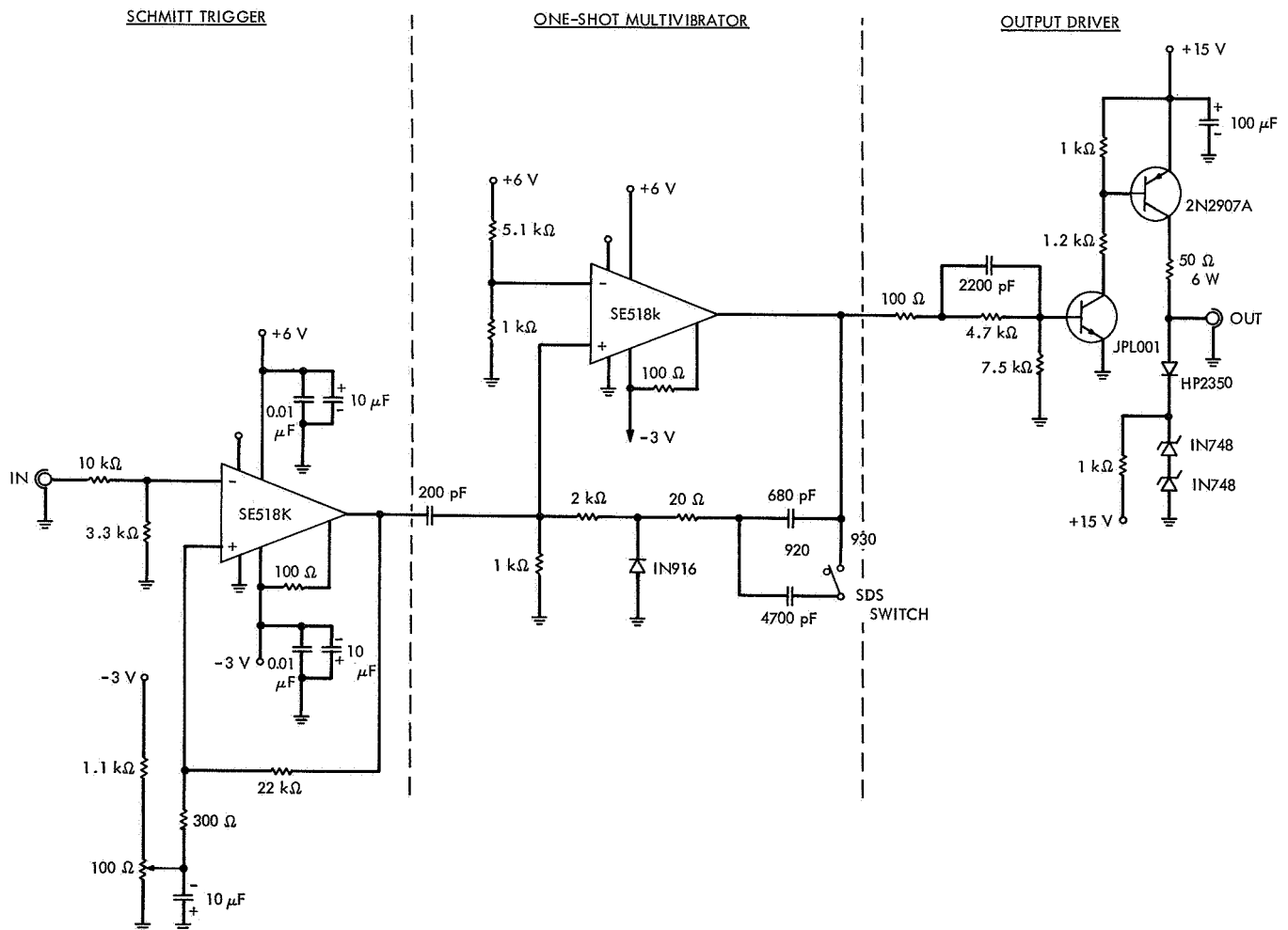
*a. Schmitt trigger.* The Schmitt trigger has 100 mV hysteresis to ensure a positive change of state when driven by a slow-varying voltage source. The input network presents a relatively high input impedance, and at the same time it offers isolation from the spurious signals reflected by the circuit.

*b. One-shot multivibrator.* The one-shot multivibrator is an improved version of one suggested in the current literature. The addition of a diode and a current-limiting resistor in the discharging path of the timing capacitor increases the duty cycle of the circuit and enables the circuit to accept the next trigger pulse much sooner. During the discharging phase, the diode is forward-biased, allowing the capacitor to discharge through the 20- $\Omega$  resistor instead of through the 3-k $\Omega$  resistance in the charging path.

*c. Driver.* The output circuit was designed to drive a 30-ft coax cable with a 50- $\Omega$  termination. The driver puts out a positive pulse with the following characteristics: amplitude 7.5 V, rise time 30 ns, repetition rate from 1 Hz to 50 kHz, and pulse width 12.5 or 2.5  $\mu$ s.



**Fig. 4. Computer interrupter block diagram**



**Fig. 5. Computer interrupter schematic**

## V. Advanced Engineering: Tracking and Data Acquisition Elements Research

### A. High-Vacuum Evaporation Techniques for Thick Metallic Film Deposition on Large Cylinders, *H. Erpenbach and C. Finnie*

#### 1. Film Deposition

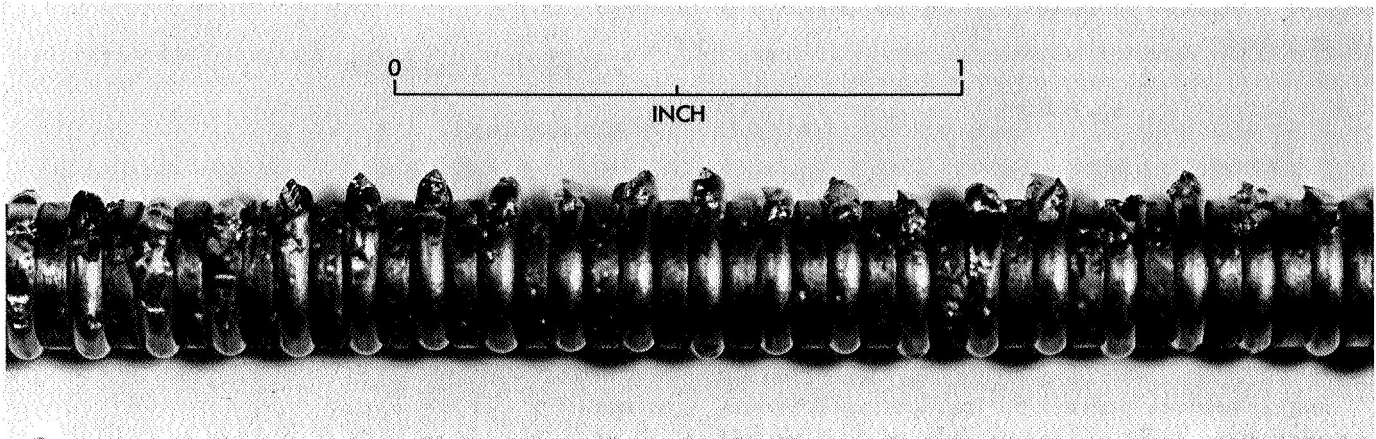
To test high-vacuum evaporation techniques for depositing thick metallic films on large cylinders, trial copper film deposits were made on the inner walls of a pyrex glass cylinder of approximately the same dimensions as the hydrogen maser cavity. The film adheres very closely to the walls and is evenly distributed. The quantity of evaporant necessary to deposit a 1-mil thickness inside the cylinder is equivalent to a rod 0.180 in. in diameter and about 12 in. in length. Since it would have been difficult to accomplish the evaporation of such an extremely large amount of material in a horizontal position using a conventional heat source, it was necessary to design a new type of electrode with a number of flat plateaus so that the evaporant would not fall off. Figure 1 shows a portion of the electrode loaded with copper wire prior to evaporation. The electrode is fabricated from a 0.25-in.-diam  $\times$  18-in.-long tantalum rod, with convolu-

tions 0.064 in. wide and 0.062 in. deep. The electrode is suspended vertically and coaxially in the cylinder.

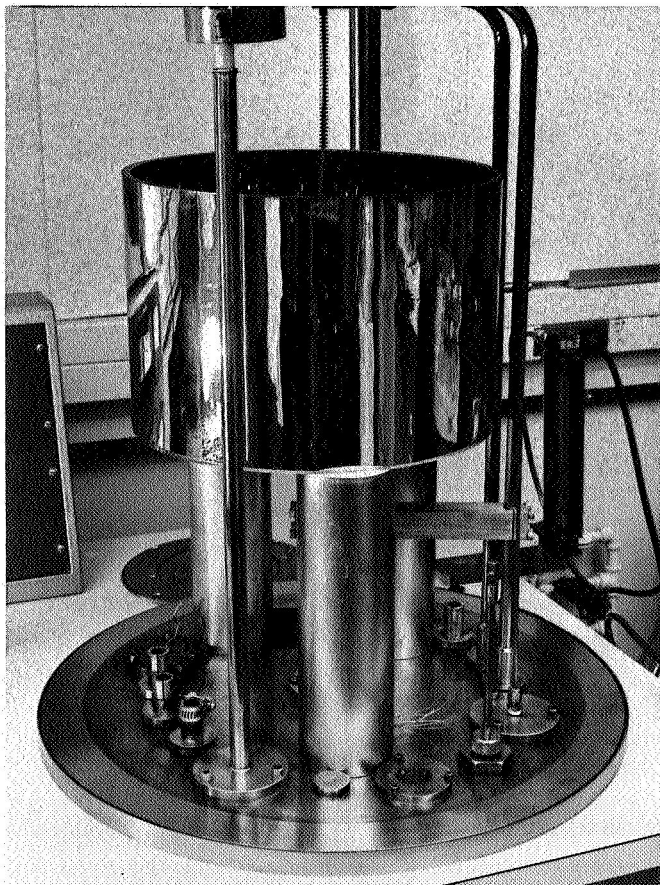
Figure 2 shows a pyrex cylinder in place after the deposition of a copper film. The actual evaporation takes about 20 min and requires about 400 A through the electrode.

#### 2. Q Measurement Techniques

The  $Q$  (energy stored/lost per cycle) of the cavities was measured using techniques that would give a good relative measurement between different materials. The hydrogen maser uses the transverse electric (TE) cylindrical cavity mode  $TE_{011}$ . This mode is degenerate with the transverse magnetic (TM) mode  $TM_{111}$  and complicates  $Q$  measurements. Under certain conditions, it is also possible to detune other adjacent modes into the desired mode by loop and tuner adjustment. For these reasons, multiple-wall cylinders were used to test the metal coatings leaving one end plate, tuner, and coupling loop undisturbed between measurements. A frequency separation between the  $TE_{011}$  mode and the  $TM_{111}$  was



**Fig. 1. Copper-wire-loaded electrode prior to evaporation**



**Fig. 2. Pyrex cylinder after copper film deposition**

obtained by using an off-axis tuning slug in the cavity. The  $Q$  measurements were made using a reflectometer with a polar display of the cavity reflection coefficient (Hewlett-Packard 8410A network analyzer). A frequency

synthesizer (HP 5100A) output of 48.7 MHz was multiplied by 30 to obtain a 1460-MHz test signal.

The reflection from a single-mode cavity at the end of a lossy cable is given by (Ref. 1)

$$\Gamma' = \frac{1 - (Y/Y_0)}{1 + (Y/Y_0)} \exp(j2\gamma l) \quad (1)$$

where

$Y$  = equivalent admittance of the cavity

$Y_0$  = characteristic admittance of the transmission line

$\gamma$  = transmission line propagation constant

$l$  = length of the line

If  $\Gamma$  undergoes the linear transformation,

$$\Gamma' = \Gamma \exp(-j2Bl) + \frac{|\Gamma_\infty| + |\Gamma_0|}{2} \quad (2)$$

where

$\Gamma_\infty$  = off-resonance reflection coefficient

$\Gamma_0$  = reflection coefficient at the cavity resonant frequency

$B$  = imaginary term of the propagation constant  $\gamma$

the amplitude of  $\Gamma'$ , near resonance, is independent of frequency for high  $Q$  circuits.

On a frequency-swept polar display, the transformation is represented by a circle centered at the origin. If the

coupling is adjusted to make  $|\Gamma_0| = 0$ , the unloaded  $Q$  is then given by

$$Q_u = 2 \frac{f_0}{B_0} \quad (3)$$

where

$f_0$  = the cavity resonance frequency

$B_0$  = the frequency shift required to shift the  $\Gamma'$  phase  $\pi$  rad on the display (resonance 3-dB points)

Using the network analyzer, the translation of the transformation given as Eq. (2) is accomplished by a shift of the oscilloscope horizontal control. The rotation is accomplished by setting the reflectometer adjustable line for a symmetrical phase versus frequency locus referenced to the horizontal oscilloscope axis.

The  $Q$  value measured is a maximum with the correctly adjusted center frequency. Adjacent mode perturbations are visible on the polar display as distortions of the resonance circle.

### 3. Copper and Aluminum Cylinder Wall Measurements

The calculations given in this subsection form the basis for anticipating the changes expected to result from the substitution of copper for aluminum as a cylinder wall coating. Because the stored energy does not depend on cavity wall conductivity, the  $Q$  ratio between the all-aluminum and partially plated copper cavity is, therefore,

$$\frac{Q_{Cu}}{Q_{Al}} = \frac{(W_{Al})_{ends} + (W_{Al})_{walls}}{(W_{Al})_{ends} + (W_{Cu})_{walls}} = \frac{1 + \frac{(W_{Al})_{walls}}{(W_{Al})_{ends}}}{1 + \frac{(W_{Cu})_{walls}}{(W_{Al})_{ends}}} \quad (4)$$

where

$(W_{Al})_{ends}$  = power loss in aluminum end plates

$(W_{Al})_{walls}$  = power loss in aluminum cylinder walls

$(W_{Cu})_{walls}$  = power loss in copper cylinder walls

The cavity power loss is given by (Ref. 2)

$$W = \frac{1}{2\sigma\delta\mu^2} \left( \oint_c dl \int_0^d dg |\bar{N} \times \bar{B}|_{sides}^2 + 2 \int_A da |\bar{N} \times \bar{B}|_{ends}^2 \right) \quad (5)$$

where

$\sigma$  = surface conductivity

$\delta$  = skin depth

The integral in Eq. (5) is the integral of the square of the tangential magnetic field over the cavity surface. Then,

$$\frac{W_{sides}}{W_{ends}} = \frac{2(\sigma\delta)_{ends} \left( \frac{K_1}{K_3} \right)^2}{(\sigma\delta)_{walls}} \quad (6)$$

where

$K_1$  = radial wave number

$K_3$  = longitudinal wave number ( $z$  direction)

The wave-number terms result from the evaluation of the integrals of Eq. (5). By inserting Eq. (6) into Eq. (4), the theoretical gain of plating the side walls of an aluminum cavity with copper is

$$\frac{Q_{Cu}}{Q_{Al}} = \frac{1 + 2.98}{1 + 2.98 \times 0.745} = 1.24$$

The theoretical  $Q$  for the  $TE_{011}$  cylindrical mode is given by (Ref. 1)

$$\frac{1}{Q} = \frac{\eta}{\pi\delta\sigma} \left\{ \frac{\lambda}{a} \left( \frac{\lambda}{\lambda_c} \right)^2 + \frac{4}{\eta} \left[ 1 - \left( \frac{\lambda}{\lambda_c} \right)^2 \right]^{3/2} \right\}$$

where

$\eta$  = reciprocal of the intrinsic impedance of the dielectric

$\lambda$  = cavity wavelengths

$\lambda_c$  = cutoff wavelength

$a$  = cavity radius

The unloaded  $Q$  evaluated for a 1420-MHz cavity is 81,800 for silver, 79,000 for copper, and 63,500 for aluminum. The theoretical improvement from an all-aluminum to an all-copper cavity should therefore be a factor of 1.241, as compared to the copper side-wall result of 1.18 where the side walls are copper and end plates are aluminum.

#### 4. Results

The following results were obtained:

Cavity type	Unloaded Q
All-aluminum cavity	38,700
Aluminum cavity with copper-plated walls	49,600
Pyrex cylinder with copper-plated walls	48,200

The measurements showed that the copper depositing technique will produce the desired Q for hydrogen maser operation (a loaded Q of approximately 30,000). The measured improvement for the copper coating (1.28) exceeds the calculated value (1.24) by less than 4%. The process has an additional advantage in that the cavity does not have to be heated to the temperatures required for a baked or silver suspension.

#### References

1. Montgomery, C. G., Dicks, R. H., and Purcell, E. M., *Principles of Microwave Circuits*. McGraw-Hill Book Company, Inc., New York, 1948.
2. Jackson, J. D., *Classical Electrodynamics*. John Wiley & Sons, Inc., New York, 1962.

### B. Broadband Microwave Waveguide Window,

C. T. Stelzried, D. L. Mullen, and J. C. Chavez

#### 1. Introduction

Waveguide windows are used in cryogenic waveguide thermal noise standards primarily to prevent atmospheric moisture from entering and contaminating the waveguide (Ref. 1). In addition, it is necessary to reduce gas convection currents that could affect the termination temperature stability. Waveguide windows constructed from bulk low-dielectric foam plastic are particularly useful because they also serve as thermal barriers. These windows are normally tuned by making their length approach a half-guide wavelength at the operating frequency. One shortcoming of this technique has been the narrow operating frequency bandwidth.

#### 2. Theory

The characteristic impedance of uniform rectangular waveguide operating in a transverse electric (TE) mode

is (Ref. 2, p. 104)

$$Z_{TE} = \frac{2b}{a} \frac{\eta}{[1 - (\lambda/\lambda_c)^2]^{1/2}} \quad (1)$$

where

$\eta$  = intrinsic impedance of the medium filling the waveguide

$a, b$  = waveguide width and height, respectively

$\lambda, \lambda_c$  = unbounded medium and waveguide cut-off wavelengths

For the TE<sub>10</sub> mode,  $\lambda_c = 2a$  so that, with unity permeability,

$$Z_{TE} = \frac{2b}{a} \frac{\eta_0}{[\epsilon_r - (\lambda_0/2a)^2]^{1/2}} \quad (2)$$

where

$\eta_0$  = intrinsic impedance of free space

$\epsilon_r$  = relative dielectric constant

$\lambda_0$  = free space wavelength

The ratio of characteristic impedances between the dielectric-filled and the unfilled (or "standard") waveguides is

$$\frac{(Z_{TE})}{(Z_{TE})_{\epsilon_r=1}} = \frac{b}{b_s} \frac{a_s}{a} \left[ \frac{1 - (\lambda_0/2a_s)^2}{\epsilon_r - (\lambda_0/2a)^2} \right]^{1/2} \quad (3)$$

where

$a_s, b_s$  = standard waveguide width and height, respectively

The filled waveguide is "matched" to the standard waveguide by setting the above equal to 1, resulting in

$$\frac{a^2 \epsilon_r - (\lambda_0/2)^2}{b^2} = \frac{a_s^2 - (\lambda_0/2)^2}{b_s^2} \quad (4)$$

Broadband matching can be achieved if  $b_s = b$  and

$$a = \frac{a_s}{\epsilon_r^{1/2}} \quad (5)$$

If  $\epsilon_r = 1 + \delta_\epsilon$  and  $a = a_s - \delta$ , where  $\delta$  can represent a shim thickness, we have

$$\delta \simeq \frac{a_s \delta_\epsilon}{2} \quad (6)$$

### 3. Experimental Measurements

Waveguide windows have been fabricated from standard 1.6-in.-long WR 90 waveguide (X-band) test sections. Shims of various thicknesses were bolted in place along the narrow wall of the waveguide to give the test piece combinations listed in Table 1. The voltage standing wave ratio (VSWR) of these pieces was evaluated over a frequency range of 8–12 GHz using a sweep generator and slotted-line technique (Ref. 3). The VSWR of the test piece in cascade with a well-matched termination is measured by recording (or photographing) and interpreting the peak-to-peak signal variation as a function of frequency due to sliding the slotted-line probe. The VSWR is given by

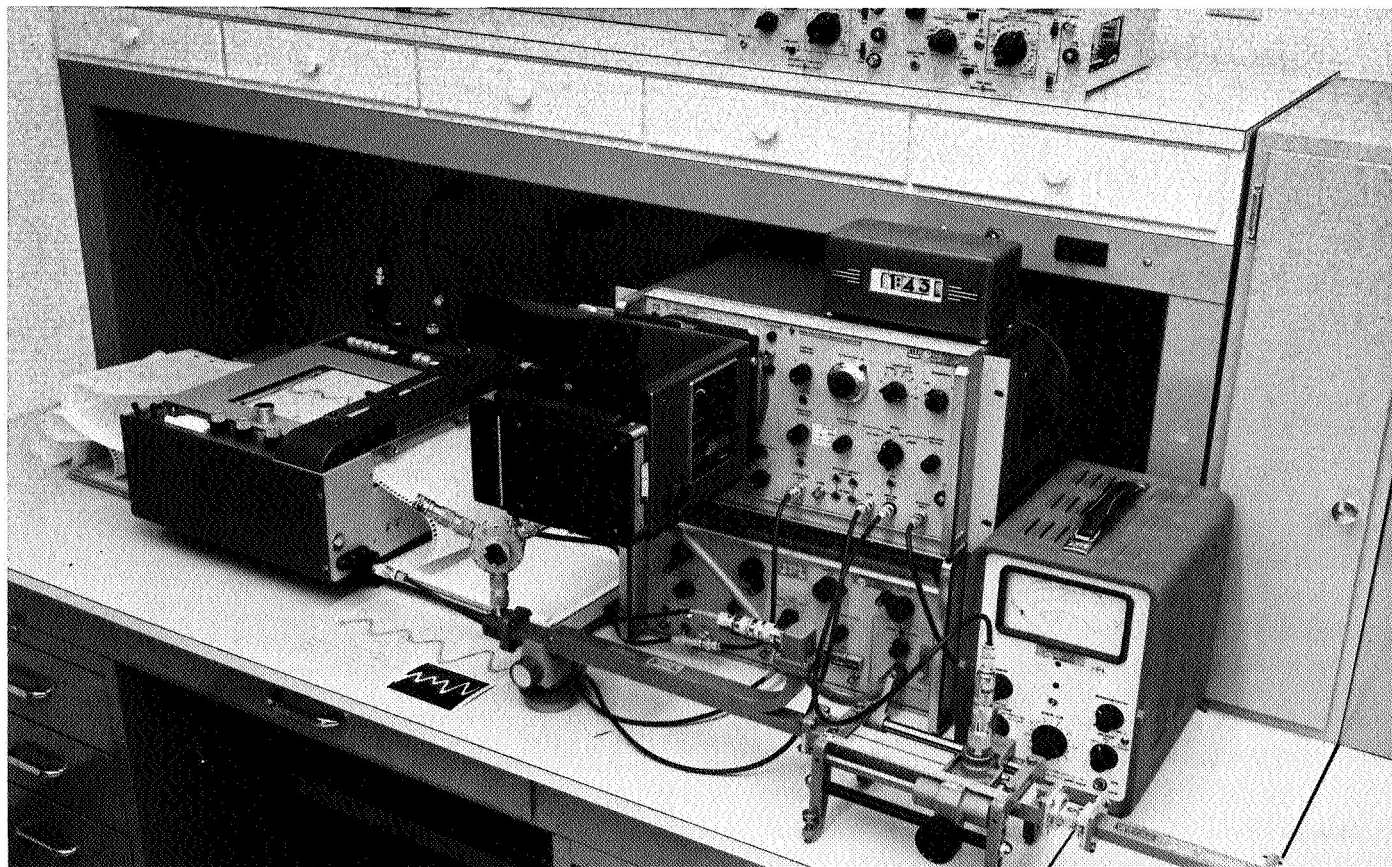
$$\log^{-1} \left( \frac{\Delta}{20} \right) = \exp \left( \frac{\Delta}{20} \ln 10 \right) \quad (7)$$

where  $\Delta$  is the peak-to-peak width in decibels.

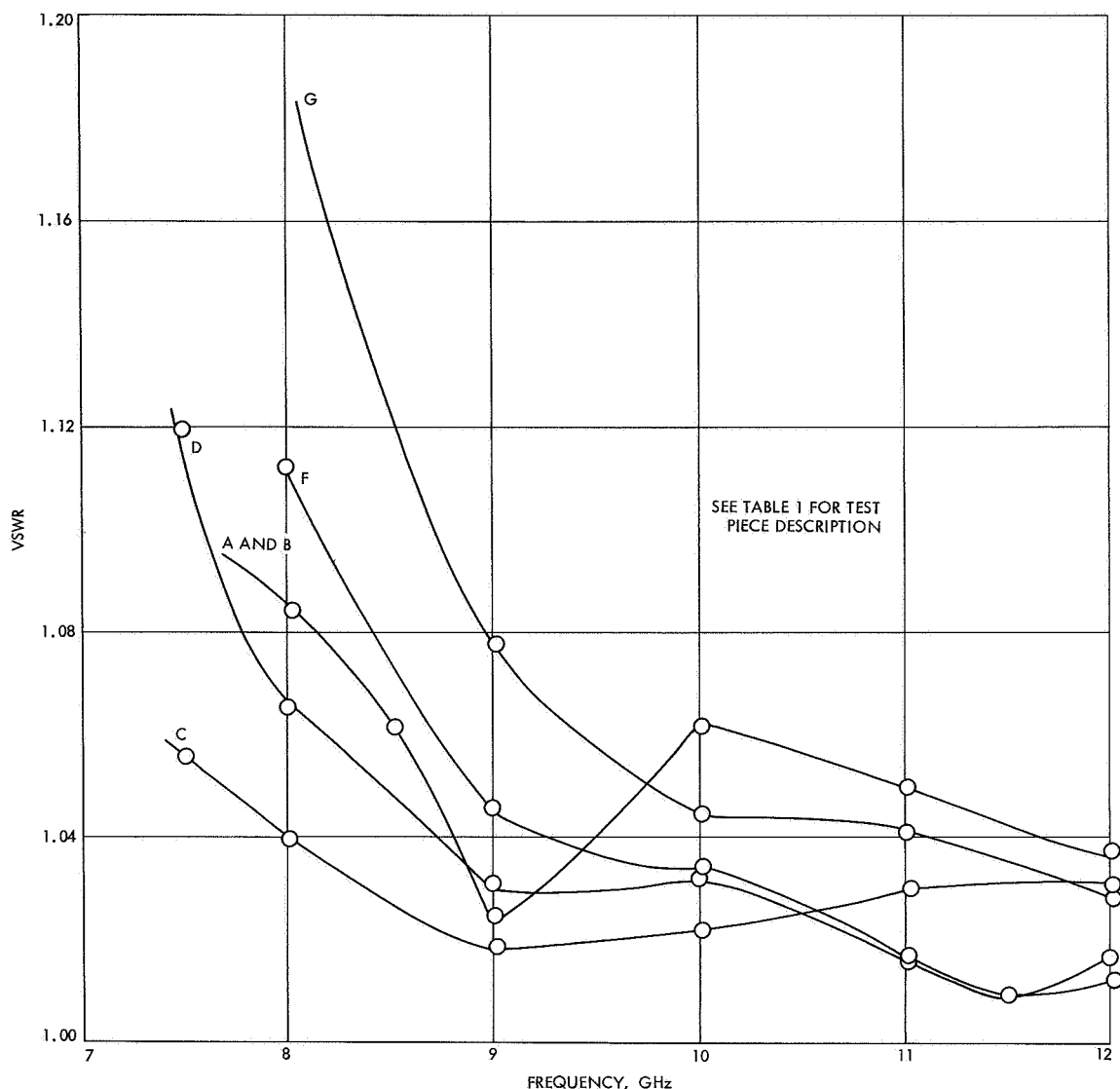
**Table 1. Description of WR 90 waveguide test sections (polystyrene-foam-filled)**

Test piece	Shim thickness, in.	Eccofoam sealing
A, B	—	No
C	0.015 (each side)	No
D	0.020 (each side)	No
F	0.025 (each side)	No
G	0.030 (each side)	No
H	0.030 (one side only)	No
J	—	Yes
E	0.032 (each side)	Yes

The broadband VSWR test installation is shown in Fig. 3. Figure 4 compares the VSWR across the frequency bandwidth for the various test pieces using polystyrene-foam-plastic filler without sealing. Test piece C, with 0.015-in. shims on each side, gives the best broadband performance. The VSWR for the test piece without shims drops to a minimum, for a narrow bandwidth, at approximately 9 GHz, at which frequency



**Fig. 3. VSWR test installation using a swept signal source and slotted line**



**Fig. 4. Broadband VSWR comparison for polystyrene-foam-filled, non-sealed test pieces**

the test section is an integral number of half-guide wavelengths. The predicted shim width from Eq. (6) with a dielectric constant of 1.04 is

$$\delta = \frac{(0.9)(0.04)}{2} = 0.018 \text{ in.} \quad (8)$$

Figure 5 compares the VSWR versus frequency performance for the polystyrene-foam-plastic-filled sections sealed with Eccofoam. These sections have a higher VSWR due to the higher dielectric constant of the Eccofoam. The measurements made using swept techniques were compared with those made using conventional

slotted-line techniques for test piece F. The VSWR values agreed to within about 0.006 across the frequency band.

#### References

1. Stelzried, C. T., "Microwave Thermal Noise Standards," *IEEE Trans. Microwave Theory Tech.*, Vol. MTT-16, No. 9, Sept. 1968.
2. Southworth, G. C., *Principles and Applications of Waveguide Transmission*, D. Van Nostrand Company, Inc., Princeton, N.J., Sept. 1961.
3. *Swept Slotted-Line System Slotted Sections*, Hewlett-Packard Technical Data for Model 817A.

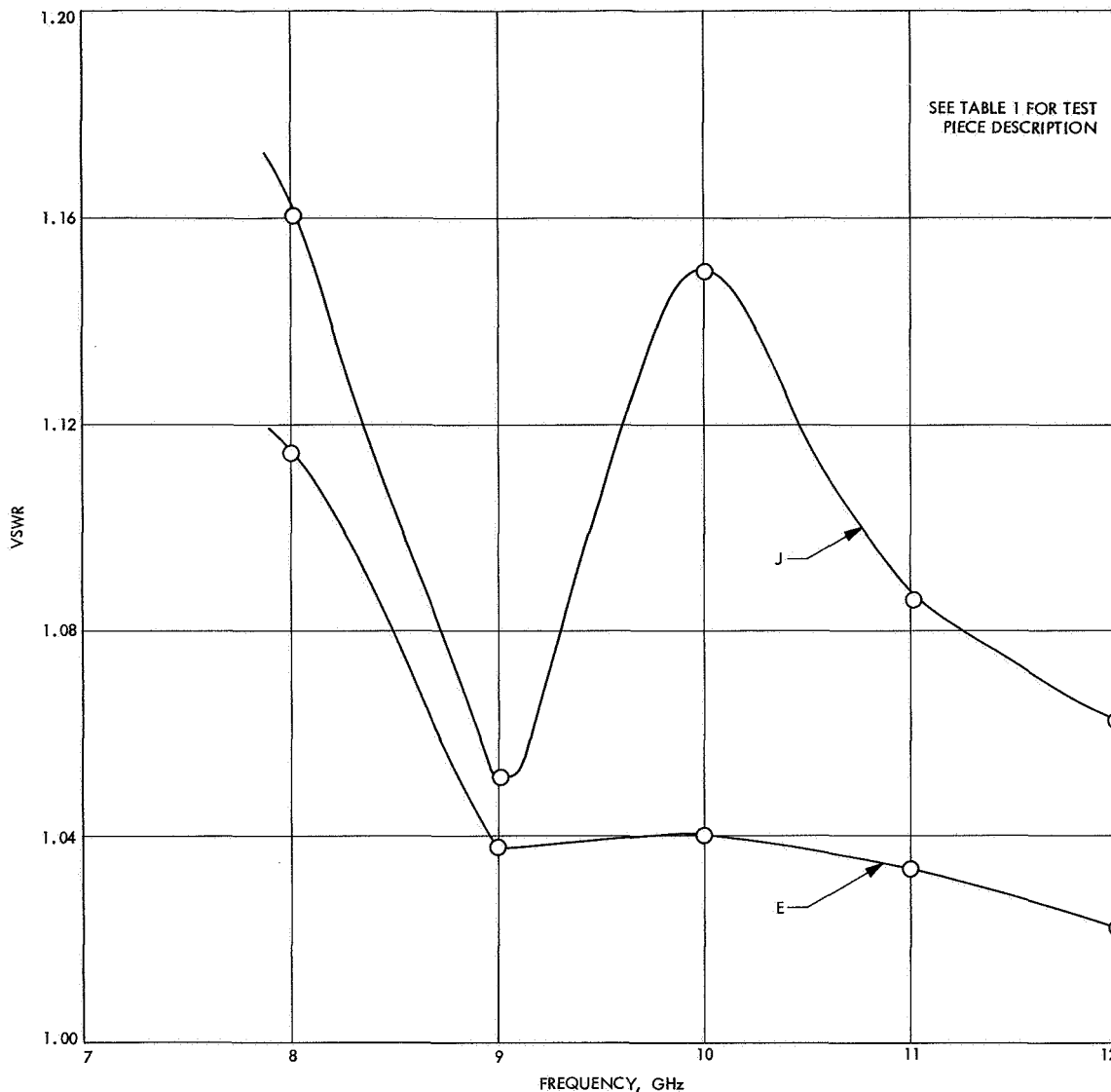


Fig. 5. Broadband VSWR comparison for polystyrene-foam-filled, Eccofoam-sealed test pieces

## C. Noise Temperatures of a Receiving System Containing Mismatched Two-Port Networks,

T. Y. Otoshi

### 1. Introduction

One of the important parameters of an interplanetary spacecraft telecommunications link is the operating noise temperature of the spacecraft. For mission performance analysis, it is sometimes desirable to know the value of this operating noise temperature at a port close to the spacecraft antenna aperture rather than at the receiver input port.

Typically, the spacecraft antenna-to-receiver input line

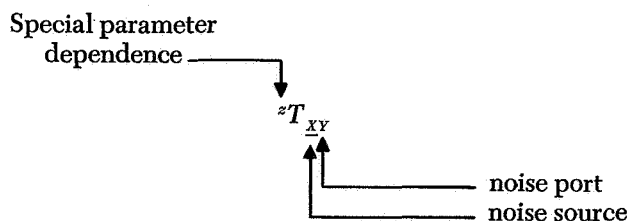
consists of coaxial components such as cables, filters, circulators, duplexers, and switches. Insertion loss and voltage standing-wave ratio measurements are often made on the individual components rather than on the overall-connected system. When the components are not matched, noise temperatures of the individual components in the connected system are not easily calculated.

This article presents some equations that can be used to analyze the noise temperatures of a spacecraft system containing mismatched components connected in cascade. The individual components are represented as two-port microwave networks that are lossy but not required to be at the same physical temperatures.

## 2. Nomenclature

The notation used in this article is the same as that used in Ref. 1. This notation is helpful in analyzing individual noise temperatures of receiving systems that consist of a large number of individual components and reference ports.

The physical temperature of a network is denoted by the symbol  $T_p$  and an additional subscript to identify the network. For example,  $T_{PS}$  is the physical temperature of network S. Available noise temperatures<sup>1</sup> are indicated by the symbol  $T$  with the subscript and superscript system shown as follows:



Internal network noise sources are identified by the first subscript letter, which will be the same as the network letter symbol. Noise source subscripts in capital letters indicate that the associated noise power flows in a direction towards the receiver output; lower case subscripts indicate that the noise power flows in a direction away from the receiver output. In the example above,  $\underline{X}$  is the noise source and indicates that the associated noise power flows towards the receiver output. The second subscript set identifies the port at which the noise temperature is defined. In the example above, Y is the port identification.

<sup>1</sup>In this article, only available noise temperatures are analyzed. If the net delivered noise temperature is required, multiply the corresponding available temperature expression by the mismatch factor  $\alpha_{i,j}$  associated with the noise port.

A double line under the noise source description subscript(s) is used to identify the following noise temperatures defined by Ref. 2: (1) the noise temperature of the input termination, (2) effective input noise temperature, and (3) operating noise temperature. These noise temperatures can be further analyzed in terms of component noise temperatures which are identified by a single line under the noise source description subscript(s).

## 3. Analysis

The equation for the noise temperature of the input termination defined at the output of several cascaded lossy (passive) two-ports may be obtained from an extension of an analysis given in Ref. 1. Figure 6 shows a receiving system that consists of noise source  $\underline{G}$ ; lossy networks A, B, and C; and the receiver connected together in cascade. The noise temperature component of the operating noise temperature at port R due to noise source  $\underline{G}$  is

$$T_{GR} = T_{GA}(\tau_{AB}\tau_{BC}\tau_{CR}) \quad (1)$$

and those from individual lossy (passive) networks are given as

$$T_{AR} = T_{AB}\tau_{BC}\tau_{CR} = [(1 - \tau_{AB})T_{PA}]\tau_{BC}\tau_{CR} \quad (2)$$

$$T_{BR} = T_{BC}\tau_{CR} = [(1 - \tau_{BC})T_{PB}]\tau_{CR} \quad (3)$$

$$T_{CR} = (1 - \tau_{CR})T_{PC} \quad (4)$$

where  $\tau_{AB}$ ,  $\tau_{BC}$ , and  $\tau_{CR}$  are the available transmission factors (available power loss or gain) of networks A, B, and C, respectively. The first and second subscripts of  $\tau$  denote the input and output ports, respectively. Table 2 is a summary of these transmission factors expressed in terms of dissipative loss factors, source voltage reflection coefficients, and network scattering parameters.

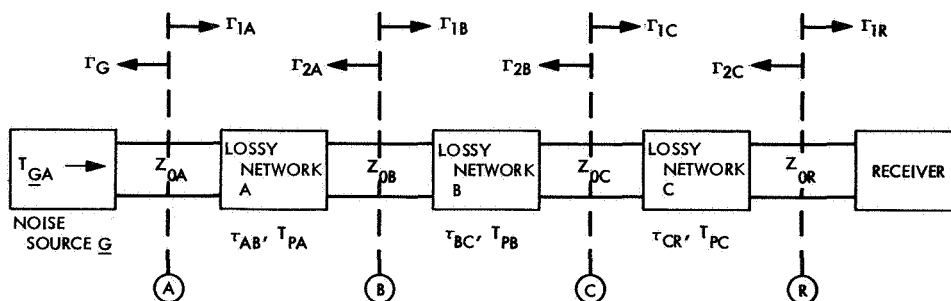


Fig. 6. Receiving system containing three cascaded lossy two-port networks between the noise source and receiver

Table 2. Exact and approximate expressions for cascaded available transmission factors

Available transmission factor	Exact expression <sup>a</sup>	Approximate expression for limits <sup>a, b</sup>
$\tau_{AB}$	$\tau_{AB} = \frac{1}{L_{AB}} \left[ \frac{(1 -  \Gamma_G ^2)(1 -  A_{11} ^2)}{ 1 - \Gamma_G A_{11} ^2 (1 -  \Gamma_{2A} ^2)} \right]$ <p>where</p> $ \Gamma_{2A}  = \left  A_{22} + \left( \frac{A_{21} A_{12}}{1 - \Gamma_G A_{11}} \right) \Gamma_G \right $	<p>For <math> \Gamma_G ,  A_{11}  \leq 0.2</math>,</p> $\tau_{AB} \approx \frac{1}{L_{AB}} \left\{ \frac{(1 -  (-1)^{i_A}   A_{11}  +  \Gamma_G ^2)}{(1 -  \Gamma_{2A} ^2)} \right\}, \quad i_A = 0 \text{ or } 1$ <p>where if <math> \Gamma_{2A} </math> was not measured, let</p> $ \Gamma_{2A}  = \left  (-1)^{i_A}  A_{22}  +  \Gamma_G  \left[ \frac{(1 -  A_{11} ^2)(1 -  A_{22} ^2)}{L_{AB} L_{BA}} \right]^{1/2} \right , \quad i_A = 0 \text{ or } 1$
$\tau_{BC}$	$\tau_{BC} = \frac{1}{L_{BC}} \left[ \frac{(1 -  \Gamma_{2A} ^2)(1 -  B_{11} ^2)}{ 1 - \Gamma_{2A} B_{11} ^2 (1 -  \Gamma_{2B} ^2)} \right]$ <p>where</p> $ \Gamma_{2B}  = \left  B_{22} + \left( \frac{B_{21} B_{12}}{1 - \Gamma_{2A} B_{11}} \right) \Gamma_{2A} \right $	<p>For <math> \Gamma_{2A} ,  B_{11}  \leq 0.2</math>,</p> $\tau_{BC} \approx \frac{1}{L_{BC}} \left\{ \frac{(1 -  (-1)^{i_B}   B_{11}  +  \Gamma_{2A} ^2)}{(1 -  \Gamma_{2B} ^2)} \right\}, \quad i_B = 0 \text{ or } 1$ <p>where if <math> \Gamma_{2B} </math> was not measured, let</p> $ \Gamma_{2B}  = \left  (-1)^{i_B}  B_{22}  +  \Gamma_{2A}  \left[ \frac{(1 -  B_{11} ^2)(1 -  B_{22} ^2)}{L_{BC} L_{CB}} \right]^{1/2} \right , \quad i_B = 0 \text{ or } 1$
$\tau_{CR}$	$\tau_{CR} = \frac{1}{L_{CR}} \left[ \frac{(1 -  \Gamma_{2B} ^2)(1 -  C_{11} ^2)}{ 1 - \Gamma_{2B} C_{11} ^2 (1 -  \Gamma_{2C} ^2)} \right]$ <p>where</p> $ \Gamma_{2C}  = \left  C_{22} + \left( \frac{C_{21} C_{12}}{1 - \Gamma_{2B} C_{11}} \right) \Gamma_{2B} \right $	<p>For <math> \Gamma_{2B} ,  C_{11}  \leq 0.2</math>,</p> $\tau_{CR} \approx \frac{1}{L_{CR}} \left\{ \frac{(1 -  (-1)^{i_C}   C_{11}  +  \Gamma_{2B} ^2)}{(1 -  \Gamma_{2C} ^2)} \right\}, \quad i_C = 0 \text{ or } 1$ <p>where if <math> \Gamma_{2C} </math> was not measured, let</p> $ \Gamma_{2C}  = \left  (-1)^{i_C}  C_{22}  +  \Gamma_{2B}  \left[ \frac{(1 -  C_{11} ^2)(1 -  C_{22} ^2)}{L_{CR} L_{RC}} \right]^{1/2} \right , \quad i_C = 0 \text{ or } 1$

Table cont'd

Table 2 (contd)

Available transmission factor	Exact expression <sup>a</sup>	Approximate expression for limits <sup>a, b</sup>
$\tau_{AC}$	$\tau_{AC} = \tau_{AB} \tau_{BC}$ $= \frac{1}{L_{AB} L_{BC}} \left[ \frac{(1 -  \Gamma_G ^2)(1 -  A_{11} ^2)(1 -  B_{11} ^2)}{ (1 - \Gamma_G A_{11})(1 - \Gamma_{2A} B_{11}) ^2 (1 -  \Gamma_{2B} ^2)} \right]$	<p>For <math> \Gamma_G ,  A_{11} ,  \Gamma_{2A} ,  \Gamma_{2B} ,  B_{11}  \leq 0.2</math>,</p> $\tau_{AC} \approx \frac{\{1 - [(-1)^{i_A}  A_{11}  +  \Gamma_G ]^2\} \{1 - [(-1)^{i_B}  B_{11}  +  \Gamma_{2A} ]^2\}}{L_{AB} L_{BC} (1 -  \Gamma_{2A} ^2)(1 -  \Gamma_{2B} ^2)},$ <p>where if <math> \Gamma_{2A} ,  \Gamma_{2B} </math> were not measured, use the expressions for <math> \Gamma_{2A} ,  \Gamma_{2B} </math> given above.</p>
$\tau_{BR}$	$\tau_{BR} = \tau_{BC} \tau_{CR}$ $= \frac{1}{L_{BC} L_{CR}} \left[ \frac{(1 -  \Gamma_{2A} ^2)(1 -  B_{11} ^2)(1 -  C_{11} ^2)}{ (1 - \Gamma_{2A} B_{11})(1 - \Gamma_{2B} C_{11}) ^2 (1 -  \Gamma_{2C} ^2)} \right]$	<p>For <math> \Gamma_{2A} ,  B_{11} ,  \Gamma_{2B} ,  C_{11}  \leq 0.2</math>,</p> $\tau_{BR} \approx \frac{\{1 - [(-1)^{i_B}  B_{11}  +  \Gamma_{2A} ]^2\} \{1 - [(-1)^{i_C}  C_{11}  +  \Gamma_{2B} ]^2\}}{L_{BC} L_{CR} (1 -  \Gamma_{2A} ^2)(1 -  \Gamma_{2C} ^2)},$ <p>where if <math> \Gamma_{2B} ,  \Gamma_{2C} </math> were not measured, use the expressions for <math> \Gamma_{2B} ,  \Gamma_{2C} </math> given above.</p>
$\tau_{AR}$	$\tau_{AR} = \tau_{AB} \tau_{BC} \tau_{CR}$ $= \frac{1}{L_{AB} L_{BC} L_{CR}} \left[ \frac{(1 -  \Gamma_G ^2)(1 -  A_{11} ^2)(1 -  B_{11} ^2)(1 -  C_{11} ^2)}{ (1 - \Gamma_G A_{11})(1 - \Gamma_{2A} B_{11})(1 - \Gamma_{2B} C_{11}) ^2 (1 -  \Gamma_{2C} ^2)} \right]$	<p>For <math> \Gamma_G ,  A_{11} ,  \Gamma_{2A} ,  B_{11} ,  \Gamma_{2B} ,  C_{11}  \leq 0.2</math>,</p> $\tau_{AR} \approx \frac{\{1 - [(-1)^{i_A}  A_{11}  +  \Gamma_G ]^2\} \{1 - [(-1)^{i_B}  B_{11}  +  \Gamma_{2A} ]^2\}}{L_{AB} L_{BC} L_{CR} (1 -  \Gamma_{2A} ^2)(1 -  \Gamma_{2B} ^2)}$ $\times \frac{\{1 - [(-1)^{i_C}  C_{11}  +  \Gamma_{2B} ]^2\}}{(1 -  \Gamma_{2C} ^2)},$ <p>where if <math> \Gamma_{2A} ,  \Gamma_{2B} ,  \Gamma_{2C} </math> were not measured, use the expressions for <math> \Gamma_{2A} ,  \Gamma_{2B} ,  \Gamma_{2C} </math> given above.</p>

<sup>a</sup>  $L_{ij}$  = dissipative loss factor ( $\cong 1$ ) of the network when the input and output ports are I and O, respectively (Ref. 1).

<sup>b</sup> Choose combinations of  $i_A, i_B, i_C$  and  $i_C$  values that result in maximum and minimum values for  $\tau$ . Use a computer program if number of cascaded networks become large.

The noise temperature of the input termination at port  $R$  may be expressed in terms of its component noise temperatures as

$$T_{\underline{GR}} = T_{\underline{GR}} + T_{\underline{AR}} + T_{\underline{BR}} + T_{\underline{OR}} \quad (5)$$

and the operating noise temperature at port  $R$  as

$$T_{\underline{TGR}} = T_{\underline{GR}} + {}^{20}T_{\underline{RR}} \quad (6)$$

where  ${}^{20}T_{\underline{RR}}$  is the effective input noise temperature of the receiver at port  $R$  when the input termination has a  $\Gamma_{20}$  reflection coefficient. If we wish to define the effective input noise temperature at port  $A$ , we may write

$$T_{\underline{AA}} = \frac{T_{\underline{AB}}}{\tau_{AB}} = \left( \frac{1}{\tau_{AB}} - 1 \right) T_{PA} \quad (7)$$

$$T_{\underline{BA}} = \frac{T_{\underline{BC}}}{\tau_{AB}\tau_{BC}} = \frac{1}{\tau_{AB}} \left[ \left( \frac{1}{\tau_{BC}} - 1 \right) T_{PB} \right] \quad (8)$$

$$T_{\underline{CA}} = \frac{T_{\underline{CR}}}{\tau_{AB}\tau_{BC}\tau_{CR}} = \frac{1}{\tau_{AB}\tau_{BC}} \left[ \left( \frac{1}{\tau_{CR}} - 1 \right) T_{PC} \right] \quad (9)$$

$$T_{\underline{RA}} = \frac{{}^{20}T_{\underline{RR}}}{\tau_{AB}\tau_{BC}\tau_{CR}} \quad (10)$$

so that the effective input noise temperature at port  $A$ , in terms of its components, may be expressed as

$${}^6T_{\underline{RA}} = T_{\underline{AA}} + T_{\underline{BA}} + T_{\underline{CA}} + T_{\underline{RA}} \quad (11)$$

Since the input termination is now defined at port  $A$ , then

$$T_{\underline{GA}} = T_{\underline{CA}} \quad (12)$$

and the operating noise temperature at port  $A$  may be expressed as

$$T_{\underline{TGA}} = T_{\underline{GA}} + {}^6T_{\underline{RA}} = \frac{T_{\underline{TGR}}}{\tau_{AB}\tau_{BC}\tau_{CR}} \quad (13)$$

Note that the expressions in Table 2 for the available transmission factors  $\tau$  require knowledge of both magnitudes and phase angles of the voltage transmission and reflection coefficients. If only magnitudes of these coefficients have been measured, then only bounds on the noise temperature values can be established. The difference between these bounds and the calculated value (when neglecting mismatches) represent uncertainties due to mismatch.

Because the possible phase angle relationships are functions of the actual network loss conditions, the limits given in Table 2 are only approximate but are believed to be accurate within 5%. Further work is being done to obtain more accurate expressions. The results will be reported in a future SPS article.

#### 4. Conclusion

This article has considered only the case of three cascaded lossy two-port networks. It is, however, a simple matter to extend the analysis to the case of  $n$ -cascaded networks. H. A. Haus and R. B. Adler (Ref. 3) have discussed the general case where the cascaded networks can be amplifiers having either positive or negative output resistances. In their treatment, a more general term "exchangeable gain" is given in place of "available gain."

#### References

1. Otoshi, T. Y., "The Effect of Mismatched Components on Microwave Noise-Temperature Calibrations," *IEEE MTT Special Issue on Noise*, Vol. 16, pp. 675-686, Sept. 1968.
2. IRE Standards on Electron Tubes: Definition of Terms, 1962 (62 IRE 7.S2) *Proc. IEEE*, p. 434, Mar. 1962.
3. Haus, H. A., and Adler, R. B., "An Extension of the Noise Figure Definition," *Proc. IRE*, Vol. 45, pp. 690-691, May 1957.

#### D. Operating Noise Temperature Calibrations of the JPL Research Cones, C. T. Stelzried

Low-noise receiving system operating noise temperature calibrations using the ambient load technique have been discussed in SPS 37-42, Vol. III, p. 25, and SPS 37-52, Vol. II, pp. 61-67. The calibrations are made by switching the maser input between the antenna and an ambient termination. The principal advantage of this technique is the long-term stability and reliability of the ambient termination. Another advantage is that it is not necessary to evaluate the waveguide losses when the system operating noise temperature is defined at the maser input. This technique depends on a previous calibration of the maser input noise temperature; however, a 10% error in this parameter results in only about a 1% error in the system temperature measurement for a typical JPL low-noise installation. Noise temperature calibrations discussed in this article were performed during the period June 12 to October 1, 1968.

The present JPL "front end" research cones using the ambient load calibration technique are designated:

- (1) S-band planetary radar (SPR) cone.

- (2) S-band multifrequency (SMF) cone.
- (3) S-band cassegrain ultra (SCU) cone.
- (4) S-band cassegrain experimental (XCE) cone.

These cones are operated on the antennas of the Venus and Mars DSSs in a cassegrain configuration.<sup>2</sup> A summary of the calibration parameters used for the operating noise temperature computer program (JPL ID 5841000, CTS20B) for these cones is presented in Table 3.

Figure 7 is a graph of the measurement results taken with the SPR cone operating on the 85-ft antenna at the Venus DSS. A tabulation of the averaged operating noise temperature calibrations for the various research cone/antenna configurations is presented in Table 4. (The case

number definitions for the various operating noise temperature calibration configurations are given in Table 5.) The indicated errors are the standard deviation of the individual measurements and of the mean. These do not include the instrumentation bias errors, e.g., those due to non-linearity, etc. The system operating noise temperature averages were computed using only data with:

- (1) Antenna at zenith.
- (2) Clear weather.
- (3) No RF spur in receiver pass band.
- (4)  $PE_{T_{op}/D}$  less than  $0.10^{\circ}\text{K}$  (from computer program CTS20B).

The maser gain is nominally optimized prior to each operating noise temperature calibration. Measurements are made approximately twice a month to check for amplifier saturation (verification of system linearity).

<sup>2</sup>Most of the calibration data presented were taken by the personnel at the DSSs indicated.

Table 3. Calibration parameter summary of JPL research cones

Cone			Date	Config-uration	Fre-quency, MHz	Noise box correction, dB		Maser tem-perature, °K	VSWR			Approximate zenith low-noise path operating noise temperature, °K	
Model	SN	Mod				C <sub>1</sub> (gain) <sup>a</sup>	C <sub>2</sub> (VSWR) <sup>a</sup>		S <sub>A</sub> <sup>b</sup>	S <sub>P</sub> <sup>b</sup>	S <sub>e</sub> <sup>b</sup>	Ground located	Antenna mounted
SPR <sup>c</sup>	01	01	7/66		2295	26.0	20.0	5.3	1.237	1.352	1.172		
					2388	26.0	20.0	5.0	1.015	1.006	1.094		
SPR	01	02	5/68		2295	26.0	20.0	5.3	1.250	1.280	1.174		
					2388	26.0	20.0	5.0	1.084	1.020	1.463	17.5	21.0
SMF	01	00			2297	26.0	20.0	7.2	1.026	1.033	1.252		
					2388	26.0	20.0	7.0	1.040 <sup>d</sup>	1.300 <sup>d</sup>	1.050 <sup>d</sup>		
SMF	01	00	9/68	0-4 (maser 1)	2295	26.0	17.0	4.5 <sup>e</sup>	1.120	1.003	1.130	19.0	
					2388	26.0	17.0	4.5 <sup>e</sup>	1.220	1.133	1.230 <sup>d</sup>		
SMF	01	01	9/68	5-9 (maser 2)	2295	36.0	20.0	5.4	1.100 <sup>d</sup>	1.300 <sup>d</sup>	1.300 <sup>d</sup>		
					2388	36.0	20.0	5.7	1.100 <sup>d</sup>	1.300 <sup>d</sup>	1.300 <sup>d</sup>		
SCU <sup>f</sup>	01	00	7/67		2295	33.0	20.0	4.1	1.013	1.005	1.222		
					2388	33.0	20.0	5.1	1.030	1.253	1.252	20.5	24.0
SCU <sup>g</sup>	01	01	3/68	0-4 (maser 1)	2295	33.0	20.0	4.1	1.044	1.001	1.266	13.5	17.0
					2388	33.0	20.0	5.1	1.147	1.263	1.249	16.5	20.0
SCU	01	01	3/68	5-9 (maser 2)	2295	26.0	20.0	5.4					27.0
					2388	26.0	20.0	5.7					
XCE <sup>h</sup>	01	00			8448	36.0	20.0	13.7	1.010	1.006	1.020	32.5	36.0

<sup>a</sup>C<sub>1</sub> = greater path loss to maser input than to maser output. C<sub>2</sub> = greater path loss to maser input than to termination or antenna evaluated.

<sup>b</sup>S<sub>A</sub>, S<sub>P</sub>, S<sub>e</sub> = VSWR, defined at maser input, of antenna (right circular-polarized), ambient termination, and maser input, respectively.

<sup>c</sup>SPS 37-40, Vol. III, p. 98.

<sup>d</sup>Fictitious data.

<sup>e</sup>Estimated data.

<sup>f</sup>SPS 37-48, Vol. II, p. 52.

<sup>g</sup>SPS 37-51, Vol. II, p. 82.

<sup>h</sup>SPS 37-43, Vol. III, p. 59.

**Table 4. Average calibration parameter summary**

Case	Reflectometer calibration, dB		Maser gain, dB	Noise temperature, °K	
	Ambient load	Antenna		Follow-up contribution	Operating
1	36.0 ± 1.3/0.11 (150)	32.6 ± 5.0/0.41 (150)	38.8 ± 0.3/0.02 (150)	0.71 ± 0.05/0.01 (101)	20.7 ± 0.50/0.05 (101)
2	—	—	39.6 ± 0.6/0.2 (15)	1.19 ± 0.16/0.05 (12)	19.8 ± 0.33/0.10 (12)
3	37.2 ± 5.0/1.0 (27)	33.4 ± 4.8/0.9 (27)	51.8 ± 2.5/0.5 (27)	0.13 ± 0.22/0.05 (18)	16.9 ± 0.82/0.19 (18)
4	—	—	48.4 ± 0.7/0.2 (9)	0.41 ± 0.23/0.10 (5)	28.2 ± 2.22/0.99 (5)
5	53.9 ± 7.0/0.2 (15)	24.0 ± 4.6/1.1 (15)	50.4 ± 0.40/01 (15)	0.04 ± 0.01/0 (7)	18.5 ± 0.27/0.10 (7)

NOTE: Numbers in parentheses indicate number of measurements performed to obtain respective values.

**Table 5. Case number definitions**

Case	Location	Frequency, MHz	Cone			Maser
			Model	SN	Mod	
1	Venus DSS	2388	SPR	01	02	—
2	Mars DSS	2388	SCU	01	01	1
3	Mars DSS	2295	SCU	01	01	1
4	Mars DSS	2295	SCU	01	01	2
5	JPL	2295	SMF	01	01	1

Figure 8 shows measured data points and a least-squares second-order curve fit of the low-noise gas tube noise temperature calibrations performed with the SPR cone at the Venus DSS. The gas tube noise temperature ( $T_G$ , °K) is evaluated from the expression

$$T_G = T_{op}(Y_G - 1) \quad (1)$$

where

$T_{op}$  = operating noise temperature, °K

$Y_G$  = power ratio with the gas tube turned on and off

The computed value of the least-squares curve fit at the mid-point of the operating period is 4.02°K.

### E. JPL System Checkout of S-Band Multifrequency Cone (SMF SN1 Mod 1), C. T. Stelzried, T. Y. Otoshi, and K. B. Wallace

#### 1. Introduction, C. T. Stelzried

The S-band multifrequency (SMF) cone (Fig. 9) was modified at JPL for polarization diversity to support the *Pioneer VI* superior conjunction solar-corona faraday rotation measurements (SPS 37-53, Vol. II, pp. 69-71) and was installed at the Mars DSS on September 17,

1968. This cone can receive or transmit right-handed circular polarization (RCP), left-handed circular polarization (LCP), or rotating linear polarization (RLP).

The polarization diversity was obtained with two rotary quarter-wave plates (with remote control and readout capability) using three rotary circular waveguide joints. The system is designed for automatic servo polarization tracking using an error channel in the DSS receiver. An error S-curve has been demonstrated with a receiver at JPL. The servo system will be installed at the Mars DSS at a later date.

#### 2. System Checkout Test, C. T. Stelzried and K. B. Wallace

Figure 10 is a photograph of the cone undergoing system tests at JPL. A summary of the 15 system-temperature measurements (preliminary data reduction using the CTS20B computer program) taken between September 1 and 13, 1968, is shown in Figs. 11 and 12. The averaged total system temperature taken at zenith, on the ground, and with clear weather is 18.5°K. Improvements have been made in the built-in reflectometer system. Figure 13 shows a graph of the reflectometer tuning versus inside cone temperature. A null depth of approximately 37 dB at 2295 MHz was observed with the RLP system (lower quarter-wave plate set at 45 deg; upper quarter-wave plate adjusted for a null).

#### 3. Waveguide Calibrations, T. Y. Otoshi

Detailed insertion loss measurements of the final waveguide assemblies were not performed. However, some estimates of line losses were obtained from application of the radiometric loss evaluation method that uses two thermal noise sources. These line losses are discussed in Subsection 4.

Measurements of system voltage reflection coefficients were performed at 2295 and 2388 MHz.<sup>3</sup> These were made with the reflectometer, placed on port  $\triangle 1$  for maser 1 and port  $\triangle 6$  for maser 2, looking into the ambient load and into the antenna in its various polarization configurations. In addition, the reflection coefficients, as seen looking into the cryogenic load line and maser, have also been measured.

The results of the calibrated voltage reflection coefficient measurements<sup>4</sup> for the modified SMF cone at 2295 MHz are summarized in Tables 6, 7, 8, and 9. All tolerances shown are probable errors that include errors due to imperfect reflectometer tuning, imperfect sliding load, and an imperfect reflectometer attenuation standard.

Measurement dispersion errors are not included, but the  $3\sigma$  dispersion error is estimated to be less than 10%.

In some cases, the antenna reflection coefficients were difficult to repeat because they were sensitive to positioning of the polarizer plate angles. Table 6 shows that, under the RLP operating conditions, the reflection coefficients are functions of upper plate angle settings. This dependence can be partially explained by the antenna reflection coefficient at port  $\triangle 2b$  combining in and out

<sup>3</sup>2388 MHz data are documented by C. T. Stelzried, *et al.*, in *JPL System Checkout of S-Band Multifrequency Cone (SMF SN1 Mod 1)*, Oct. 10, 1968 (JPL internal document).

<sup>4</sup>C. Chavez assisted with the measurements.

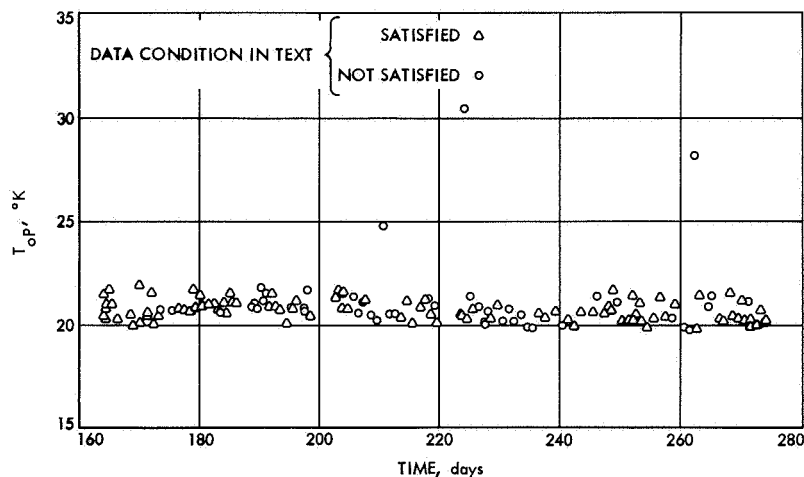


Fig. 7. Operating noise temperature of the SPR cone

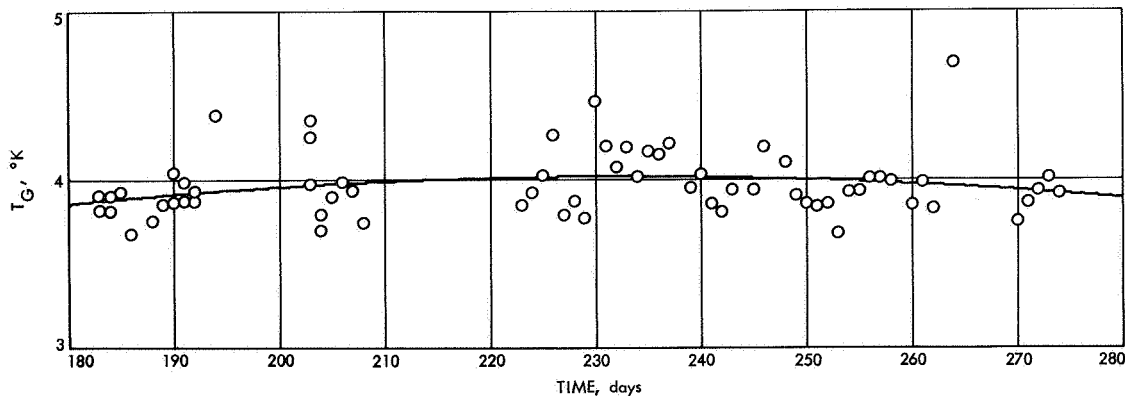


Fig. 8. SPR cone low-noise gas tube temperature versus time

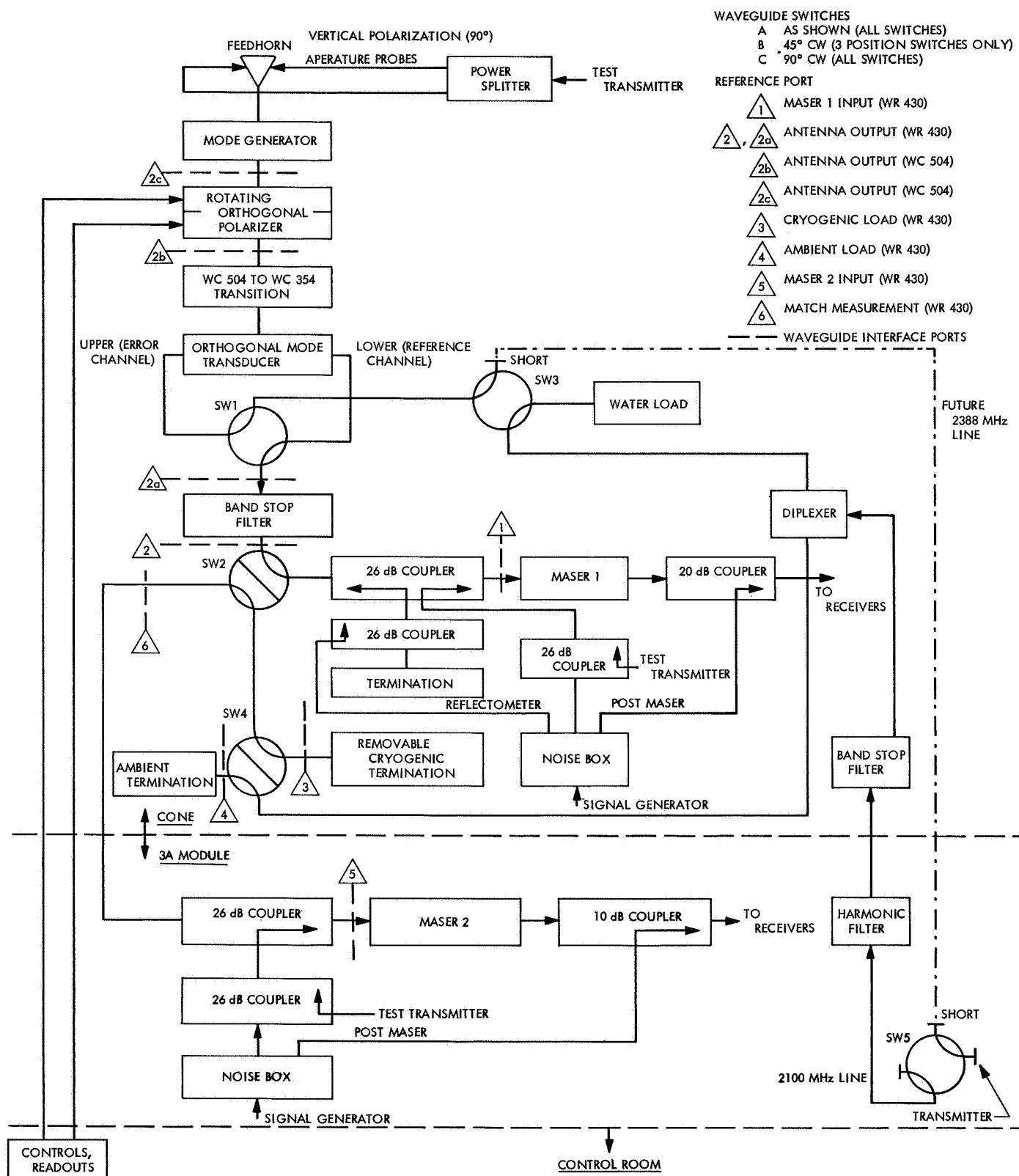


Fig. 9. SMF cone configuration

of phase with the resultant reflection coefficient generated by the components between ports  $\triangle 1$  and  $\triangle 2b$  (Fig. 9). In the RLP configuration, the antenna reflection

coefficient, as seen at port  $\triangle 2b$ , is approximately the same in magnitude as the mode generator reflection coefficient (0.05) at port  $\triangle 2c$ .<sup>5</sup> However, because of the two quarter-wave plates, the phase angle of this reflection coefficient will change 2 deg for each degree of rotation of the upper plate. Hence, it should be expected that when the upper plate is rotated in the RLP configuration, the maximum and minimum reflection coefficient, as seen at port  $\triangle 1$ , will occur at upper-plate angle settings separated by 90 deg.

#### 4. Component Noise Temperature Calibrations,

C. T. Stelzried and T. Y. Otoshi

Maser and antenna noise temperature calibrations were performed with a WR 430 waveguide liquid helium-cooled termination (Fig. 14) and an ambient termination. Manual switching of the two terminations directly at the maser port  $\triangle 1$ , using the Y-factor measurement technique, resulted in a calibrated maser temperature, and  $\pm$  total probable error, of  $4.6 \pm 0.2^\circ\text{K}$  at 2295 MHz. The total probable error includes the uncertainty of the helium load temperature as defined at the output of a 180-deg waveguide bend that was used in this laboratory calibration.

After installation of the maser into the cone, and with the helium load connected at port  $\triangle 3$  as shown in Fig. 9,

<sup>5</sup>Measurements indicate that the broadband mode-generator has a voltage standing-wave ratio (VSWR) of 1.10 at 2295 MHz, but that the quarter-wave plates are very well matched. For example  $|\Gamma_1|$  and  $|\Gamma_{11}|$  of each plate is 0.002 at 2295 MHz. The VSWR of the orthomode-cosine taper assembly is about 1.07.

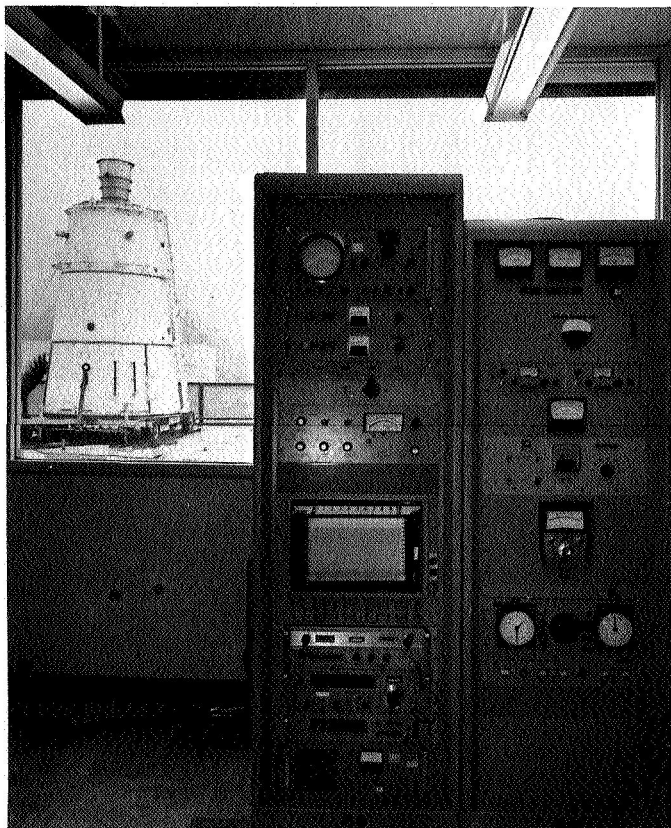


Fig. 10. SMF cone during system checkout at JPL

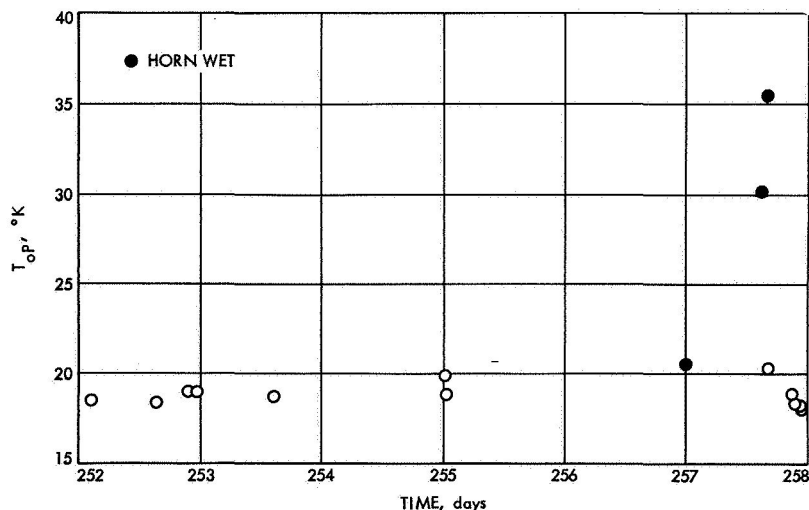
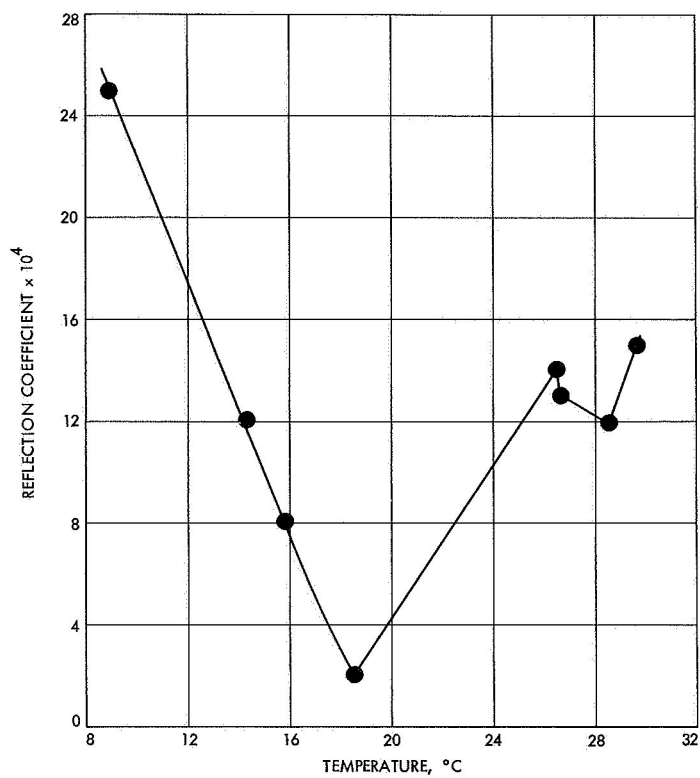


Fig. 11. Operating noise temperature of SMF cone

CODE 10 FOR NO. 1 FOR YES													
STA.	CONE	CONFIG.	POLAR.	OP.	FREQ. (MHZ)	MISSION							
TIME	HUM.	TEMP.	(C)	PR	PU	WTHR.	EL	GND.	AMB	ANT	(DB)	(K)	(K)
(GMT)	(PCT)												
10 SMF/01/01	-0	LIN		KBW	2295.00		0	1	48.0	26.1	49.4	0.04	18.58
252/2/30				0	0	1	1	0				0.23	SAT 1 BLDG 238AIL
10 SMF/01/01	-0	LIN		CTS	2295.00		0	1	51.5	25.5	50.5	0.04	18.41
252/15/30				0	0	1	1	0				0.21	TEST 2 AIL
10 SMF/01/01	-0	LIN		CTS	2295.00		0	1	51.1	26.5	50.1	0.04	18.96
252/21/45				0	0	1	1	0				0.22	TEST 3 AIL
10 SMF/01/01	-0	LIN		CTS	2295.00		0	1	45.0	26.4	50.2	0.04	18.92
252/23/30				0	0	1	1	0				0.25	TEST 4 AIL
10 SMF/01/01	-0	LIN		CTS	2295.00		0	1	49.4	25.4	50.4	0.04	18.70
253/14/45				0	0	1	1	0				0.22	TEST 5 AIL
10 SMF/01/01	-0	LIN		KBW	2295.00		0	1	48.3	26.2	50.8	0.04	19.91
255/0/20				0	0	1	1	0				0.22	TEST 6 RFSPUR AIL
10 SMF/01/01	-0	LIN		KBW	2295.00		0	1	48.8	23.3	51.0	0.03	18.79
255/0/45				0	0	1	1	0				0.24	TEST 7 AIL
10 SMF/01/01	-0	LIN		GAG	2295.00		0	1	46.9	29.4	50.9	0.03	20.55
257/0/10				0	0	1	1	0				0.53	TEST 8 SIG GEN UNSTABLE
10 SMF/01/01	-0	LIN		KBW	2295.00		0	1	58.0	13.0	50.0	0.03	30.28
257/14/50				0	0	1	1	0				0.28	TEST 9 HORN WET
10 SMF/01/01	-0	LIN		KBW	2295.00		0	1	63.0	13.3	50.3	0.03	35.64
257/15/50				0	0	1	1	0				0.34	TEST 10 HORN WET
10 SMF/01/01	-0	LIN		KBW	2295.00		0	1	62.3	23.7	50.2	0.03	20.31
257/16/20				0	0	1	1	0				0.22	TEST 11 HORN WATER REMOVED
10 SMF/01/01	-0	LIN		KBW	2295.00		0	1	56.0	25.2	50.6	0.01	18.92
257/21/0				0	0	1	1	0				0.28	TEST 12 T ON RCVR
10 SMF/01/01	-0	LIN		GAG	2295.00		0	1	56.1	25.4	50.2	0.03	18.45
257/21/35				0	0	1	1	0				0.22	TEST 13 YGIL=
10 SMF/01/01	-0	LIN		KBW	2295.00		0	1	70.0	25.4	50.2	0.03	18.36
257/21/35				0	0	1	1	0				0.22	TEST 14 T ON RCVR
10 SMF/01/01	-0	LIN		KBW	2295.00		0	1	54.0	25.3	50.5	0.03	18.10
257/22/50				0	0	1	1	0				0.21	TEST 15 T OFF RCVR
10 SMF/01/01	-0	LIN		KBW	2295.00		0	1					YGIL=.84 YGILH=4.65
257/23/0				0	0	1	1	0					

Fig. 12. Summary of SMF cone receiving system daily noise temperature calibrations







**Fig. 13. Graph of the reflectometer tuning versus inside cone temperature**

**Fig. 14. Liquid helium load assembly installed in SMF cone**





**Table 6. Antenna reflection coefficients defined at input port**


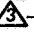
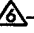
Antenna line configuration	Input-to-output path (see Fig.9)	Antenna polarization			Maximum/minimum voltage reflection coefficients
		Receive mode	Lower plate angle, deg	Upper plate indicated <sup>a</sup> angle, deg	
Maser 1 Normal receive path (reference channel)	Port  to feed-horn output via SW 2, SW 1, and lower orthomode transducer	RCP	0	270	0.0172 ± 0.0008
		LCP	0	0	0.0172 ± 0.0008
		RLP	45	25.0	0.0359 ± 0.0015
				110.8	0.0562 ± 0.0021
				209.2	0.0359 ± 0.0015
				299.4	0.0562 ± 0.0021
			315	71.4	0.0363 ± 0.0015
				169.4	0.0575 ± 0.0021
Maser 1 Orthogonal polarization path	Port  to feed-horn output via SW 2, SW 1, and upper orthomode transducer	CP	0	270	0.0367 ± 0.0015
		CP	0	0	0.0394 ± 0.0016
		RLP	45	49.6	0.0822 ± 0.0028
				136.7	0.0110 ± 0.0006
				234.2	0.0851 ± 0.0029
				315.0	0.0111 ± 0.0006
			315	42.3	0.0822 ± 0.0028
				132.5	0.0112 ± 0.0006
Maser 2 Orthogonal polarization path	Port  to feed-horn output via SW 2, SW 4, diplexer, SW 3, SW 1, and lower orthomode transducer	CP	0	270	0.0462 ± 0.0018
		CP	0	0	0.0432 ± 0.0017
		RLP	45	43.7	0.0014 ± 0.0002
				143.0	0.0891 ± 0.0030
				233.0	0.0015 ± 0.0002
				315.0	0.0891 ± 0.0030
			315	49.6	0.0015 ± 0.0002
				136.6	0.0902 ± 0.0030
Maser 2 Normal receive path (error channel)	Port  to feed-horn output via SW 2, SW 4, diplexer, SW 3, SW 1, and upper orthomode transducer	CP	0	270	0.0617 ± 0.0022
		CP	0	0	0.0638 ± 0.0023
		RLP	45	37.1	0.1023 ± 0.0033
				132.2	0.0126 ± 0.0007
			315	66.4	0.1000 ± 0.0032
				330.6	0.0126 ± 0.0007


<sup>a</sup>Indicated upper plate angle is —45 deg with respect to the actual angle of the upper plate.


**Table 7. Ambient load reflection coefficients defined at input port**

Ambient load configuration	Input-to-output path	Voltage reflection coefficient
Maser 1 path	Port  -SW 2-SW 4-WR 430 ambient load	$0.0013 \pm 0.0002$
Maser 2 path	Port  -SW 2-SW 4-WR 430 ambient load	$0.0200 \pm 0.0009$

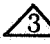

**Table 8. Cryogenic load transmission line reflection coefficients (matched load on output)**

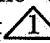

Cryogenic load line configuration	Input-to-output path	Voltage reflection coefficient
Maser 1 path	Port  -SW 2-SW 4-port 3	$0.0011 \pm 0.0006$
	Port  -SW 4-SW 2-port 1	$0.0014 \pm 0.0006$
Maser 2 path	Port  -SW 2-SW 4-port 3	$0.0202 \pm 0.0009$

noise temperature calibrations were again performed at 2295 MHz. By assuming that the maser temperature at port  remained unchanged, the cryogenic line loss

**Table 9. Maser assembly reflection coefficients defined at port **

Operating condition	Voltage reflection coefficient
Pump power turned on; maser is peaked at 2295 MHz	$0.067 \pm 0.002$
Pump power turned off; maser is peaked at 2295 MHz	$0.014 \pm 0.001$

between ports  and  was radiometrically determined to be  $0.085 \pm 0.005$  dB.

The antenna temperature at the maser reference port  via the error channel on a particular RLP setting was calibrated to be  $14.1 \pm 0.2^\circ\text{K}$ . If the effect of mismatches is neglected and an antenna temperature of  $5.0^\circ\text{K}$  at the horn aperture assumed, the antenna line loss contribution is calculated to be  $9.2^\circ\text{K}$  for the maser 1 error channel. However, because the phase of the antenna reflection coefficient at port  changes whenever the upper plate is rotated, a change in the system temperature will be observed.

No component noise temperature measurements were made at 2388 MHz.

## VI. Advanced Engineering: Supporting Research

### A. 210-ft Antenna Primary Reflector Structure Distortions Due to Thermal Differences and Wind Loadings, M. S. Katow

#### 1. Introduction

A method of analytically computing the distortions of the reflector structure under gravity loadings, using the STAIR structural computing program (Refs. 1 and 2) and the results of the RF performance evaluations by the RMS program (SPS 37-40, Vol. IV, p. 176 and Ref. 3), was described in SPS 37-52, Vol. II, pp. 86-92. This report describes the applications of this same method to compute deflections of the reflector structure caused by the thermal differences of the structural parts due to the sunlight exposures and by wind pressure loadings.

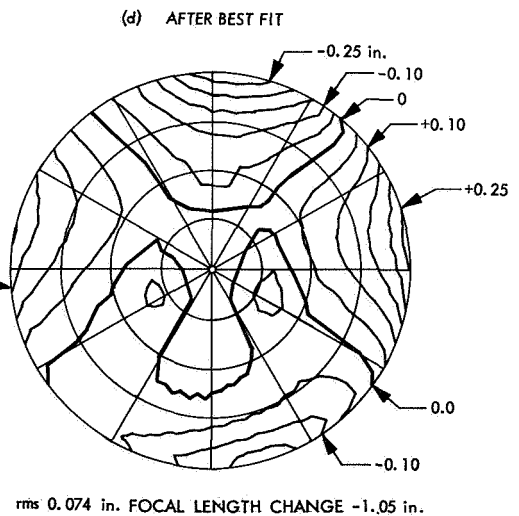
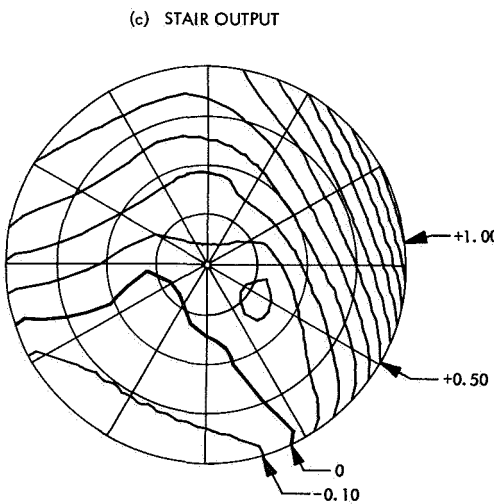
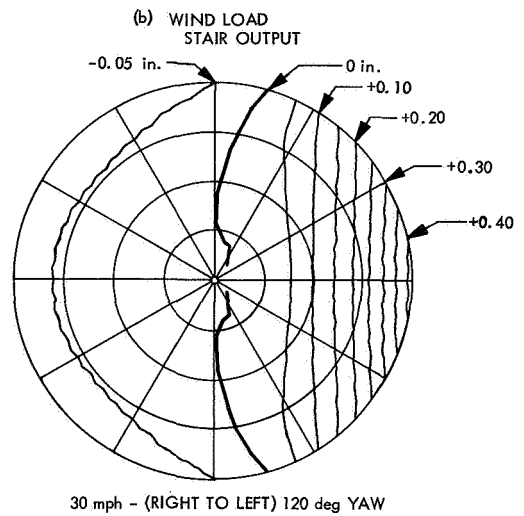
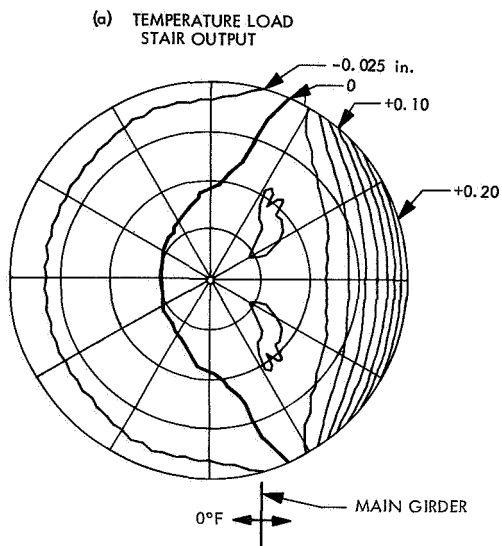
#### 2. Discussion

The thermal loading results from the differential expansion due to the temperature differences in the parts of the structure caused by unequal exposures to the sun's rays. Many tests using painted steel parts have shown that 10°F difference between the sun-lighted and shaded portions is a reasonable design number. The paint must, of course, have reasonable life as a "white" color and be applied at a specification thickness.

The thermal loadings input to computer analysis were the temperature differences of the truss elements. The temperature differences in this case were applied to all ribs outside the main girder on one side (right-hand side looking into the face of the reflector) only. This was assumed to result from the position of the sun at the right side at right angle to the symmetric axis of the reflector structure. The temperature difference at the outside chord of the ribs exposed to the sun was assumed to be +10°F; at the diagonals of the rib trusses, because of partial shading, to be at +5°F; and at the top chords next to the surface panels, in the shade, to be at 0°F. Figure 1a shows the plane of the main girder line which divided the rib trusses under the temperature loads from the sun-protected ribs. The hoop trusses were treated in the same manner as the ribs.

For the wind loads, the pressure coefficients were obtained from the pressure coefficient curves applicable to the percentage porosity of the 210-ft antenna as developed from the wind tunnel data.<sup>1</sup> The wind condition selected was the 30 mph also from the right hand side so as to add to the distortions of the thermal loads. The

<sup>1</sup>Fox, N. L., *Load Distributions on the Surface of Paraboloidal Reflector Antenna Wind Tunnel Tests*, January 1963 (JPL internal document).



**Fig. 1. Contour map of  $\frac{1}{2}$ -RF-pathlength errors**

maximum pressure case of 120-deg yaw angle as measured from the axis of symmetry of the reflector structure was used.

For the total distortion picture of all three environmental loadings, the horizon-look gravity distortions with the surface panels set to 45 deg previously reported (SPS 37-52, Vol. II) were added to the temperature and wind loadings.

### 3. Results

The computed results of the temperature loading are shown by contour levels in Fig. 1a and for the wind loading in Fig. 1b. For the worst-case addition of all three environmental loadings, Fig. 1c shows the contour levels with vectorially added distortion vectors resulting from no load to full loading. When the sum of the distortions are best fitted by the rms program, the residuals are shown by the contour levels in Fig. 1d with the resulting rms distortion and the change in focal length.

It should be pointed out that the above calculations do not account for the manufacturing tolerances of the surface panels and the actual deflections of the hyperboloid and their effects on the total performance.

### 4. Summary

In retrospect, the temperature difference picture assumed may not be conservative. However, estimated wind loadings used to develop pressure curves from cases tested in the wind tunnels did prove to be conservative. To check the actual pressure, differences will be measured on the 210-ft antenna in the near future so that a check on wind loads can be established.

For X-band use there is a possible performance gain during wind loading to be obtained by refocussing the hyperbola. This would require a servo-operation (with a small computer) as a function of the wind velocity and direction coupled with the antenna azimuth and elevation angle positions.

The combined manufacturing errors of the surface panels and the effects of the deflections of the hyperboloid computes into the performance results of Table 1.

### References

1. Lincoln Manual No. 48 "STAIR" (Structural Analysis Interpretive Routine). Lincoln Laboratory, Massachusetts Institute of Technology, Lexington, Mass., July 1962.

2. Katow, M. S., Bartos, K. P., and Matsumoto, R., *JPL Modified STAIR System—Operating Procedures*, Technical Memorandum 33-304. Jet Propulsion Laboratory, Pasadena, Calif., June 1, 1968.
3. Katow, M. S., and Schmele, L., "Utku-Schmele Paraboloid RMS Best-Fit Program," in Technical Report 32-979, Vols. I and II, p. 75. Edited by Ludwig, A., Jet Propulsion Laboratory, Pasadena, Calif., April 15, 1967.

Table 1. Performance results

Deviation	Surface distortion, in. (rms)
10°F + 30-mph wind + horizon gravity	0.074
Surface error at 45 deg elevation (manufacturing tolerance)	0.048
Effective focal length offset	0.080
RF feed lateral offset	0.040
Total	0.242

## B. Survey Technique for the 210-ft Antenna

**Azimuth Bull Gear, W. R. Bollinger, S. R. Paine, and C. C. Valencia**

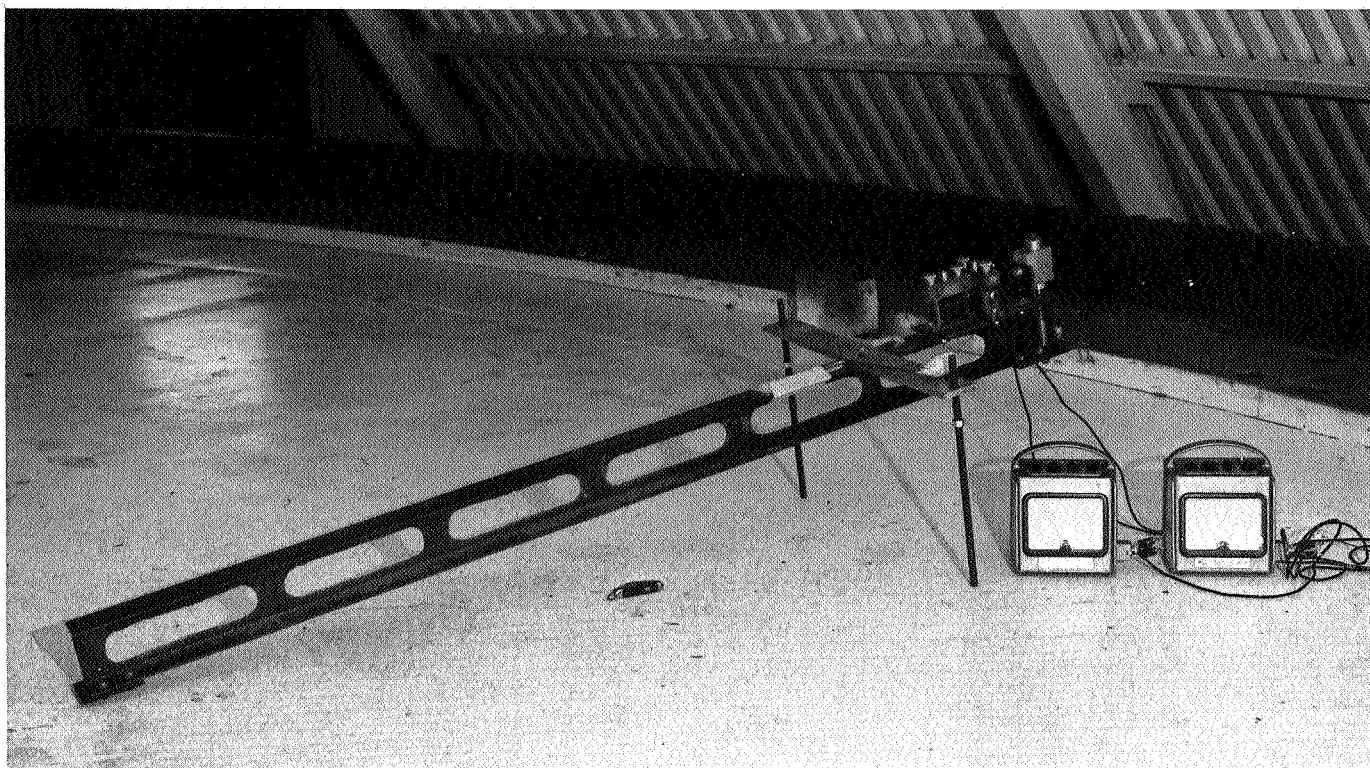
### 1. Introduction

Measurements of levels on the azimuth hydrostatic bearing runner of the 210-ft advanced antenna system (AAS) require a reference surface which can be used as a level datum. A groove was machined in the azimuth bull gear for this purpose, but because this groove itself is not level, it is necessary to survey it with respect to a true level plane to obtain corrections for measurements made from it.

The total survey process consists of determining the elevation of points at 10-deg intervals on the bull gear groove above a level reference datum plane, the further determination of points, at 3½-deg intervals, between the 10-deg points, and finally the determination of the elevation of the groove at ½-deg intervals. The data so obtained is entered on a cam compensation system which automatically corrects readings taken from the bull gear groove to a true level datum plane. Accuracies of the order of 0.001 in. are required. This article describes the method of surveying the bull gear groove at 10-deg intervals.

### 2. Azimuth Bull Gear Reference Groove

The azimuth bull gear on the 210-ft AAS is a 754-tooth, 3½-in. circular pitch spur gear approximately 70 ft in diameter mounted on steel supports embedded in the antenna pedestal concrete (Fig. 2). A continuous groove



**Fig. 2. Azimuth bull gear installation**

approximately  $\frac{3}{4}$  in. wide was machined on the top face of the bull gear rim using a cutting head mounted on one of the antenna alidade corner weldments. Vertical motion of the corner weldment, due to variations in the azimuth bearing runner elevation, prevented cutting this groove to a true level surface. The groove is 833 in. in diameter.

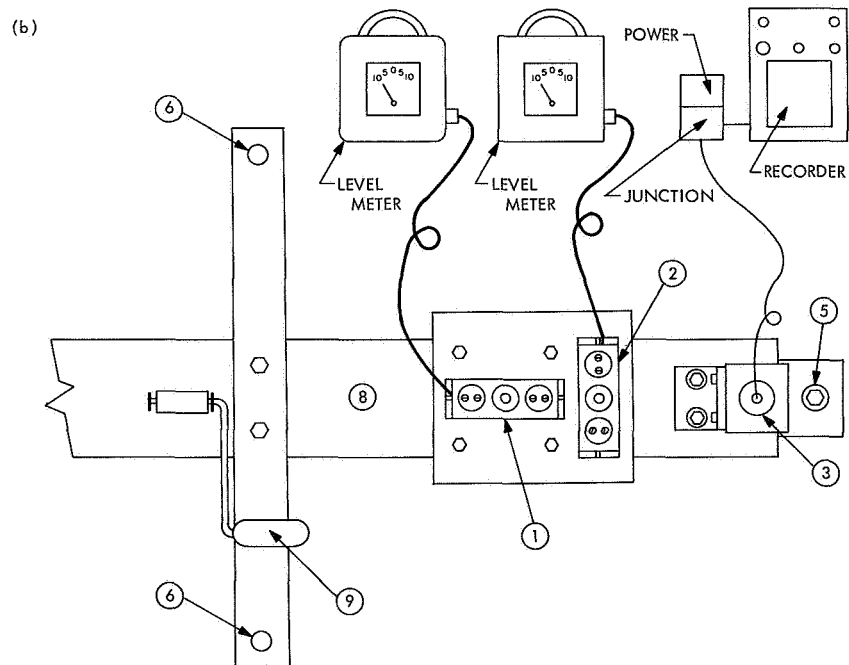
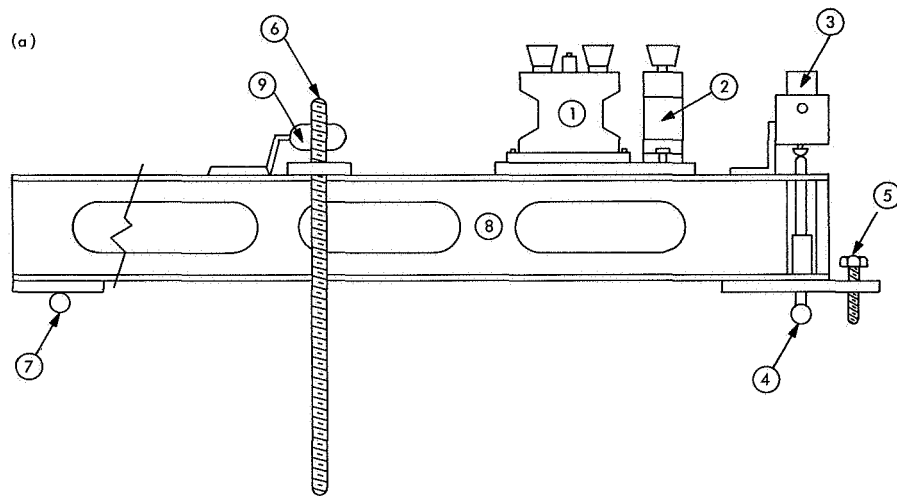
### **3. Surveying Technique**

*a. Survey method for 10-deg points.* The survey method for the 10-deg points consists of making a traverse around the runner groove, using a specially constructed precision level which spans exactly 10 deg on the gear groove. Level measurements are made midway between the alidade corner weldments, to minimize any deflections due to the bearing load on the pedestal. Work is done in the front bay (between the front two pads) because of available space. The survey data is recorded electrically on a strip chart recorder. In making a survey two or three complete traverses are made to eliminate accidental errors in individual points, and for the final reduction the averages of the sets of data are used.

*b. Precision level.* The precision level used in the bull gear survey consists of a 4-in. steel I-beam on which are

mounted adjusting screws, electronic levels, and a position transducer (Fig. 3). In use the I-beam is supported by a fixed tooling ball ⑦ at one end, and an adjusting screw at the other end, both resting in the bull gear reference groove. A cross-arm, with a counterweight ⑨ and cross-level screws ⑥ provides transverse support and adjustment. The cross-arm extends on both sides so that the level can be reversed with transverse support from the pedestal. A linear transducer ③ and a plunger with a tooling ball foot ④ resting on the gear groove measure the relative height of the end of the level above the gear groove. Tooling balls ④ and ⑦ are spaced 72.67 in. apart, equivalent to 10 deg on the gear groove. Two Talyvel electronic levels ① and ② are mounted on the I-beam. Talyvel ① is used with the leveling screw ⑤ to level the I-beam longitudinally while the Talyvel ② and cross-level screw ⑥ are used to level the beam transversely. The transverse level is necessary because of the sensitivity of the Talyvel levels to cross-level error.

The Talyvel level is a pendulum device, with a capacitor-type probe measuring the pendulum displacement. A power supply, detector circuit, and readout meter are contained in a separate box. Readouts are available in 25-arc-sec, 100-arc-sec, and 8-arc-min ranges. For the purposes of this level the 25-arc-sec range, with a 1-arc-



- |   |                         |   |                    |
|---|-------------------------|---|--------------------|
| ① | ② TALYVEL LEVEL         | ⑥ | CROSS-LEVEL SCREWS |
| ③ | PROBE                   | ⑦ | TOOLING BALL RIGID |
| ④ | TOOLING BALL (FLOATING) | ⑧ | 10-deg LEVEL BAR   |
| ⑤ | LEVELING SCREW          | ⑨ | COUNTERWEIGHT      |

**Fig. 3. Level arrangement: (a) top view (b) side view**

sec scale marking, is used for the longitudinal unit, and the 100-arc-sec range for the transverse unit.

The linear transducer used is a Collins Model SS-202 mounted in an aluminum cartridge. This is the same unit used in other runner measurements except that the plunger spring is removed so that there is no mechanical coupling between the floating tooling ball and the level structure. The transducer has an output of approximately 200 mV/0.001 in. over a range of  $\pm 0.100$  in. using a 24-V excitation. The transducer output is recorded on a Brush strip chart recorder to provide a permanent data record. Calibration of the transducer/recorder can be accomplished with a shim of known thickness slipped under the transducer plunger, or by placing the transducer and cartridge in a special calibration head, with displacements set in by a micrometer calibrated in 0.0001-in. increments. The usual recorder setting is 0.0005 in. per minor division.

*c. Setting up the level.* At the start of a survey the level is set up as follows:

- (1) The antenna is moved to an azimuth position from which 360 deg of motion in one direction is available. It is further positioned so that the center-line of the alidade, measured by the center structural support on the alidade windshield, is midway between two of the 10-deg points to be measured. The 10-deg points to be measured are previously established by bench marks on the bull gear.
- (2) The level is set on the bull gear with tooling balls ④ and ⑦ set on the 10-deg points.
- (3) The level is then set, using leveling screw ⑤ and cross-level screw ⑥ so that both Talyvels read zero.
- (4) The transducer is positioned so that the readout on the recorder is at the recorder electrical zero.
- (5) The level is then reversed, so that tooling balls ④ and ⑦ are on the opposite 10-deg points from the original setting. Using the adjusting screws it is releveled to zero on the Talyvel readouts.
- (6) The transducer reading on the recorder is noted, and the transducer cartridge is readjusted to move the recorder pen one half of the distance back toward zero.

The level and recorder are now set so that on an incline, if the level is adjusted to zero readings on the Talyvels, the recorder will indicate the elevation difference between the points on which the tooling balls rest.

*d. Running a traverse.* For each 10-deg step, the level is set with the tooling balls on the 10-deg points. The level is adjusted to zero on the Talyvels, and the transducer displacement recorded. The level is then reversed, releveled, and the transducer displacement again recorded. The elevation difference between the two 10-deg points, for this traverse, is taken as the average of the two chart readings. The sign of this difference is determined by the direction of the recorder offset.

This process is repeated from point to point, until, after 36 steps the traverse is closed on the starting point. The antenna is moved 10 deg at each step to keep the alidade centered on the 10-deg span being measured.

In each survey, two or three full traverses are made to identify and eliminate random errors.

*e. Data reduction.* The elevation difference data recorded is reduced to final elevations in the following steps:

- (1) The average of the elevation differences between the 10-deg points from each run is calculated.
- (2) Starting with the initial point as zero elevation, the elevation of each successive point is calculated from the elevation of the previous point and the average elevation difference between them. The difference between the thirty-sixth point so calculated and zero is the closure error since, ideally, the thirty-sixth and initial point should be the same.
- (3) One thirty-sixth of the closing error (if positive) is then subtracted from each average elevation difference. The corrected elevation differences are then stepped out for each 10 deg giving final elevations.

At the end of each complete traverse, a closing error for that traverse is calculated. Typical closing errors are less than 0.010 in. Larger values indicate that a rerun is required.

#### 4. Conclusions

The instrument and process described have been very successful. A lighter level beam would be an improvement, but there is concern that one made of aluminum, for example, would have problems with temperature variations. The sensitivity of the Talyvel level to cross-tilt has been studied more thoroughly, and a 10-s bubble might be used in cross-level in place of the second Talyvel.

Two surveys of the segment taken approximately 6 mo apart showed a considerable change in elevations. Part of this was random, apparently due to local changes in the bull gear support, and part was sinusoidal, which could reflect a tilt of the pedestal of the order of 1 arc sec (this tilt is too small to affect the antenna-pointing accuracy requirements). Further studies on these questions are under way.

### C. Electron-Beam Welding Test for Large Hydrostatic Bearing Runner Plates,

*C. J. McCaul, H. P. Phillips, and R. A. Zanteson*

#### 1. Introduction

The azimuth hydrostatic bearing runner for the 210-ft advanced antenna system (AAS) is constructed of 5-in. thick plates made up in eleven segments to form a circle 77 ft in diameter. A complex mechanical joint used between adjacent segments provides satisfactory structural properties but is both expensive to manufacture and subject to leakage problems in use. Manufacturing engineers at the Rohr Corp., the prime contractor on the 210-ft antenna installed at Goldstone DSCC, suggested that an electron-beam welding process, using a portable

vacuum chamber, might provide a more satisfactory field joint. A joint project between JPL and the Rohr Corp. was undertaken to test this method, and the results of this are reported in this article.

The major problem anticipated was maintaining flatness across the joint after welding. The allowable step at the joint is 0.0015 in. while the allowable warpage out of flat is limited to 0.003 in. over a 50-in. length. Surface roughness at the weld can be smoothed out by hand methods, but it is not practical to correct large scale warpage in the field.

#### 2. Joint Design

Considerable work has been done in the field of welding thick plates by the electron-beam process (Refs. 1 and 2), but these have been limited to plates of about 2 in. thickness because of the power limitations in available welding machines. To overcome this problem the Rohr Corp. manufacturing engineers developed a joint design (Fig. 4) in which the weld could be made in three phases. The first pass welds the lower half of the plates together. The second and third passes weld the insert to each of the two plates. While this design overcomes the thickness limitation, it introduces both a potential source

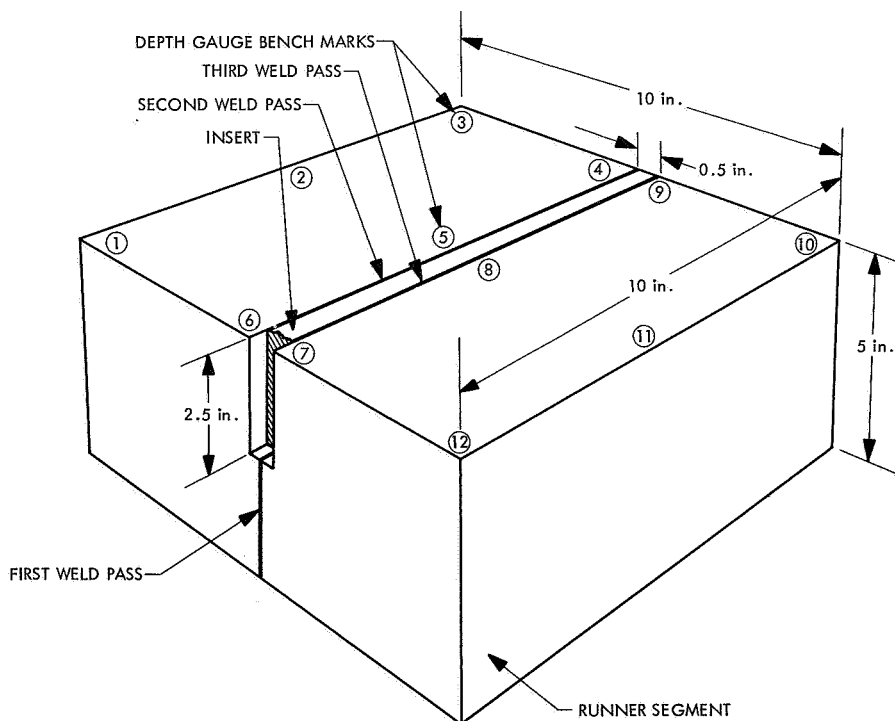


Fig. 4. Joint design (portion of insert shown cut away)

of warpage because of the unsymmetrical weld pattern and a structural discontinuity at the bottom of the insert. In general, the stress levels in the runner are very low, and it was believed that problems relating to the structural discontinuity could be determined by subsequent tests if the warpage problem was overcome.

### 3. Weld Test

The weld test was conducted at the Rohr Manufacturing Laboratory using a Sciaky 30-kW electron beam welding machine. A test sample reproducing the runner thickness, but 10 in. square (Fig. 4) made of A36 steel (the same material used for the actual runner) was prepared. The insert was fit to the joint with approximately 0.002-in. clearance. Benchmarks for warpage measurements were etched on the material in the locations shown.

The settings used for making the welds are listed in Table 2.

**Table 2. Weld machine settings**

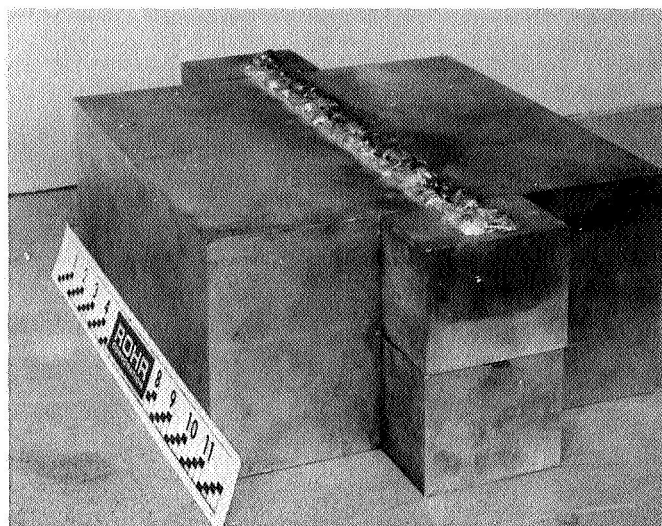
Measurement	Setting
Chamber vacuum	$3 \times 10^{-5}$ torr
Accelerating voltage	57 kV
Beam current	515 mA
Head travel setting	14½ in./min
Focal point (below top surface)	1½ in.
Energy per lineal inch of weld	121.5 kJ/in.
Penetration (estimated)	2.61 in.

### 4. Test Results

Height gage measurements were made before and after the welding was completed to determine the amount of warpage resulting from the welding process. The results are shown in Table 3 and indicate a maximum warpage

**Table 3. Height gage measurements on bench marks**

Station	Measurement, in.		
	Before welding	After welding	Change
1	+0.0002	+0.012	+0.0118
2	+0.0001	+0.0115	+0.0114
3	0	+0.012	+0.012
4	-0.0001	+0.003	+0.0031
5	+0.0002	0	-0.0002
6	0	+0.002	+0.002
7	0	0	0
8	+0.0002	-0.0045	-0.0047
9	0	0	0
10	-0.0001	+0.0115	+0.0116
11	0	+0.0115	+0.0115
12	0	+0.0145	+0.0145



**Fig. 5. Specimen showing second and third weld passes**

along a line through points 3, 8, and 12. This is considerably beyond the acceptable amount. Figure 5 shows the specimen after welding, and Fig. 6 shows specimens after sectioning and polishing. The porosity is attributed to nonmetallic inclusion in the steel.

### 5. Conclusions

From the results of this test it is concluded that this method of welding is not suitable for use in joining the segments of the hydrostatic bearing runner. Not only is the surface warpage excessive, but the porosity of the resultant welds make the structural integrity of the weld questionable.

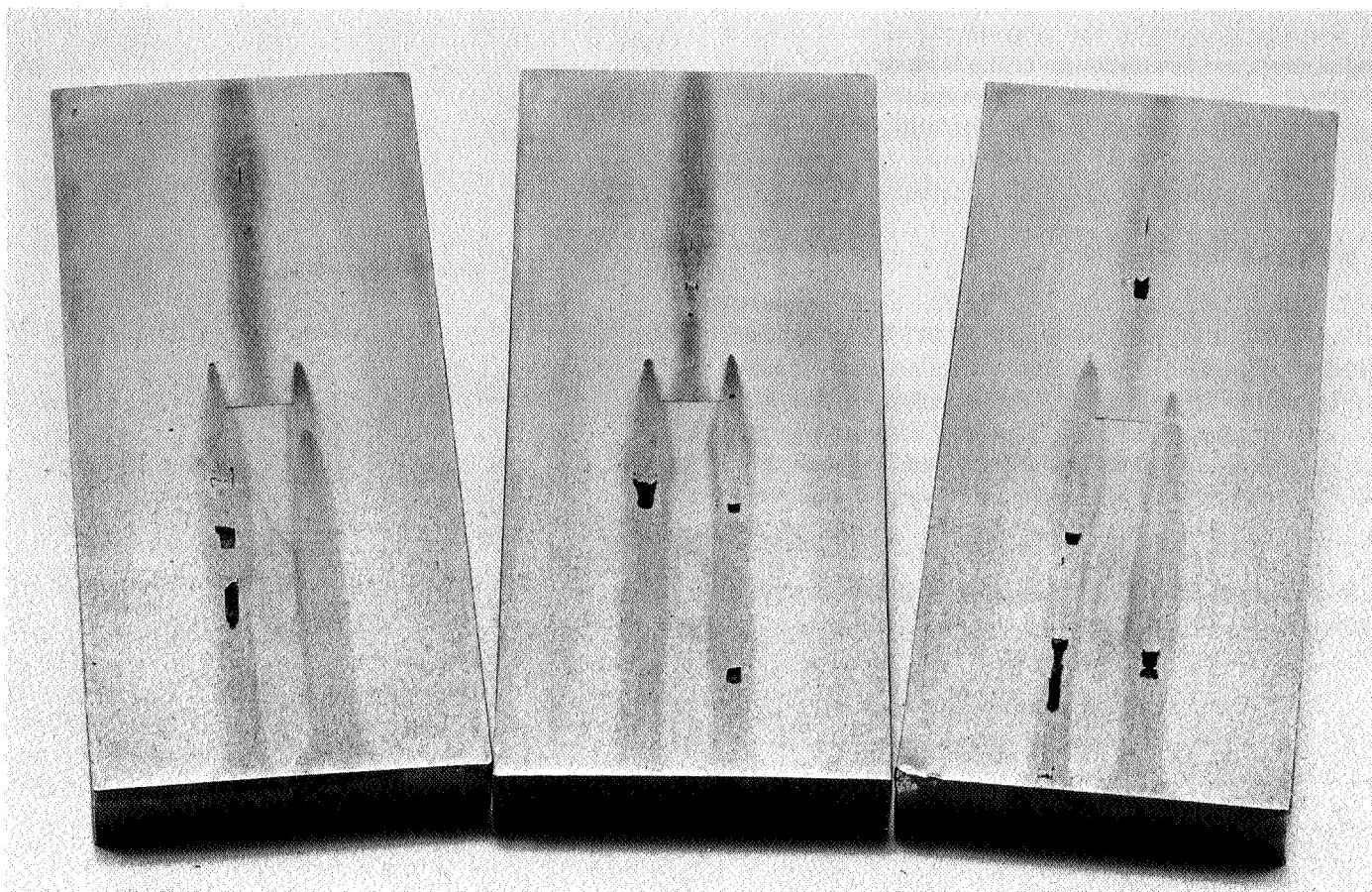
### References

1. Groves, M. T., and Gerken, J. M., *Evaluation of Electron Beam Weld in Thick Materials*, Thompson Ramo-Wooldridge, Inc., Technical Report AFML-TR-66-22, 1966.
2. *Evaluation of 2" Thick Electron Beam Weldments*, Applied Research Laboratory, United States Steel Corp., Monroeville, Penn. Publication AD604875, U.S. Department of Commerce.

### D. Voltage-Controlled Phase Shifter, C. E. Johns

#### 1. Introduction

There are numerous variable phase shifters used within the receiver portion of the S-Band receiver/exciter/ranging subsystem and the subcarrier demodulator assembly. Their function is to allow adjustment of the phase



**Fig. 6. Polished cross sections of welds**

relationship between a locally generated reference frequency and a received RF signal applied to a phase-coherent detector.

The phase shifters presently used are separate sub-assemblies and operate electromechanically. The reference signal is applied to the input of a mechanical phase resolver so that, by mechanical rotation of a shaft, the phase resolver can be continuously varied. Due to the large signal insertion loss of the resolver, each subassembly also contains several tuned amplifiers to give the desired reference power level at the output terminal.

Although the present phase shifters perform satisfactorily, they are physically large and would be inconvenient for use in future systems where volume will be at a premium. Also, remote automatic phasing is now under consideration for automatic checkout. The present phase shifters do not lend themselves conveniently to this purpose. To reduce the problems posed by the present

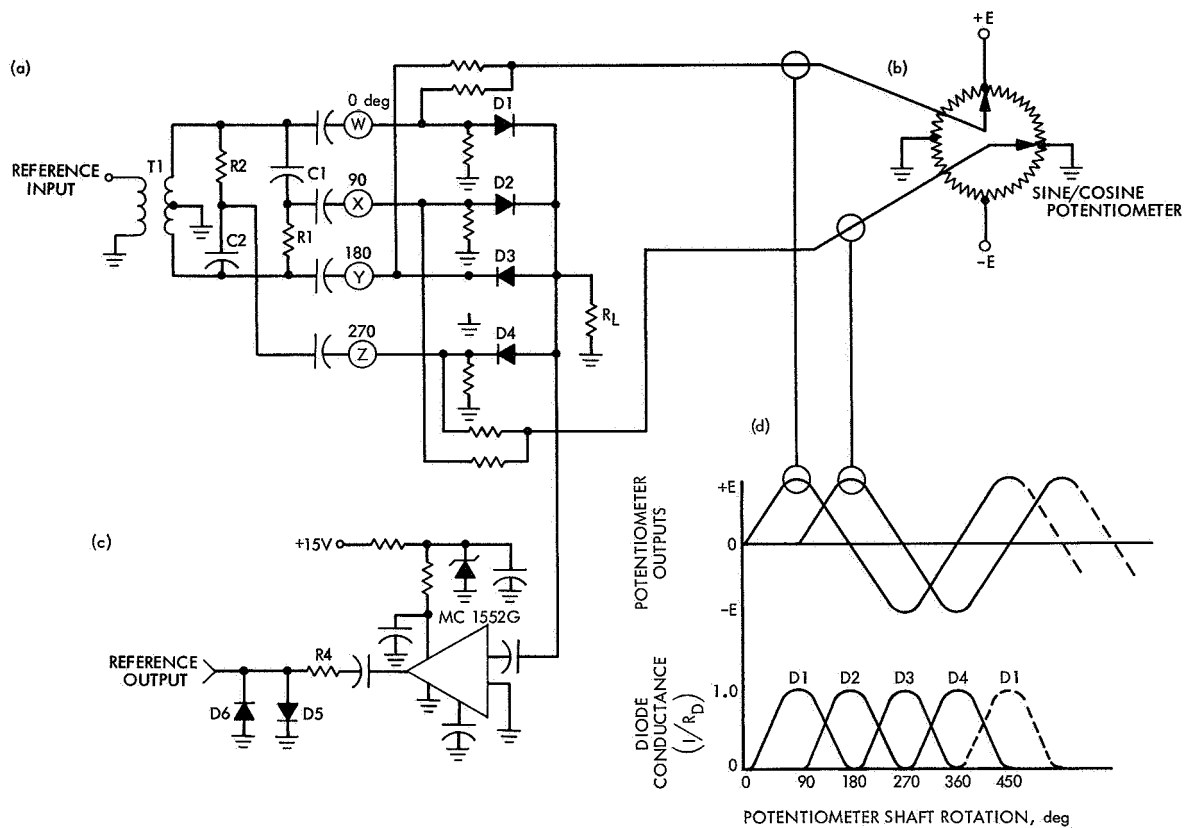
shifters, a continuously variable voltage-controlled phase shifter has been developed.

## **2. Design and Operation**

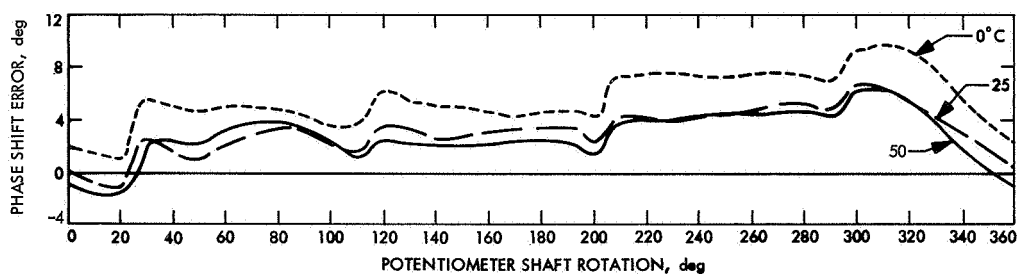
The design goals for the voltage-controlled phase shifter were:

- (1) It must be continuously controllable through 360 deg by application of dc voltages.
- (2) The RF circuit volume must be small enough to combine with a phase detector, thereby eliminating the phase shifter subassembly.
- (3) Phase stability must be within  $\pm 10$  deg over the temperature range of 0 to 49°C at any phase setting (the present phase shifter specifications).
- (4) The basic circuit must be applicable to any reference input frequency from 100 kHz to 10 MHz.

The operation of the shifter is best described in Fig. 7. The dc voltage applied to diodes D1, D2, D3, and D4 is



**Fig. 7. Voltage-controlled phase shifter schematic**



**Fig. 8. Phase shift error versus potentiometer rotation**

supplied from the armatures of the sine/cosine potentiometer R3. As the potentiometer shaft is rotated through 360 deg, it causes the conductance of each diode to vary sequentially, as shown in Fig. 7d.

Reference signals are applied to the diodes at terminals W, X, Y, and Z. Each of these are the same signal with a 90-deg phase difference between them. These signals are vectorially summed across the load resistor  $R_L$ . For example, as the potentiometer shaft is rotated from 0 and 90 deg, diode D1 goes from zero to full conduction, and the signal appearing across  $R_L$  will be that which is applied to terminal W (0 deg). Shaft rotation from 90 to 180 deg will turn diode D1 off and D2 on. As this occurs, the effective resistance of D1 is increasing and that of D2 is decreasing. Since the resistance of each diode is a function of the applied forward dc voltage  $R_D = f(E_{dc})$ , the resultant signal across  $R_L$  is

$$E_{RL} = E \left[ (\sin \omega t) \frac{R_L}{R_{D1} + R_L} + (\sin \omega t + 90) \frac{R_L}{R_{D2} + R_L} \right]$$

where  $E$  is the signal amplitude applied to terminals W and X. For a shaft rotation from 90 to 180 deg, the resultant signal across  $R_L$  varies from 0 to 90 deg. For a shaft rotation from 180 to 270 deg, the same action takes place between diodes D2 and D3, and the signal across  $R_L$  changes from 90 to 180 deg. Between 270 and 360 deg, the action is repeated between D3 and D4. From 360 to 90 deg, it occurs between diodes D4 and D1. Since the potentiometer has no stops, the reference signal phase can repeatedly be varied through 360 deg.

A linear integrated circuit (Fig. 7c) is used to amplify the small signal across  $R_L$  to a suitable level. The output of the amplifier is applied across R4 and diodes D5 and D6, which serve as amplitude limiters to reduce the reference signal amplitude variations due to potentiometer rotation. The quadrature signals applied to terminals W, X, Y, and Z are generated by transformer T1 (Fig. 7a) and the phase lead and lag networks  $R_1, C_1$  and  $R_2, C_2$ . To change the operating center frequency of the phase shifter, it is necessary to change only the values of  $C_1$  and  $C_2$  (Fig. 1a) to assure a 90-deg phase lead and lag. Circuitry is minimal, and requires little more than 1 in.<sup>3</sup> packaging space, which is small enough to allow its installation within a phase detector.

The phase shift error versus potentiometer shaft rotation and temperature variations is shown in Fig. 8. As

shown, the phase shift at any potentiometer shaft setting is well within the design goal of  $\pm 10$  deg over the temperature range.

DC voltages to the diodes can be supplied from two digital-to-analog converters, rather than from a sine/cosine potentiometer, thus allowing it to be programmed for automatic checkout.

### 3. Conclusion

The voltage-variable phase shifter meets the design requirements. Its small size will eliminate the need for individual phase shifter subassemblies and therefore reduce equipment size and costs. It can be controlled remotely, either manually or by computer control, which will give increased flexibility to future receivers.

**E. Venus DSS Activities, R. M. Gosline, M. A. Gregg, and E. B. Jackson**

### 1. Experimentation

During the period of August 16 through October 15, 1968, the Venus DSS, using its 85-ft az-el antenna, conducted monostatic and (with the Mars DSS) bistatic planetary radar experiments. In addition, measurements of average peak signal strength, repetition rate and pulse period of all known pulsars continued. In particular, continuing studies were made of CP0950, CP0328, and AP2015. The pulse-to-pulse periods for these three have been determined at S-band with a resolution of 2 ns. Additionally, average flux density has been measured and studies of long-term scintillation are under way.

Ephemeris update tracking with the 85-ft antenna was unsuccessful on moving sources, although earlier tests with a test transmitter at the Venus DSS's collimation tower were satisfactory (SPS 37-48, Vol. II, pp. 152-153). Software problems unrelated to the basic concept involved were the reason and are currently being corrected.

The 30-ft antenna continued to be used for time synchronization transmissions to the National Bureau of Standards at Boulder, Colorado and the Tidbinbilla DSS in Australia.

During the first two weeks in October the 85-ft antenna was fitted with a maser, receiver, and associated feed cone for reception at 8448 MHz, and antenna performance at this frequency is being evaluated.

## 2. System Performance

**Digital systems.** Some difficulty was experienced with power line transients during starting of the new 500 kV-A motor generator to be used on the X-band transmitter, but tailoring of the starting cycle intervals reduced these transients sufficiently to prevent loss of operation of the digital systems during the starting phase.

## 3. System Improvements

**a. Digital systems.** The memory size of the SDS 930 computer has been expanded from 8,192 words to 16,384 words.

The station control and monitor (SCAM) subsystem was improved by the addition of a line driver chassis, time-input selection switch, and an audible operation code monitor.

**b. Transmitting systems.** The following modifications were made to the S-band transmitter:

- (1) The beam running time meter was modified to operate only when the beam is in the "raised" condition to eliminate the time logged against the tube when the beam was on at only 3 kV.
- (2) The collector monitor circuits were modified with nonindicative type shunts to prevent loss of meter movements.
- (3) A new beam warning automatic control panel was installed in remote cabinet for computer operation.

## F. 500-kW Motor-Generator for X-Band Time Synchronization Transmitter, R. E. Arnold

### 1. Introduction

Until recently, the X-band time synchronization transmitter on the Venus DSS 30-ft antenna has been using essentially the same equipment that had been used during the 1964-1965 lunar radar mapping experiment (SPS 37-35, Vol. III, pp. 64-65). This report describes the new motor-generator (MG) recently installed that gives the system an immediate 25-kW RF capacity. During the next calendar year, the RF output power will be increased to 100 kW through the procurement of a new klystron transmitter and installation of an existing larger water-to-air heat exchanger.

## 2. Description

A 60- to 400-Hz, 500-kW synchronous MG set, with motor starting and generator controls, was built by a contractor according to JPL specifications and has been installed on a reinforced concrete pad near the 30-ft antenna. The motor and generator characteristics are shown in Table 4.

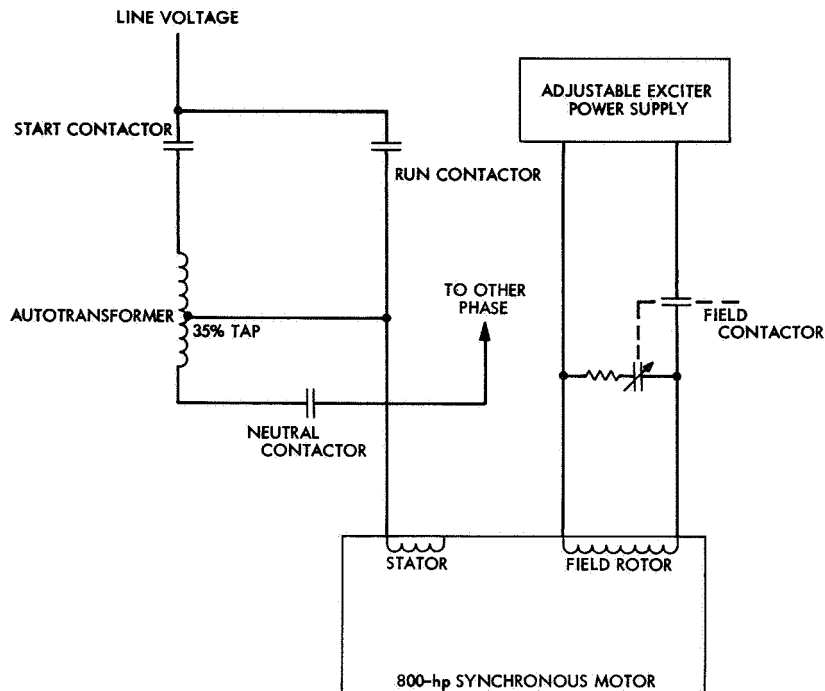
Table 4. Motor and generator characteristics

Characteristic	Motor	Generator
	Synchronous 3-phase, reduced voltage induction start	Synchronous 3-phase
Rated power	800 hp	500 kW at 0.8 power factor
Synchronous speed	1200 rpm	1200 rpm
Voltage, In-In	480 V	2400 V (variable)
Frequency	60 Hz	400 Hz
Line current at rated power	75.4 A at 1.0 power factor	150 A at 0.8 power factor
Field current at no load	24.5 A at 87 V	49.6 A at 89 V
Field current at full load	35.4 A at 125 V	84 A at 150 V

### 3. Motor Starting Transients

The motor as delivered did not meet JPL's requirement of a maximum 500 kV-A for starting transients. The motor-starting equipment uses a three-phase autotransformer with 35% taps and several contactors to reduce starting transients. Figure 9 is a simplified diagram (single-phase case) of the autotransformer starting equipment. The starting controls, as originally installed, provided the following sequential operations to start and synchronize the motor to the line:

- (1) The start and neutral contactors are closed. This applies 35% of the line voltage to the motor. Figure 10a is the line current for the first 4.5 s of the start cycle; except for the initial inrush, line current is 500 A (415 kV-A for the three phases).
- (2) After accelerating for 150 s from the start of step (1) to about 98% of synchronous speed, the neutral contactor is opened, the run contactor is closed, and the start contactor is opened.
- (3) A field current of 24.6 A is applied by closing the field contactor. The motor then accelerates to synchronous speed and a 1.0 power factor is obtained. It is a characteristic of this particular motor (Table 4) to operate at unity power factor when running at rated speed and 24.6 A of field current.



**Fig. 9. Motor starting equipment, simplified diagram**

Figure 10b shows the line current just prior to step (2) and continuing through step (3). During this period, the average rms current is approximately 900 A (700 kV-A for the three phases).

#### 4. Modified Start

The starting transients in steps (2) and (3) above were reduced to under the 500 kV-A maximum requirement by interchanging steps (2) and (3). The modified sequence is:

- (a) Same as the previous step (1).
- (b) After 135 s the field contactor is closed, and 8 A of current is applied to the field. The motor accelerates to synchronous speed prior to step (3).
- (c) 15 seconds after step (b), the neutral contactor is opened, the run contactor is closed and the start contactor is opened.
- (d) The motor field current is adjusted to 24.6 A for a 1.0 power factor.

Figure 10c shows the current during step (c); the field current was 8 A. Except for the inrush current during the

first 125 ms, the starting transient is less than 500 A or 415 kV-A.

Figure 10d shows the line voltage as monitored in the Venus DSS control room during step (c) of a modified motor start. Voltage drop was approximately 7% for 125 ms. The voltage drop does not interfere with the operation of the computers or other station equipment.

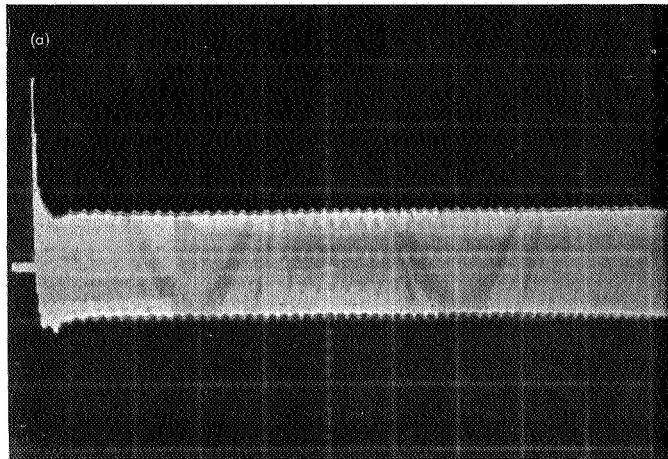
For the past month all starting of the MG set has been done using the modified starting procedure. The starting procedure is not fully automated at present, but it is currently being incorporated in the automatic starting controls. Presently it requires an operator to manually operate a switch to apply the field contactor at the end of 135 s [step (c)] and to adjust the motor field exciter for the different currents.

#### 5. Conclusion

Motor-starting transients can be reduced in an auto-transformer starting method by applying the motor field current prior to connecting the motor to the full-line voltage. This method of motor starting is being incorporated in the control circuitry for the Venus DSS's 500-kW MG set.

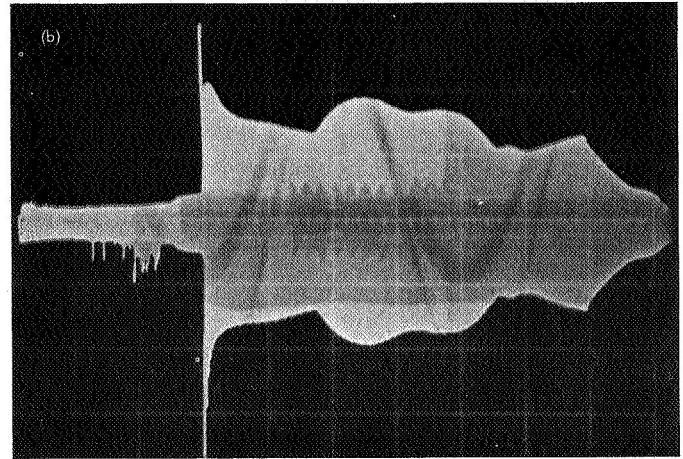
HORIZONTAL: 0.5 s/div  
VERTICAL: 300 A/div

HORIZONTAL: 0.5 s/div  
VERTICAL: 300 A/div



(a)

NEUTRAL AND START CONTACTORS CLOSING

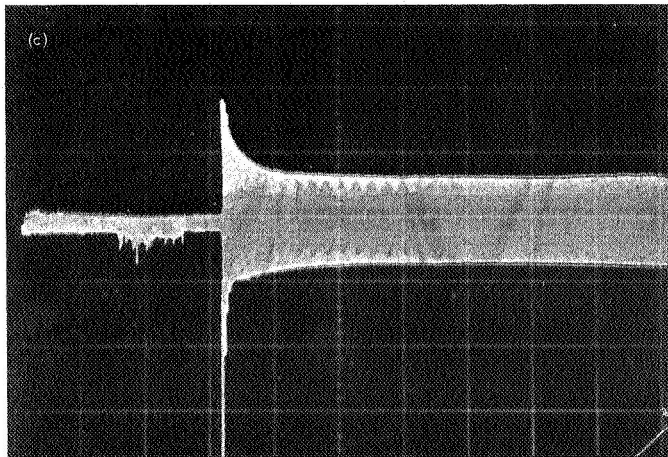


(b)

RUN CONTACTOR CLOSING

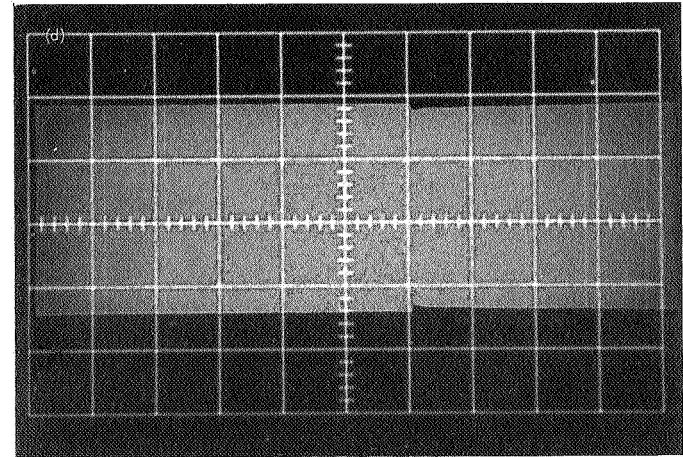
HORIZONTAL: 0.5 s/div  
VERTICAL: 300 A/div

HORIZONTAL: 0.5 s/div  
VERTICAL: 35 V rms/div



(c)

RUN CONTACTOR CLOSING



(d)

DROP CAUSED BY MOTOR STARTING

Fig. 10. Line current: (a) initial start, (b) normal start, (c) modified start, (d) control room line voltage



## VII. Network Development and Operations

### A. High-Rate Telemetry Project, R. C. Tausworthe

The following articles report the progress of the high-rate telemetry (HRT) project.<sup>1</sup> The test set configuration is described, some changes to the correlator design are given, the latest updates to the software are discussed, actual measured performance of the entire system in the compatibility test area is shown, and the effects of variation in subcarrier loop parameters on the subcarrier demodulator performance are described.

There have been no alterations in the project schedule. Field set I is en route to Cape Kennedy DSS to be installed and checked out for prelaunch spacecraft support. Field set II is in operation in the compatibility test area, giving performance identical to its predecessor. Laboratory set A is being updated to be the electrical equivalent of the two field sets.

### B. Test Equipment, R. I. Greenberg

#### 1. Physical Configuration

Figure 1 shows the final front panel configuration of the test equipment. The subassemblies are positioned from top to bottom as follows:

- (1) Power supply.

<sup>1</sup>Previous reporting on this project is given in SPS 37-48, Vol. II, pp. 83-130, SPS 37-49, Vol. II, pp. 115-127, SPS 37-51, Vol. II, pp. 127-157, and SPS 37-52, Vol. II, pp. 141-143.

- (2) Control.
- (3) Code generator.
- (4) Frequency counter.

A fan located at the top is provided to cool equipment within the cabinet.

#### 2. Controls

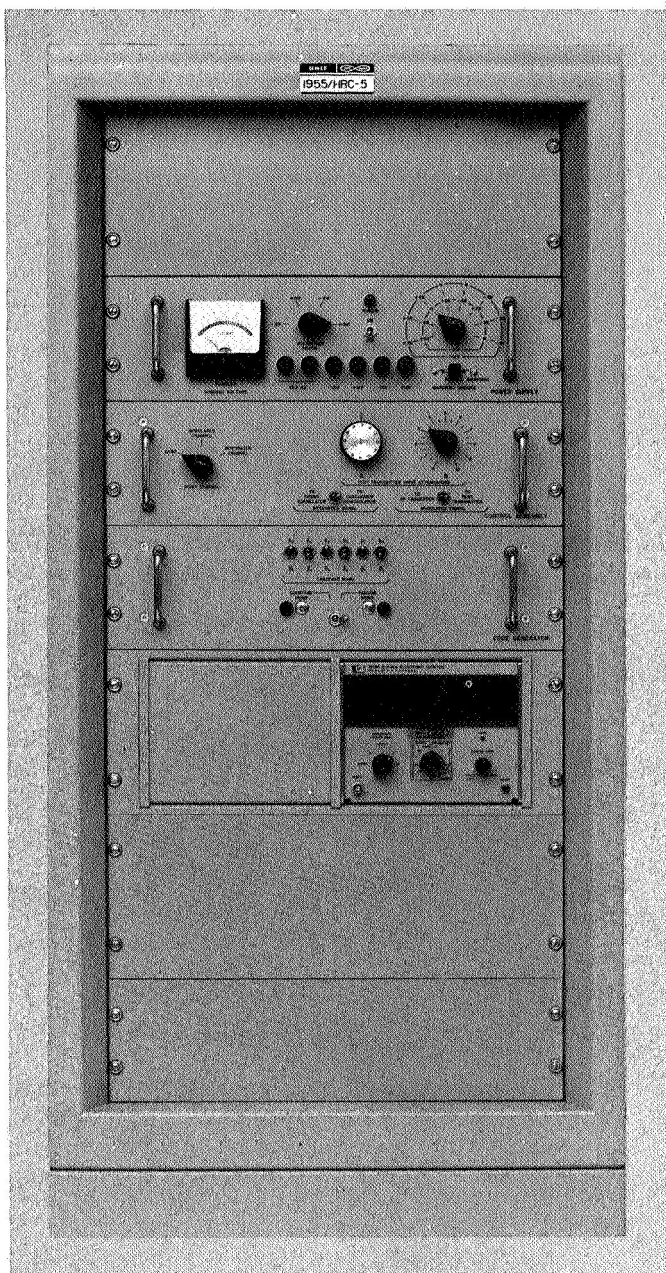
##### a. Power supply subassembly.

*Voltage readout meter and voltage selector switch.* The selector switch on the left may be positioned to choose any of the following four voltages for readout:  $\pm 12$  V  $\pm 15$  V. Normal reading will be "100," corresponding to the nominal voltage.

*Marginal voltage control.* The choice of marginal check voltages ( $\pm 12$  V) in all possible combinations may be made by the selector switch on the right. The marginal voltages are provided to check the logic circuitry of the code generator during preventive maintenance in order to anticipate faulty operation. The lever switch, located below the selector switch, overrides all positions of the selector switch. In the normal position, nominal  $\pm 12$  V only are available.

##### b. Control subassembly.

*The noisy channel selector switch.* When the noise generator and signal/noise mixer are properly connected, the



**Fig. 1. Front panel of test equipment**

selection of the noisy channel may be made by this switch. Note that only one channel may be chosen for noise addition. The other channel will be without noise.

*Selection of outputs.* This may be done by the two toggle switches located at the lower right. The left switch permits choice of outputs either to the cross correlator or to the subcarrier demodulator. The right switch permits choice of output either to the up converter or to

the test transmitter. Note that the choice of output by either switch does not affect the choice of output of the other switch.

*Attenuators.* The variable attenuators, located above the toggle switches, apply only to the test transmitter output. The other outputs are fixed.

*c. Code generator subassembly.* Two modes of operation are possible for the code generator subassembly.

*Mode choice toggle switch.* Either random word output or constant word output may be chosen by this switch, which is located at bottom center.

*Constant word choice switches.* This constitutes a grouping of six toggle switches, which provide the capability of choosing any one of 64 words for the output.

### 3. Outputs

All outputs are clearly marked with connector numbers and function description at the rear panels of the subassemblies. The outputs are:

- (1) To cross correlator from control subassembly.
- (2) To subcarrier demodulator from control subassembly.
- (3) To up converter from control subassembly.
- (4) To test transmitter from control subassembly.
- (5) Word sync from code generator subassembly.
- (6) Symbol sync from code generator subassembly.

Outputs listed (1) through (4) must be terminated by 50  $\Omega$  to obtain the output voltages required. Termination requirements for (5) and (6) are unspecified.

### 4. Performance

The field units and the laboratory unit have been in operation for several months. Some difficulties were initially present, but these were corrected. Since then, the test equipment has been functioning without any apparent problems.

## C. Digital Equipment, H. C. Wilck

### 1. Design Changes

Figure 2 shows a block diagram of the digital equipment. The 10-bit digital-to-analog (D/A) converter,

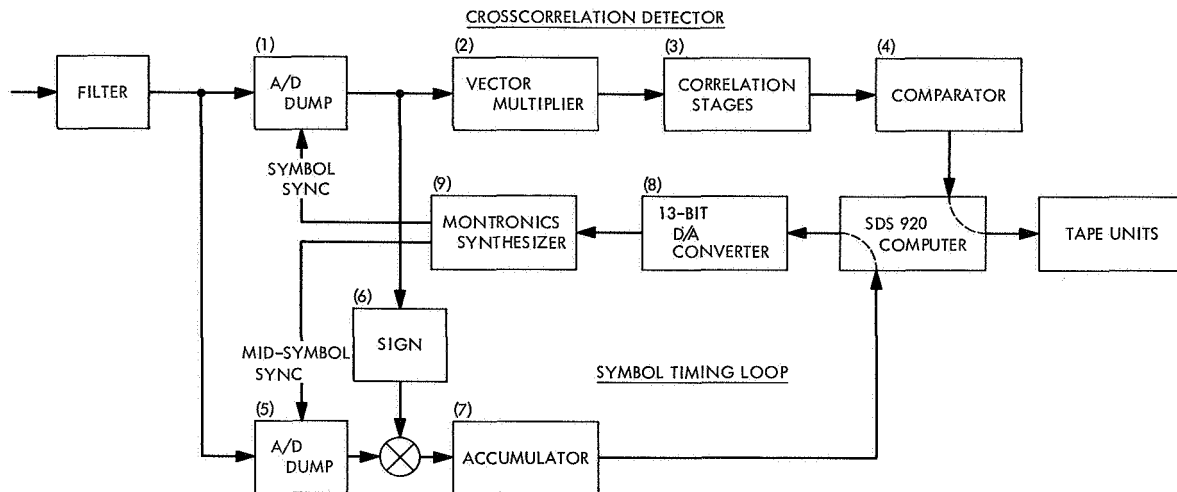


Fig. 2. Digital equipment diagram

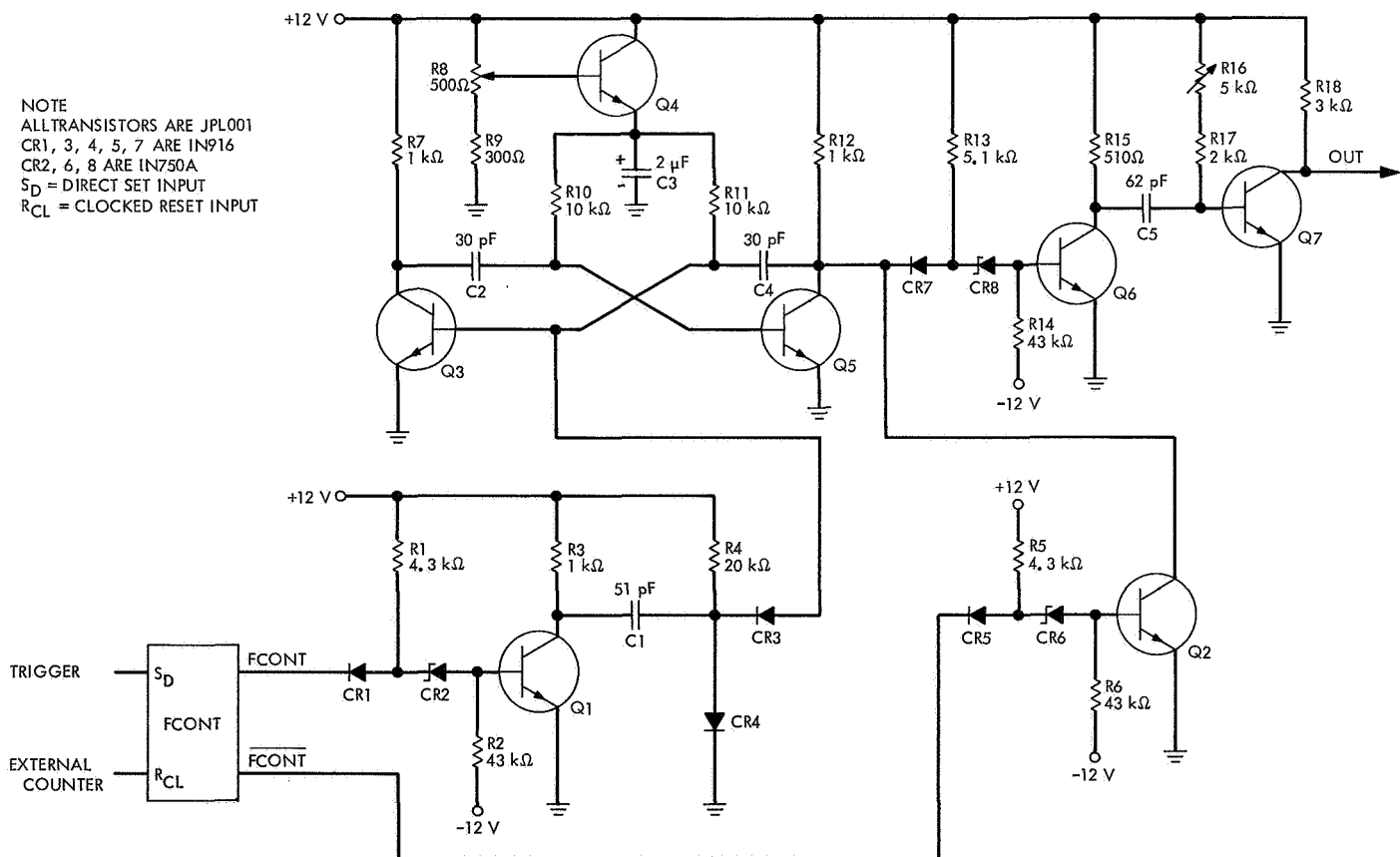


Fig. 3. Clock generator schematic

block (8) of Fig. 2, was changed to 13 bits. Also, the Hewlett-Packard frequency synthesizer, block (9) of Fig. 2, was replaced by a Montronics Model 314B-5; the Montronics synthesizer is capable of searching symmetrically around any frequency within its range, while the

Hewlett-Packard searches over full decades only. Both the D/A change and the synthesizer change improve the voltage-controlled oscillator resolution in the symbol loop, and this in turn allows the loop to operate at a narrower bandwidth.

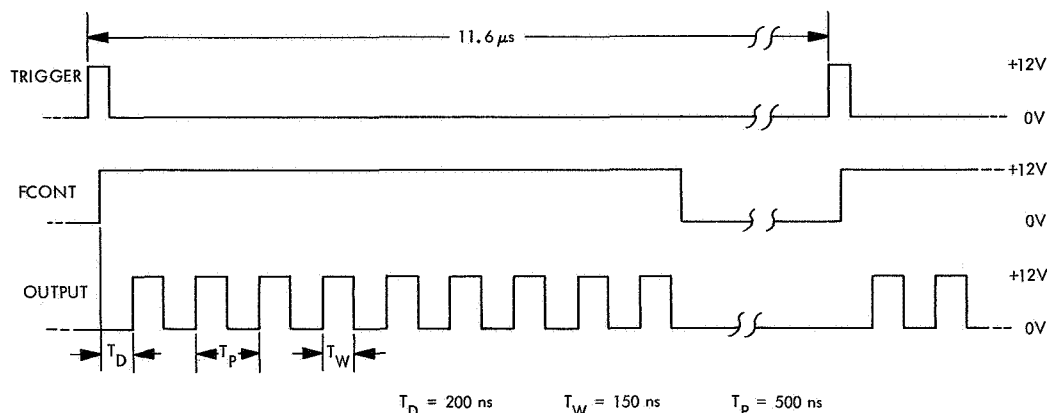


Fig. 4. Clock generator timing diagram

The system clock generator has been changed to a new design with more easily adjustable repetition rate and pulse width and improved independence of active component parameter variations. Figures 3 and 4 show the circuit and the timing diagram for the new clock generator. A trigger pulse, in synchronism with the incoming symbol frequency, sets control flip-flop FCONT, causing the generator to start outputting clock pulses after an initial delay  $T_D$ . After nine clock pulses, FCONT is reset by an external counter (not shown), thus terminating the clock sequence and making the generator ready to receive the next trigger. The value of C1 determines the delay  $T_D$ ; the repetition rate  $1/T_P$  and the pulse width  $T_W$  can be adjusted by means of R8 and R16, respectively.

## D. Software Teletype Output Routines,

P. H. Schottler

### 1. Introduction

One of the requirements on the HRT software package is that it provides real-time information concerning the status of the HRT system both to the local station and to the Space Flight Operations Facility (SFOF). This dual requirement is fulfilled by using one of the teletype channels which interfaces with the telemetry and command processor (TCP) communications buffer. The local output is provided by a teletypewriter located at the station, and the output to the SFOF is provided over the teletype link connecting the station with the SFOF. The teletype output, together with the data output on magnetic tape, comprises the permanent record of the HRT system. The software routines which provide for teletype channel output are briefly described in this article.

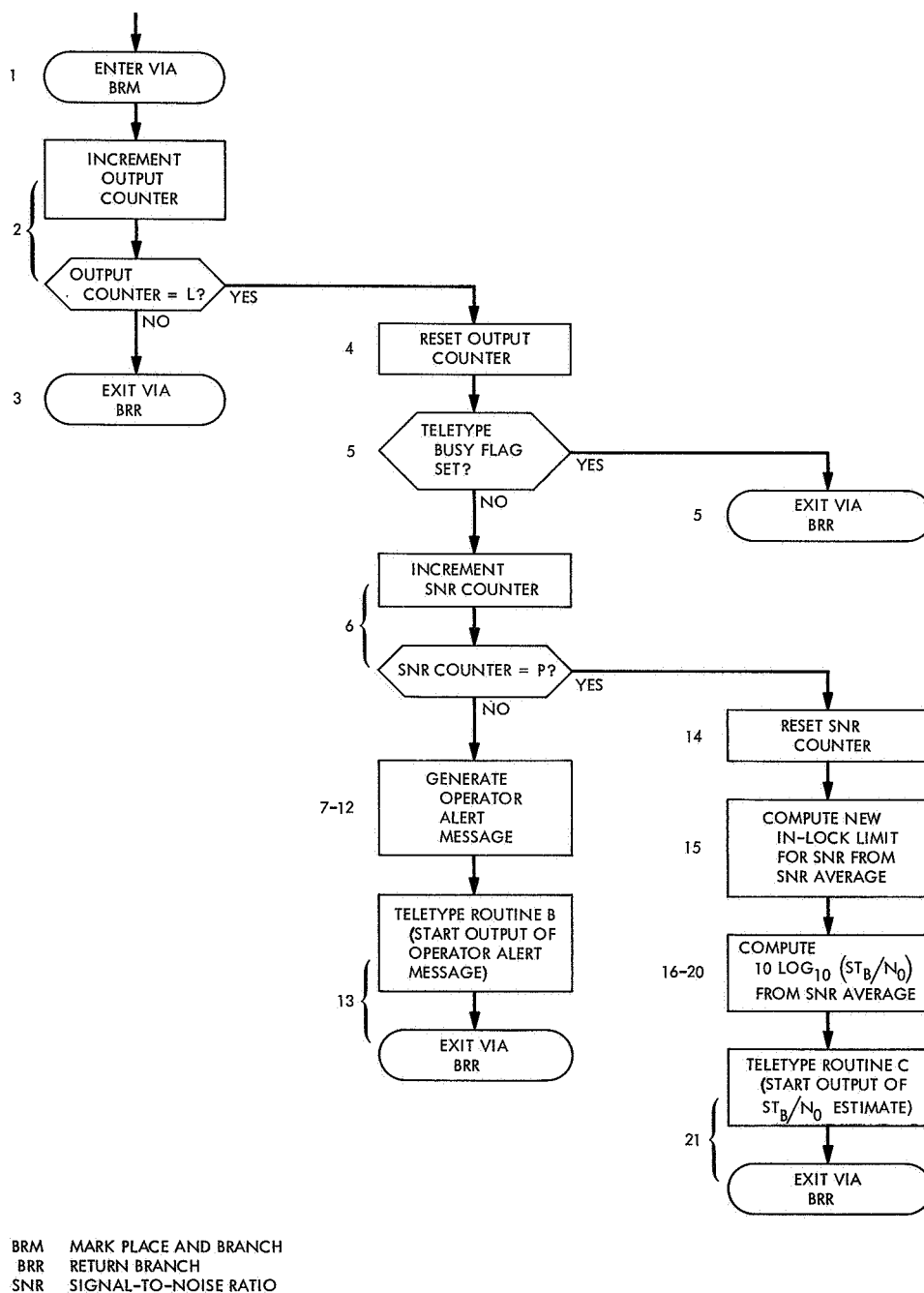
### 2. Teletype Output

The teletype output takes two different forms. One form consists of alert messages which provide information about the current status of various components of the HRT system. The alert messages are intended primarily for use by the TCP operator at the local station. Typical alert messages provide information about the current lock status of the carrier and subcarrier loops, about the readiness of the magnetic tape units for data recording, and about mode transitions which occur as a result of word loop loss-of-lock. The alert message output is coded in order to minimize the time required to output the alert. A message consists of a time tag followed by a three-digit number, the first digit of which specifies the mode that the program is in (0, 1, 2, or 3), and two digits which specify the message number. A table lookup provides the operator with the message content and specifies what action, if any, is required.

The second form of teletype output consists of an estimate of the ratio of signal energy per information bit to noise spectral density ( $ST_B/N_0$ ) in dB. This output provides a measure of the overall performance of the HRT system and is intended for use primarily by SFOF personnel to evaluate spacecraft performance. The estimate output consists of a time tag followed by a six-digit number (three places to either side of the decimal point and preceded by an algebraic sign) and is read directly in dB.

### 3. Teletype Routines

Five software routines participate in the output of teletype messages. They are teletype routines A, B, and C (TTRA, TTRB, and TTRC) shown in Figs. 5, 6, and 7, respectively, and teletype interrupt routines A and B (TIRA and TIRB) shown in Figs. 8a and 8b, respectively.



**Fig. 5. Teletype routine A (TTRA)**

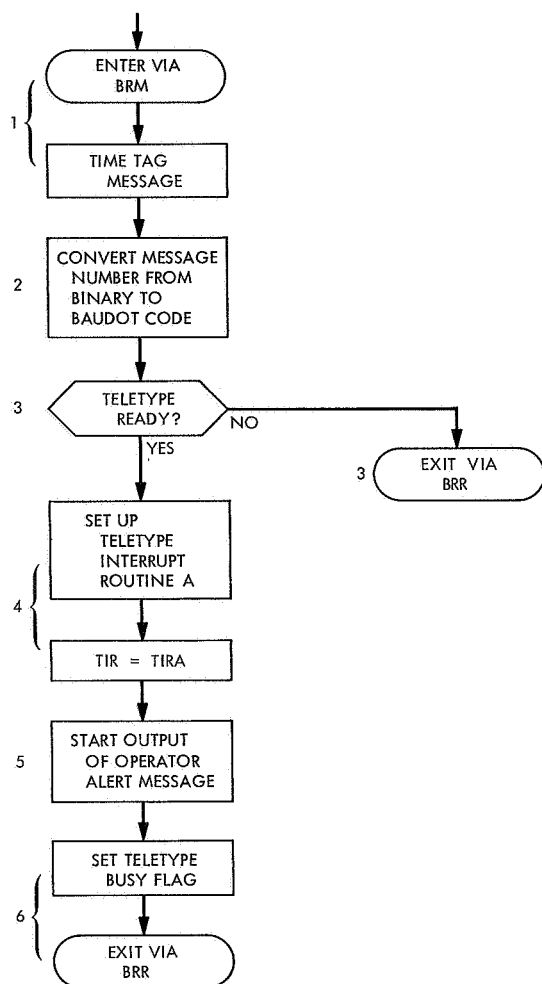


Fig. 6. Teletype routine B (TTRB)

Routine TTRA appears as block 33 of the data processing routine of mode 3 (SPS 37-48, Vol. II, p. 105, Fig. 16). Routines TTRA, TTRB, and TTRC are coded as sub-routines, and entry is by means of a "mark place and branch" instruction.

Routines TTRA, TTRB, and TIRA handle the output of operator alert messages. After every group of  $L$  data records ( $L = 20$ ) is written on magnetic tape, a status check of the various components of the HRT system is made in TTRA and the message number which corresponds to the current status of the system is generated. The program then enters routine TTRB where a time tag is added, the entire message converted from binary to five-level Baudot code, and the message output started. Control of the message output then passes to teletype interrupt routine TIRA. After each Baudot character is transmitted, a "teletype transmit end of word" interrupt occurs and the program enters routine TIRA where the

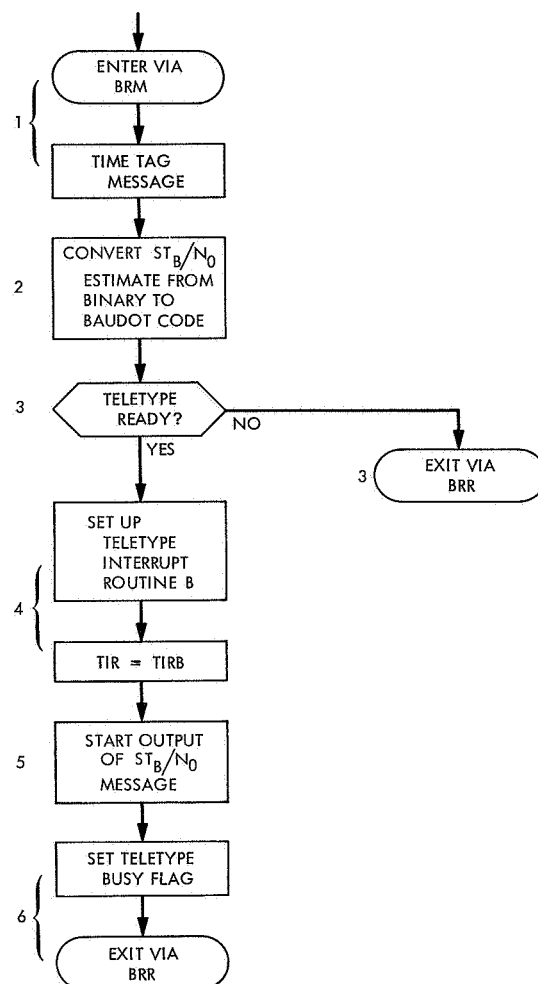


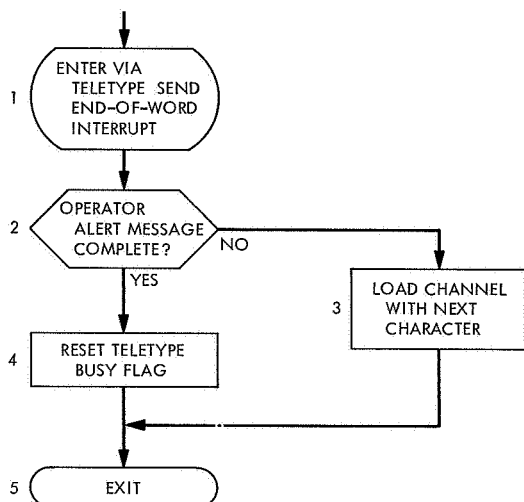
Fig. 7. Teletype routine C (TTRC)

next character is loaded into the channel. When the final character has been transmitted, the channel disconnects. During the time that the teletype channel is in the process of transmitting a message, the teletype busy flag is set. The flag is reset when the message output is complete. The program can test the teletype busy flag to determine when a new transmission can be started.

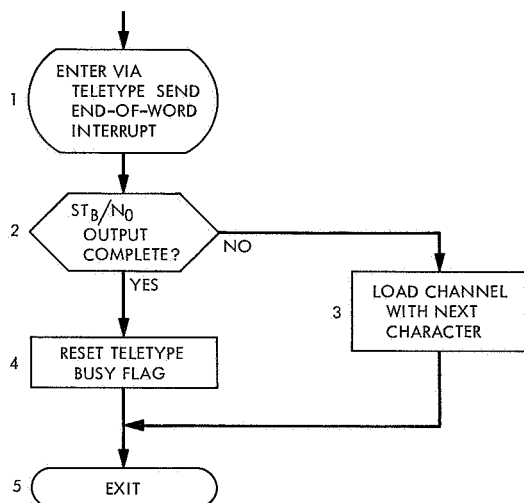
The "teletype transmit end of word" interrupt is a patchable 200-level interrupt in the TCP. Using a teletype channel rather than the TCP console typewriter to provide status information at the local station thus has the added advantage, as far as real-time operation is concerned, that the teletype channel is a low priority device whereas the console typewriter, which is on a noninterlaced buffer, is a high priority device (interrupt level 31).

Routines TTRA, TTRC, and TIRB handle the output of  $ST_B/N_0$  estimates. After every group of  $L \cdot P$  data

(a) TIRA



(b) TIRB



**Fig. 8. Teletype interrupt routine A (TIRA) and B (TIRB)**

records ( $P = 5$ ) is written on magnetic tape, the quantity  $10 \log_{10}(ST_B/N_0)$  is computed in TTRA. The value of  $ST_B/N_0$  used in this calculation is an average of  $ST_B/N_0$  over the immediately preceding 100 data records. This average is computed in block 14 of the data processing routine of mode 3 (SPS 37-48, Vol. II, p. 105, Fig. 16). After the quantity  $10 \log_{10}(ST_B/N_0)$  is computed in TTRA, the program enters routine TTRC where a time tag is added, the entire message is converted from binary to Baudot code, and the message output is started. Control of the message output then passes to teletype interrupt routine TIRB.

The  $\log_{10}$  calculation in TTRA makes use of straight-line approximations to the  $\log_2$  function over three intervals of abscissa, the result being then converted to  $\log_{10}$ . The straight-line approximations are obtained by minimization of the mean-square error

$$\bar{\epsilon}^2 = \int_a^b [\log_2 x - (ax + b)]^2 dx \quad 0.5 \leq a < b \leq 1.0$$

over each of the three intervals. The intervals are taken to be  $[0.5, 0.65]$ ,  $[0.65, 0.8]$ , and  $[0.8, 1.0]$ . The absolute error in the calculation of  $10 \log_{10}(ST_B/N_0)$  does not exceed  $8 \cdot 10^{-3}$ . The standard Scientific Data Systems programmed operator for  $\log x$  is not used because execution of the programmed operator takes too much time, and also because the algorithm contains a divide instruction which is non-interruptable for 28 memory cycles. A worst-case timing analysis of the program shows that this divide instruction could cause a data interrupt to be missed.

## E. System Verification Tests, R. W. Burt

During July 1968, a series of system tests was performed using field set 1 at the compatibility test area. The measurement techniques discussed in previous SPS articles were used to determine the performance measurement of word error rate of the demodulated telemetry as a function of the RF input signal-to-noise ratio ( $ST_B/N_0$ ).

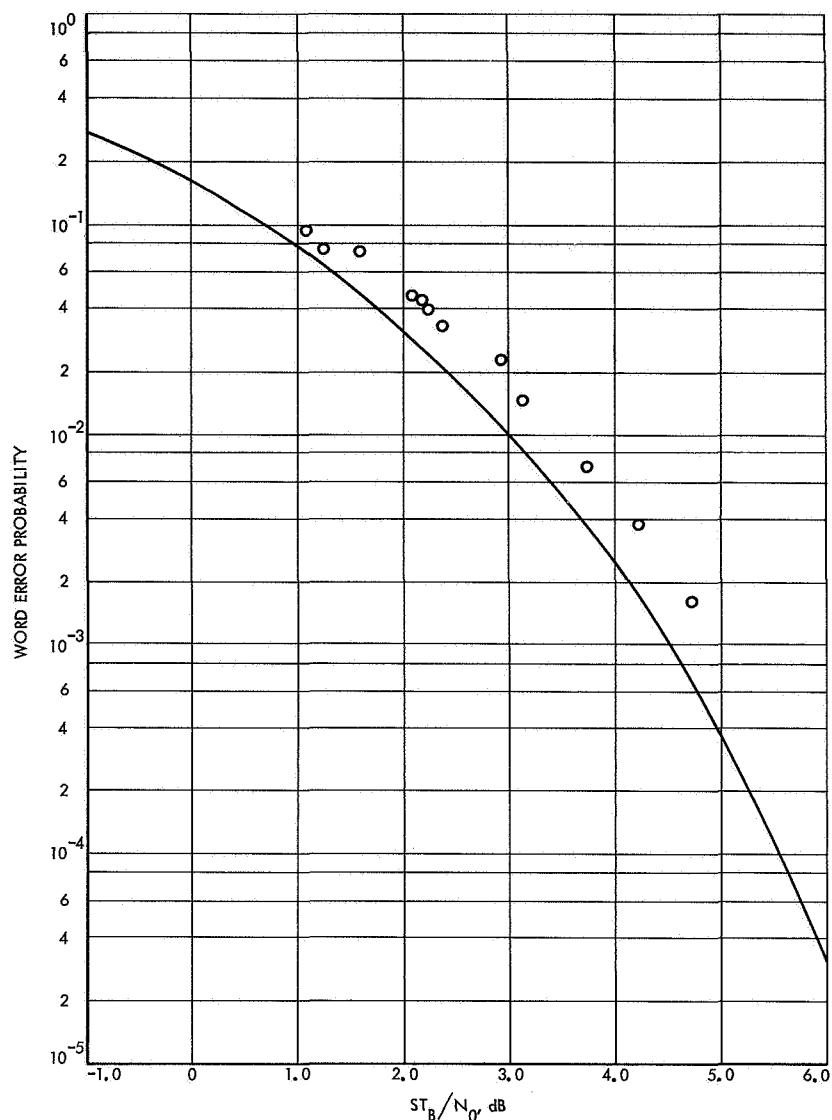
Results were compiled two or three points at a time on July 9, 11, 12, 17, 18 and 19. A composite of the test results is shown in Fig. 9. Average degradation for the data is 0.47 dB, a degradation slightly worse than the high-rate telemetry design goal of 0.44 dB. Note that performance consistency was demonstrated over a period of six different days.

## F. Effect of Variation in Subcarrier Loop Parameters on Telemetry Subcarrier Demodulator Performance, M. H. Brockman

### 1. Introduction

Theoretical performance characteristics for the telemetry subcarrier demodulator, which are applicable to a wide range of data rates for both uncoded and coded binary phase-shift-keyed telemetry, were presented in SPS 37-52, Vol. II, pp. 127-143. This article presents the effects of variation in the subcarrier tracking loop parameters on the basic performance characteristics of the telemetry subcarrier demodulator.

Fig. 9. High-rate telemetry test data



## 2. Subcarrier Tracking Loop Design and Telemetry Demodulator Performance

As developed in SPS 37-52, Vol. II, the performance of the telemetry subcarrier tracking loop is uniquely related to the signal-to-noise spectral density parameter  $(\alpha')^2 \times S/N_0$  in the tracking loop predetection filter  $F_{A_2}$  for any signal level, telemetry data rate, and coding scheme within the capabilities of the DSIF S-band system. The factor  $\alpha'$  represents the data suppression factor (SPS 37-46, Vol. III, pp. 189-204). The nominal noise bandwidth of the predetection filter  $F_{A_2}$  is 500 Hz, while the nominal design point parameters for the subcarrier tracking loop (which are contained in SPS 37-52, Vol. II) are presented in Table 1 for reference.

The following variations relative to the nominal (nom) design point parameters are applied herein to the theoretical expressions presented in SPS 37-52, Vol. II:

$$\frac{\alpha_{SL_0}}{\text{nom } \alpha_{SL_0}} = 0.91 \text{ to } 1.12$$

$$\frac{G_0}{\text{nom } G_0} = 0.70 \text{ to } 1.35$$

$$\frac{\tau_1}{\text{nom } \tau_1} \text{ and } \frac{\tau_2}{\text{nom } \tau_2} = 0.95 \text{ to } 1.05.$$

**Table 1. Subcarrier loop design point parameters**

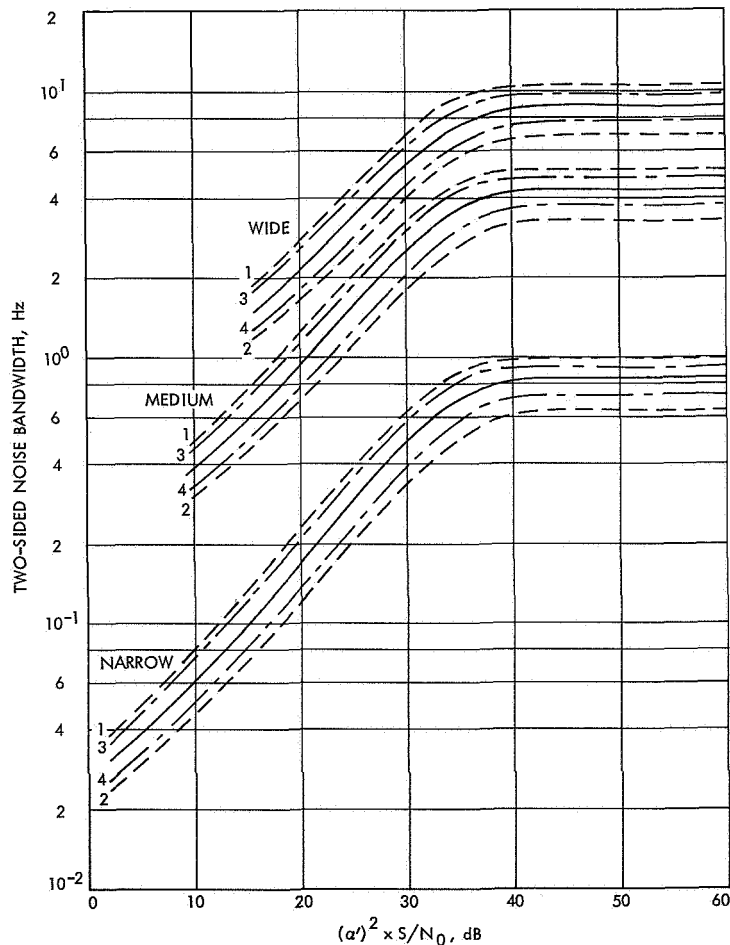
Design point noise bandwidth, Hz	$(\alpha')^2 \times S/N_0$ , dB	Soft bandpass limiter			$G_0$ , 1/s	$r_0'$ , ratio	$\tau_1$ , s	$\tau_2$ , s
		$\alpha_{RL_0}$ ratio	$\nu$ ratio	$\Gamma_{RL}$ ratio				
0.03	+1.7	0.0244	0.50	1.16	10	2.0	12,500	50
0.375	+9.7	0.0611	0.50	1.15	250	2.0	3000	4
1.50	+15.7	0.122	0.50	1.12	500	2.0	250	1

It should be pointed out that a variation in  $G_0$  from 0.70 to 1.35 of nominal accommodates the following tolerances:

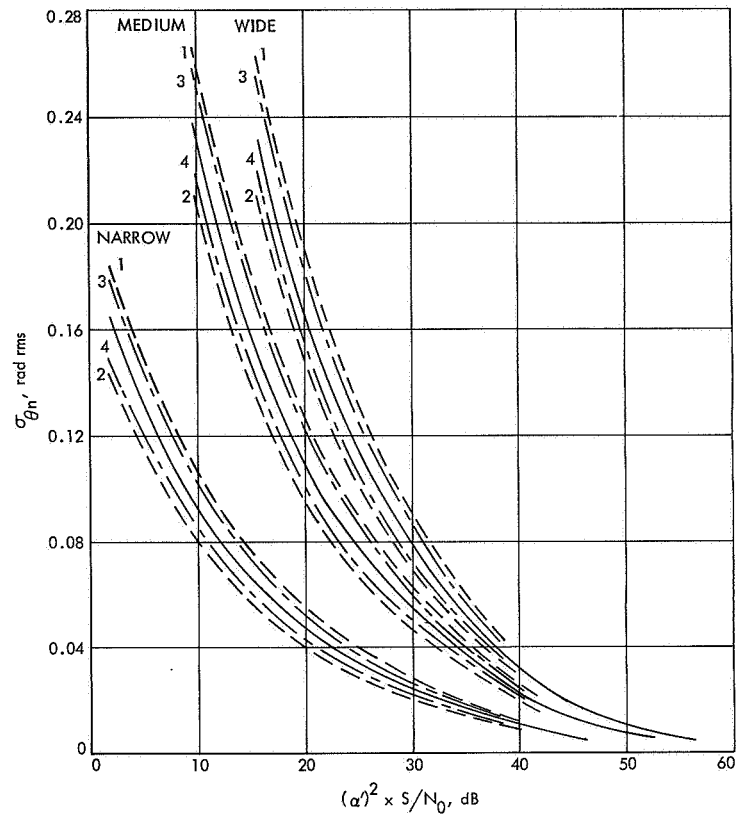
$F_{A_2}$ noise bandwidth	$500 \pm 100$ Hz
Detector slope	0.9 to 1.1 of nominal
Voltage-controlled oscillator sensitivity	0.9 to 1.1 of nominal

plus a change in phase shift through the filter  $F_{A_2}$  and the soft bandpass limiter of 15 deg from design point to strong signals.

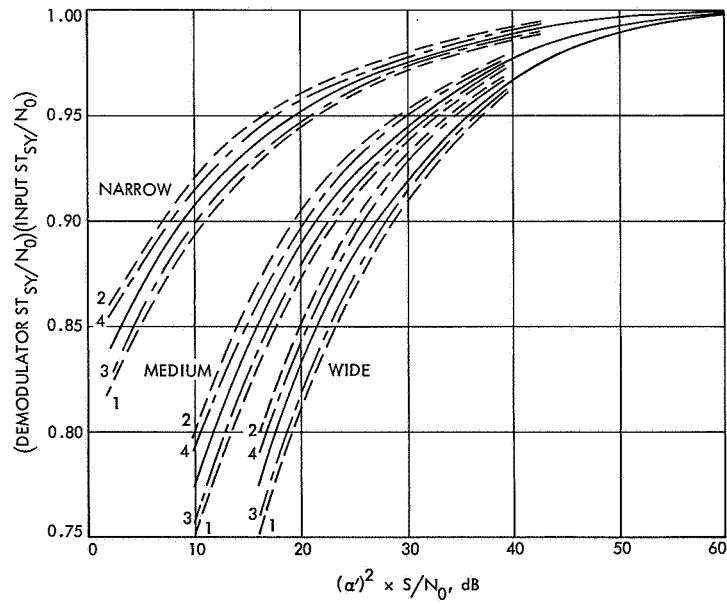
The effect of the variation in subcarrier loop design point parameters on two-sided closed-loop noise bandwidth  $BW_{SCL}$  is shown in Fig. 10 as a function of the signal-to-noise spectral density parameter  $(\alpha')^2 \times S/N_0$  from equipment design point to strong signal levels for



**Fig. 10. Telemetry subcarrier demodulator two-sided closed-loop noise bandwidth vs predetection signal-to-noise spectral density ratio parameter**



**Fig. 11. Telemetry subcarrier demodulator rms phase noise error vs predetection signal-to-noise spectral density ratio parameter**



**Fig. 12. Demodulated  $ST_{SV}/N_0$  vs telemetry demodulator predetection signal-to-noise spectral density ratio parameter (subcarrier loop noise bandwidth: narrow, medium, wide)**

the three bandwidths listed in Table 1. Following is the legend for Figs. 10-12.

————	Nominal
— — — — 1	$G_0 = 1.35$ nom, $\tau_1$ and $\tau_2 = 0.95$ nom
2	$G_0 = 0.70$ nom, $\tau_1$ and $\tau_2 = 1.05$ nom
— . — . — . 3	$G_0 = 1.25$ nom, $\tau_1$ and $\tau_2 = 0.95$ nom
4	$G_0 = 0.80$ nom, $\tau_1$ and $\tau_2 = 1.05$ nom

The resulting effect of design point parameter variation on the subcarrier tracking loop rms phase noise error  $\sigma_{\phi_n}$  is shown in Fig. 11 as a function of  $(\alpha')^2 \times S/N_0$  for the three bandwidth designs listed in Table 1. The  $\sigma_{\phi_n}$  characteristics in Fig. 11 are applicable to any probability of

data symbol stream switching and for any ratio of  $\tau_D/\tau_{SY}$  selected (SPS 37-52, Vol. II).

Finally, the effect of design point parameter variations on ratio of demodulated  $ST_{SY}/N_0$  to input  $ST_{SY}/N_0$  (demodulation efficiency) with zero phase error due to doppler frequency shift/rate is shown in Fig. 12 as a function of  $(\alpha')^2 \times S/N_0$  for the three bandwidth designs listed in Table 1. It is interesting to note the following: With variation of  $G_0$  from 0.70 to 1.35 of nominal plus variation of  $\tau_1$  and  $\tau_2$  from 1.05 to 0.95 of nominal, the resulting variation in demodulation efficiency at equipment design point is  $\pm 0.020$ ,  $\pm 0.025$ , and  $\pm 0.025$  for the three bandwidth designs (Fig. 12).

Use of the performance characteristics shown in Figs. 10 through 12 is presented in SPS 37-52, Vol. II by application to *Mariner Mars 1969*.

## VIII. DSIF Development and Operations

### A. Time-Synchronization System Performance,

H. W. Baugh

A precision clock-synchronization network is being established to meet DSN requirements. The immediate goal for this system is to synchronize all stations committed to *Mariner* Mars 1969 to within 20  $\mu$ s, and provide correlation to the National Bureau of Standards (NBS) to within 5  $\mu$ s for the DSN as a whole.

The system being used was described in SPS 37-43, Vol. III, pp. 92-106 and SPS 37-45, Vol. III, pp. 72-75. Some preliminary results of the field experiments were described in SPS 37-47, Vol. II, pp. 90-92, SPS 37-50, Vol. II, p. 165, and SPS 37-53, Vol. II, pp. 97-99.

Time-synchronization transmissions are continuing on a routine basis whenever the master station at Venus and Tidbinbilla DSS have a common view of the moon during their normal working periods. Schedules and predicts are normally sent to the receiving station several weeks in advance and followed up with a weekly teletype message giving the anticipated transmission schedule for the next week. Participation by the NBS has been hampered due to a lack of personnel to commit to the operation on a formal basis. Tidbinbilla DSS is performing time synchronization operations as a routine duty.

Early in August, Tidbinbilla DSS began experiencing a gradual degradation in receiver output and, by mid-month, the signals were unusable. Telephone conferences assisted the station in isolating the problem, which was caused by a malfunction of the digital coder due to an improper supply voltage. Correct adjustment of the supply voltage restored the system to normal operation. Note that the receiver at Tidbinbilla DSS is the earliest prototype unit, and that the modules used in the coder were fabricated several years ago. Further, there are some known deficiencies in the logic implementation. These problems will be corrected during the implementation of the rest of the time synchronization network, as discussed below.

The results obtained at Tidbinbilla DSS continue to be satisfactory; when any data is obtained, it is generally consistent. The rubidium standard in use has a history of nearly constant drift rates for long periods. This makes it possible to assess the stability of the time synchronization system by fitting a straight line to the data and observing the differences between observed points and the fitted line. Figure 1 shows such a plot for the data given in Table 1, which is the latest available performance record. The individual points are all within about  $\pm 6 \mu$ s of the straight line, and the distribution of the differences has a standard deviation of 3.25  $\mu$ s. Overall

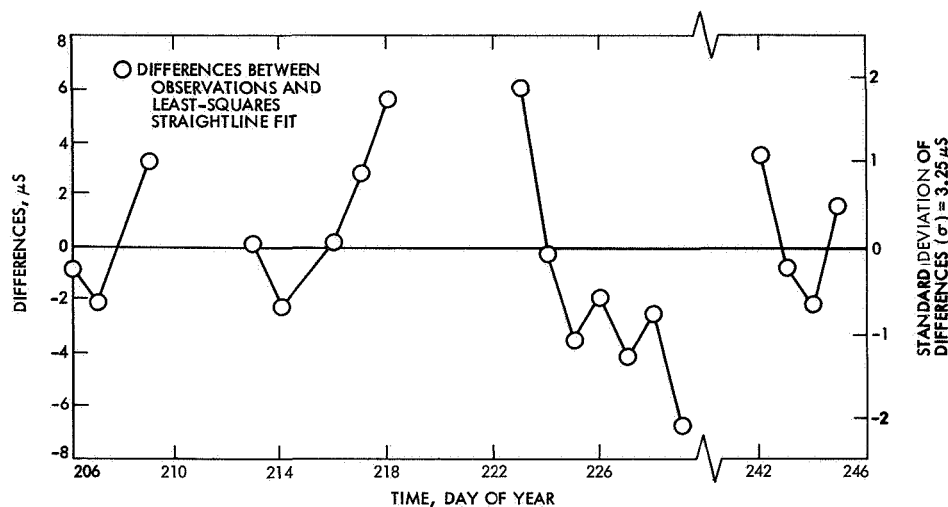


Fig. 1. Clock synchronization results from Tidbinbilla DSS

Table 1. Clock Synchronization results from Tidbinbilla DSS

Calendar date	Day of year	Measured offset (42-13), $\mu$ s	Differences <sup>a</sup> (measured-fitted), $\mu$ s
July 24	206	11	-0.77
25	207	15	-2.07
27	209	31	3.33
31	213	49	0.12
Aug. 1	214	52	-2.19
3	216	65	0.21
4	217	73	2.91
5	218	81	5.60
Note 1			
10	223	108	6.09
11	224	107	-0.21
12	225	109	-3.51
13	226	116	-1.82
14	227	119	-4.12
15	228	126	-2.42
16	229	127	-6.72
Notes 1 and 2			
29	242	207	+3.58
30	243	208	-0.72
31	244	212	-2.03
Sept. 1	245	221	+1.67

<sup>a</sup>Differences = measured offset - [11.76 + (date - 206)] in  $\mu$ s.

NOTES

1. Tidbinbilla DSS clock retarded 100  $\mu$ s. Offsets are given as though the clock were not retarded, to facilitate date reduction.
2. Prolonged gap in data due to receiver troubles. Clock jump at Tidbinbilla DSS forced the station to re-set its clock by reference to Mt. Stromlo.

system performance as a real-time operation may be somewhat better than these values indicate since the data has not yet been corrected for any drifts in the Venus DSS clock. In formal operations, the timing pulses to the

transmitter system will be verified before each transmission by comparison with the Goldstone Standards Laboratory, which is maintained as close as possible to NBS time.

During September and October, there were numerous interruptions in the service, largely due to transmitter upgrade and overhaul work and to problems of training personnel at Venus DSS as preparations are being made to convert the experimental system into an operational network.

The full network will be implemented early in 1969. New receivers are undergoing system tests in mid-October, antennas are ready for shipment, and new coders have been built. The four new receivers will be installed at Woomera, Tidbinbilla, Johannesburg, and Cebreros DSSs. The receiver at Tidbinbilla DSS will be completely refurbished for installation at the U.S. Naval Observatory, and the equipment at NBS/Boulder will be provided with some modifications and additions to improve its effectiveness.

The receiver-coders supplied thus far have been designed to work in conjunction with frequency and timing system (FTS) I, which provides timing pulses that swing between ground and a negative supply voltage. Since some of the new installations will be working with FTS II, their coders will be designed to accept the positive logic levels supplied by the new units. The installation kits for such stations will include coders of both types so that the checkout can proceed in advance of FTS II implementation.

## **B. Station Control and Data Equipment,**

*E. Bann, A. Burke, J. Woo, D. Hersey, and P. Harrison*

### **1. Introduction**

This article gives the status of the DSIF station control and data equipment (SCDE), as of October 1968. The SCDE consists of the antenna pointing subsystem, Phase I (APS-I), digital instrumentation subsystem (DIS), telemetry and command processor, Phase IIC (TCP-IIC), station monitor and control console, Phase II (SMCC-II), and the frequency and timing subsystem, Phase II (FTS-II). The DIS is not included in this report because of the present level of network implementation efforts.

### **2. Antenna Pointing Subsystem, Phase I**

The APS-I has been implemented in the deep space stations for the purpose of providing computer control of antenna pointing by means of manual inputs, precomputed drive tapes, or on-line ephemeris computations. A more detailed description of APS-I is given in SPS 37-38, Vol. III, pp. 74-76.

Installation of APS-I at Echo, Woomera, Tidbinbilla, Johannesburg, Robledo, and Cebreros DSSs is essentially complete with the equipment operational in all modes except the injection conditions mode. Current activity has been concerned with resolving hardware and software problems in the field. The APS-I software is being updated to include a "reasonable data" check of the drive tape in tape drive mode, a more compatible error/voltage slope for analog error outputs, an earlier warning for "out-of-limits" check of antenna position, and resolution of timing problems in the injection conditions mode.

The Scientific Data Systems (SDS) 910 computer in the Mars DSS APS has been retrofitted to the standard catalog SDS 910 configuration. This makes all APS-I systems identical with the exception of Tidbinbilla and Robledo DSSs, which will be retrofitted at a later date.

### **3. Telemetry and Command Processor, Phase IIC**

The TCP-IIC was updated to the Phase IIC configuration as part of the multiple mission telemetry system (MMTS). The extent of the updating is discussed in SPS 37-46, Vol. III, pp. 230-234.

The installation and checkout of the TCP-IIC equipment has been completed at Echo, Woomera, Johannesburg, Cebreros, Cape Kennedy, and Mars DSSs (one TCP-IIC computer) and compatibility test area (CTA) 21.

High-speed data modification kits for the TCP-IIC communications buffer, used to maintain interface compatibility with NASCOM error encoder-decoder equipment, have also been installed and checked out at these DSSs.

Mars DSS has been equipped with a single-computer TCP-IIC configuration. The station will remain in this configuration until March 1, 1969. Until this time, the other computer for Mars DSS will remain at the SFOF for software checkout.

The TCP-IIC equipment required to bring Tidbinbilla and Cebreros DSSs to the standard configuration is on order with delivery to JPL scheduled to begin in late December 1968. Installation and checkout of this equipment will be performed during January and February, 1969, at Tidbinbilla and Robledo DSSs, respectively.

### **4. Station Monitor and Control Console, Phase II**

The installation of the Program Alarm and Control Panel into the SMCC-II at Echo DSS was completed on September 6, 1968. Installation kits for performing this modification at four other stations were shipped during the week of September 22, 1968.

Six X-Y recorders have been procured and are currently being evaluated. These recorders will be installed in the SMCC-IIs to display doppler residuals, doppler noise, angle residuals, and received signal strength in either residual or unprocessed form. The X-Y recorder receives analog input signals and control signals from the Phase II DIS. It features several modes of operation that allow it to be used as either a conventional X-Y recorder or a fully computer-controlled plotter. Graphs may be made on either roll charts or individual sheets using a ball point pen or a character printer.

The first installation of the plotter will be made at Echo DSS during the early part of November 1968. Assuming that no serious problems are encountered, the five remaining recorders should be delivered to the stations sometime in December 1968.

### **5. Frequency and Timing Subsystem, Phase II**

The FTS-II equipments, which were to be assembled by a contractor, have been received and are being added to, and tested, at JPL. The additions and modifications will be completed, and all units shipped and installed, prior to the end of the year. The first of these units will

be installed at Mars DSS during the period October 10–November 11, 1968.

### C. Rapid Generation of Monitor Criteria Data,

M. Thomas

Future mission requirements have created a need for the rapid generation of monitor criteria data (MCD) to support the DSIF monitor program. *Mariner* Mars 1969 is the first mission that will require this capability. As discussed in SPS 37-50, Vol. II, pp. 181–185 and SPS 37-52, Vol. II, pp. 112–114, MCD has been generated in sets of approximately 269 parameters per set to be used in the establishing and monitoring of configuration, status, nominal values, and tolerance parameters for the DSIF subsystems. One highly desirable feature of rapid MCD generation is the minimization of time lag between station hardware changes and subsequent station software changes. Another desirable feature is the savings in time and work it will afford the operations group associated with the SFOF. The computer program will be initialized to the mission-independent set (standard set), which the operations engineer will review and make the changes he desires to the subsets. Notations of the changes will then be inputted (by keyboard) to the basic mission-independent set. Upon completion, the computer will integrate these changes into the mission-independent set and retain all other parameters to which the computer program has been initialized. This set will then be put into the MCD format and made ready for transmission to the station.

The basic approach is to take a mission-independent set of MCD and number the parameters sequentially (1 through 552). A mission-independent set of MCD, containing all possible combinations of subsystem parameters, includes at least  $51.32 \times 10^{157}$  sets. However, for *Mariner* Mars 1969 purposes, only 1396 of these will be used. The operations personnel will simply use a mission-independent set of MCD in which each subsystem parameter has been placed into a one-to-one correspondence with the sequential set of numbers. The operations engineer will indicate each parameter in the mission-independent set that is desired for a given mission mode. A software program will take these inputs and generate an MCD set for transmission to the station.

In developing this article, it was assumed that the only changes required were those associated with the subset corresponding to the microwave subsystem. This was borne out by a review of the microwave subset (Table 2) which revealed that only the subset of the parameters

Table 2. Microwave configuration subset

Sequential number	Parameter	Condition	Format
1	SCM <sup>a</sup> polarization	RCP <sup>b</sup>	000
2	SCM polarization	LCP <sup>c</sup>	111
3	SAA <sup>d</sup> polarization	RCP	000
4	SAA polarization	LCP	111
5	Transmitter antenna selector	SCM	0
6	Transmitter antenna selector	SAA	1
7	Transmitter load selector	Antenna	0
8	Transmitter load selector	RF water load	1
9	SAA sum channel selector	Paramp	0
10	SAA sum channel selector	Bypass	1
11	SCM sum channel selector	Maser	0
12	SCM sum channel selector	Bypass	1
13	Reference temperature load selector	Cryogenic	0
14	Reference temperature load selector	Ambient	1
15	Receiver 1 input selector	Maser	0
16	Receiver 1 input selector	Paramp	1
17	Receiver 1–10 dB attenuator	In	0
18	Receiver 1–10 dB attenuator	Out	1
19	Receiver 1–15–27 dB attenuator	In	0
20	Receiver 1–15–27 dB attenuator	Out	1
21	Receiver 1 bypass selector	Normal	0
22	Receiver 1 bypass selector	Bypass	1
23	Receiver 2 input selector	Maser	0
24	Receiver 2 input selector	Paramp	1
25	Receiver 2–10 dB attenuator	In	0
26	Receiver 2–10 dB attenuator	Out	1
27	Receiver 2–15–27 dB attenuator	In	0
28	Receiver 2–15–27 dB attenuator	Out	1
29	Receiver bypass selector	Normal	0
30	Receiver bypass selector	Bypass	1

<sup>a</sup>S-band cassegrain monopulse cone.  
<sup>b</sup>Right circular polarized.  
<sup>c</sup>Left circular polarized.  
<sup>d</sup>Station acquisition aid.

associated with the sequential numbers 1, 4, 6, 8, 10, 12, 14, 16, 18, 20, 22, 24, 26, 28 and 30 required changes. At this point, the required computer inputs are made based upon the sequential number and the corresponding format associated therewith. The computer input would appear as follows:

MCD (1/000, 4/111, 6/1, 8/1, 10/1, 12/1, 14/1, 16/1, 18/1, 20/1, 22/1, 24/1, 26/1, 28/1, 30/1) \$

This input establishes the desired microwave configuration and replaces the configuration to which the computer was initialized for the microwave subsystem. The computer will now integrate the new configuration with the initialized MCD set, and a new MCD set is generated and ready for transmission.

## D. DIS Monitor Calibration Computer Program,<sup>1</sup>

W. Roach and T. Lewis

### 1. Introduction

With the installation of the digital instrumentation subsystem (DIS) phase II computer hardware and the monitor program system, a revised calibration program became necessary. Previous calibration methods consisted only of an automatic gain control (AGC) curve fit for calibrating the different configurations of the receivers. The data from the AGC was then fitted to a polynomial and the coefficients input to the interim monitor program. The new method will interface with the DIS monitor program with calibrated data of the following four basic parameters:

- (1) Receiver and total system noise temperature, °K.

<sup>1</sup>For detailed information concerning this subject, see Request for Programming DSIF Phase I Monitor Calibration Program, Mar. 21, 1968 (JPL internal document) and DIS Monitor Calibration Computer Program (DOI-5010) by W. Roach and T. Lewis, Nov. 1968 (JPL internal document).

- (2) AGC voltage, dBmW.

- (3) RF error channel voltage, degrees.

- (4) Receiver static phase error (SPE) alpha suppression factors.

The interface between station equipment and the computer programs is shown in Fig. 2.

### 2. Functional Description

The AGC voltage and RF error channel voltages are brought into the DIS computer via the analog-to-digital converter. The four basic parameters listed in *Subsection 1* are calibrated and the data is placed on a magpak for utilization during track for real time monitoring of the parameters. The remainder of this subsection contains a discussion of the four parameters listed in *Subsection 1*.

*a. Receiver and total system noise temperature.* The Y-factor method is used in measuring the receiver and total system noise temperatures. Figure 3 is a block diagram of the calibration system. The temperatures of the

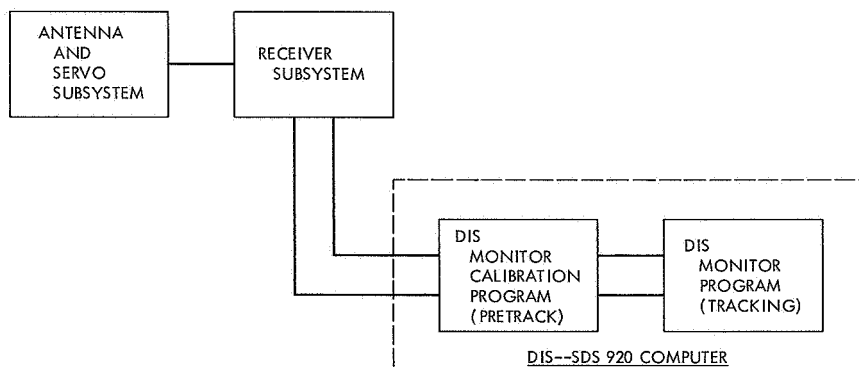


Fig. 2. Station equipment and computer program interfaces

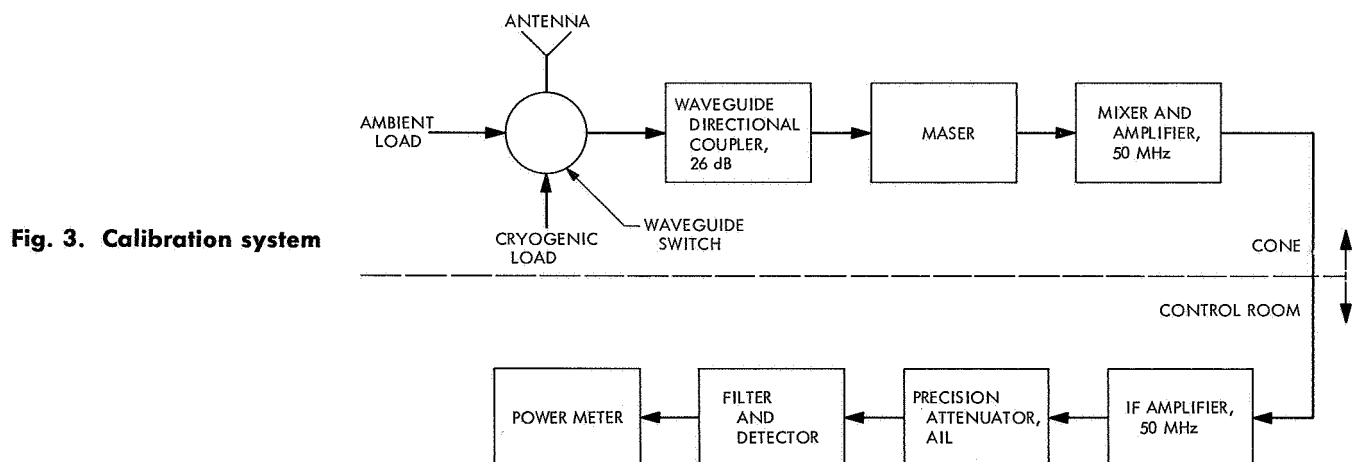


Fig. 3. Calibration system

ambient and cryogenic loads are measured and input to the program. The waveguide switch is switched between the ambient and cryogenic loads. The precision IF attenuator is adjusted each time for a common reference of system noise power  $P_n$ . The attenuator readings are then input to the program, which computes receiver noise temperature  $T_r$  (in °K) as follows:

$$y = P_{n(\text{amb})} - P_{n(\text{cryo})}$$

$$T_r = T_{(\text{amb})}^{\circ} - \frac{y - T_{(\text{cryo})}^{\circ}}{y - 1}$$

The procedure is repeated, switching the receiver between the ambient load and the antenna, and the attenuator readings input to the program for total system noise temperature computation. Both the receiver and total system noise temperatures are included in the printout from the line printer.

**b. AGC voltage.** The AGC is calibrated in much the same manner as described in *Paragraph a*. The test transmitter is adjusted for desired input signal levels into the 26 dB directional coupler shown in Fig. 3. The program samples the AGC voltage of both receivers. The voltages and input signal levels are stored so that, when all signal levels have been input, the program will fit the data to a fourth-order polynomial by a standard least-squares method. The coefficients are written on the magpak in order to be utilized by the DIS monitor program.

**c. RF error channel voltage.** RF error channel voltages are calibrated by first switching the receiver to the antenna and pointing the antenna at the collimation tower. The transponder is then turned on and the receiver locked to the signal. The antenna is moved to 0.1 deg off the signal in hour angle and samples the voltage from the error channel of the receiver. The antenna is then moved to an error of -0.1 deg and the voltage again sampled. The program fits these data to a straight-line equation and the coefficients are written on the magpak. This procedure is repeated for the declination angle.

**d. SPE alpha suppression factors.** A table of SPE alpha suppression factors is calculated for a fixed set of signal levels. The table is calculated using the total system noise temperature computed in *Paragraph c*. The table is then written on the magpak. This table will be used for the SPE voltage-to-degrees conversion.

### 3. Program Design

The DIS monitor calibration program is designed to operate on the DIS with phase II computer hardware. This consists of a Scientific Data Systems (SDS) 920 computer with a 16,000 word memory, W- and Y-buffers (interlaced), photoreader, paperpunch, plotter, typewriter, page printer, dual channel magpak, and two magnetic tape units. The program is written in the SDS Fortran II language, except for a few subroutines written in the SDS symbolic language. Analog-to-digital program inputs will come from the following three sources:

- (1) Console typewriter for operator inputs.
- (2) Analog-to-digital converter for analog inputs.
- (3) Photoreader for a data tape from a previous program run.

Program output will be on the following three media:

- (1) Paper tape for updating procedures at the station.
- (2) Line printer output for station analysis.
- (3) Magpak for utilization by the DIS monitor program.

Two guidelines were used in designing this program:

- (1) Ease of operation. Each input entry is preceded by a message from the typewriter that describes to the operator exactly which parameter is to be entered at that point.
- (2) Flexibility in use. Four different countdown procedures are available in the program to meet the pretrack requirements of the user at the tracking station.

The four countdown procedures are described in the remainder of this subsection.

**a. Initial class A.** No previous data tape is read. All desired configurations are computed from input data. When all tracking configurations have been input and computed, the program will punch out a data tape for future station reference and use.

**b. Class A.** This procedure is essentially the same as initial class A, except that a previous data tape is read in and only selected configurations are changed and computed.

**c. Class B.** This procedure is used as a "quick change" method for computing the correction factor for the AGC coefficients prior to tracking. The previous tape is read in and only a few data readings, preferably three to five points per curve, are input to compute the correction factor.

**d. Class C.** This procedure is merely a "load and go" method. No computations are made. The tape from a previous countdown is read in and the information is copied onto the magpak for immediate use by the DIS monitor program.

#### 4. Problem Formulation

The first input requested by the program is the desired countdown procedure. The program will then request the configuration number. Major configurations are maser, paramp and bypass for receivers I and II. Minor configurations are comprised of four possible bandwidths in the tracking loop of the receiver. Receiver I configurations are numbered 11 through 19; receiver II configurations are numbered 21 through 29.

The receiver and total system noise temperatures must be computed for each major configuration calibrated. The first two variables input to the program are the temperatures of the ambient load and the cryogenic load.

$T_{(amb)}$  = temperature of ambient load, °C (converted to °K in the program)

$T_{(cryo)}$  = temperature of cryogenic load, °K

**a. Receiver temperature.** The receiver is switched between the ambient load and the cryogenic load. For each load, a reference level is set by the precision IF attenuator referenced in Fig. 3. Three sets of readings are input to the program. The program will then compute the following:

$$Y = \frac{1}{3} \sum_{i=1}^3 [P_{n(amb)} - P_{n(cryo)}]_i$$

$$T_r = T_{(amb)} - \frac{Y - T_{(cryo)}}{Y - 1}$$

**b. System noise temperature.** The procedure is then repeated by switching the receiver between the ambient load and the antenna. Five sets of attenuator readings are

input to the program. The program computes the following:

$$Y = \frac{1}{5} \sum_{i=1}^5 [P_{n(amb)} - P_{n(ant)}]_i$$

$$T_s = \frac{T_{amb} + T_r}{Y_{ratio}}$$

where  $T_s$  is equal to the total system noise temperature.

**c. AGC coefficients.** The program then requests inputs for the calibration of the AGC curve. The signal power level for each point is input from the typewriter and stored in the array  $Y$ . One thousand samples are taken of a receiver AGC voltage and temporarily stored. The mean and standard deviation of these voltages are computed and a  $3.5\text{-}\sigma$  test is made on each of the 1000 points. All voltages falling outside this  $3.5\text{-}\sigma$  range will be resampled and a new mean and standard deviation computed. To insure further accuracy, this final standard deviation will be compared with a reference value stored in the program. If this computed standard deviation is greater than the reference value, another 1000 samples will be taken and the  $3.5\text{-}\sigma$  test procedures repeated. This resampling procedure will be allowed a maximum of five times. If the standard deviation does not meet the requirements after the five cycles, an error message will be typed out instructing the operator to check the configuration and the program will halt.

The last value of the signal power level should be 4 dB above threshold for the specific configuration being computed. The signal power level values (dependent variable) and the AGC voltages (independent variable) are used by a subroutine that will solve for the coefficients of a fourth order polynomial by a standard least-squares method. Another subroutine will compute fitted signal power levels  $Y'$  from the curve and difference these values with the input  $Y$ s.

$$X_i = \frac{1}{1000} \sum_{j=1}^{1000} V_j$$

$$\sigma_i = \left[ \frac{1}{1000} \sum_{j=1}^{1000} (V_j^2 - X_i^2) \right]^{1/2}$$

where

$V_j$  = voltage sampled

$X_i$  = mean voltage for a given power level of the signal

$\sigma_i$  = standard deviation

After all points for the curve have been taken, the program will compute the coefficients for the AGC polynomial:

$$Y'_i = A_0 + A_1X_i + A_2X_i^2 + A_3X_i^3$$

Each  $Y'_i$ ,  $Y_i$ ,  $X_i$ , and  $\sigma_i$  is printed out.

Each day that a calibration is performed, the punched tape from the last calibration is input to the program. During class B countdown, an AGC curve may be updated by inputting three to five points on the linear portion of the AGC curve. Voltages are sampled as before and the same  $3.5\sigma$  test is given. Using the mean voltage  $X_i$ ,  $Y'_i$  is then calculated for the three points of the polynomial from the punched tape. The correction factor is computed as follows:

$$A_0 = A_o + \frac{1}{3} \sum_{i=1}^3 (Y'_i - Y_i)$$

where  $A_0$  is equal to the first term of the polynomial.

**d. SPE tables.** The SPE alpha tables will be computed for each station configuration of maser, paramp, and direct. These computations will produce tables of alpha suppression factors, which are functions of the system noise temperature and signal power level values.

$$\alpha = \left[ \frac{0.785 \rho_H + 0.4768 \rho_H^2}{1 + 1.024 \rho_H + 0.4768 \rho_H^2} \right]^{1/2}$$

$$\rho_H = 10 \{ P_{s(\text{dBmW})} [-165.2 + 10 \log_{10}(T_s)] \} .1$$

Where  $P_s$  is equal to the received signal strengths (in dBmW). The tables to be output will be dBmW values versus  $\alpha$  factors for three configurations.

**e. RF error channels.** The RF error channel voltages are calibrated by locking the antenna in declination and introducing a  $\pm 0.1$ -deg error in hour angle. At each point, the voltage is sampled 1000 times and averaged. The error and mean voltage at each point are used to compute the coefficients for a linear curve. The antenna is

then locked in hour angle and the above procedure repeated for declination.

$$X_i = \frac{1}{1000} \sum_{j=1}^{1000} V_j$$

$$Y' = A_0 + A_1X_i$$

$$X_i = \text{mean voltage}$$

## E. Fiber Optics Boresight Telescope,

C. Lundy and F. Stoller

Hand-steered, 4-ft-diam tracking antennas are used at the Cape Kennedy Spacecraft Compatibility Station to track spacecraft during launch. With these antennas, it is essential that the operator have a visual (boresight) reference for tracking the target. Until recently this visual reference was provided by a rifle telescope that protruded through a small hole in the dish of the antenna (Fig. 4). When tracking a fast-rising spacecraft, the operator had to bend and twist in awkward attitudes, making it difficult to steer the antenna effectively.

The boresighting hardware has been upgraded as part of a redesign of the antenna mount used at Cape Kennedy.



Fig. 4. Antenna with rifle scope

The new design places the eyepiece of the telescope in a convenient place, which remains at a fixed angle of elevation. The new boresight device consists of a fiber optics bundle with objective and eyepiece. The fiber optics unit, purchased from Bausch and Lomb, is 18-in. long and contains a  $\frac{1}{8}$ -in. diam bundle of about 50,000 small glass fibers. These close-packed fibers are free for most of their length, but are bonded together solidly at both ends. The fiber bundle is protected and supported by a sealed flexible conduit having a maximum diameter of about  $\frac{1}{2}$  in. Although it has not been verified, the entire package appears to be sealed airtight; it will, in any case, be easy to make the finished telescope a sealed unit. The completed unit is shown in Fig. 5.

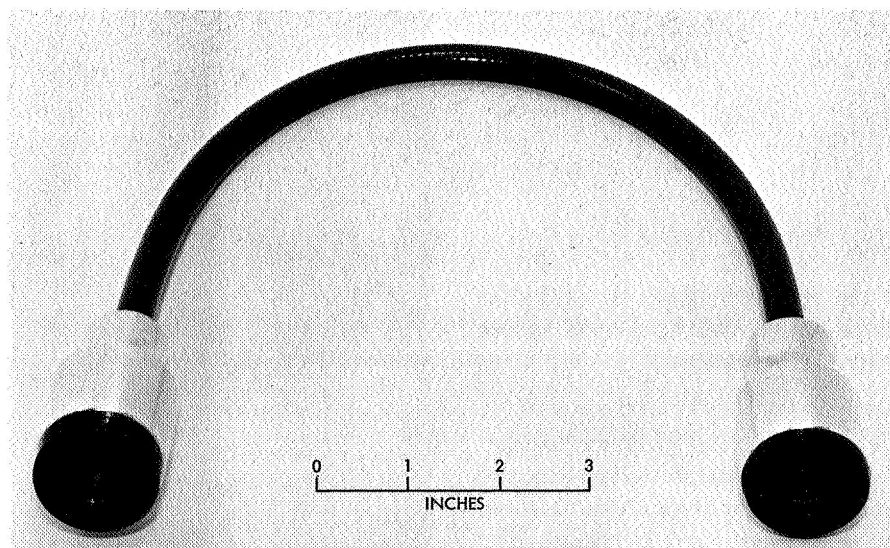
The fibers are so aligned at the ends that a real image formed on one end is transmitted to the other end with no change except in brightness. The change in brightness is due to the light lost by reflection and absorption, as well as the loss of oblique light, which the fibers do not accept. To measure the acceptance angle of the sample, a photoresistive cell was attached to the exit port with the input side clamped to a dividing head in such a way that the light from a small source could be received at varying angles. The manufacturer of the photocell states that the conductivity of the cell is proportional to the light flux. Data taken are plotted in Fig. 6. Approximately 96% of the light is included in the 40-deg span marked. Therefore, there is no advantage in using a "fast" objective for the telescope since light arriving at angles exceeding 20 deg is wasted.

The brightness of the image was compared with that of a  $6 \times 30$  monocular. A Gamma T-500 Telephotometer was used to measure the image brightness with both instruments facing a wide white screen. A mask with a small pupil at the eye point was used to avoid errors caused by different exit pupil sizes. The image from the flexible telescope was 0.36 as bright as that from the monocular. This reduction in brightness is not significant as the target is a bright light against the sky; i.e., the glow of the launch vehicle's rocket flame.

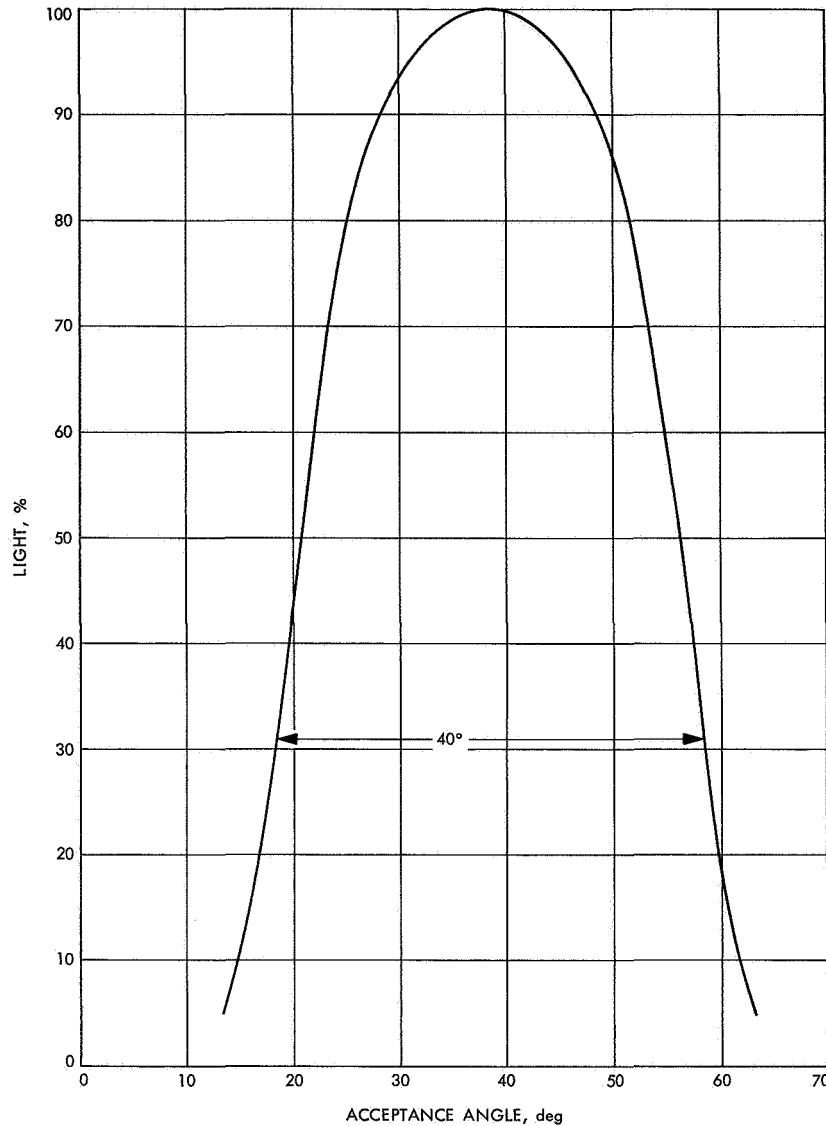
The entrance pupil of the system is set by the  $\frac{1}{8}$ -in. diam of the bundle. From other tests, it was decided that the field of view should have a total width of about 8 deg; this requirement had the effect of setting the focal length to about 1 in. The choice for the objective was a stock telescope eyepiece of 24-mm nominal focal length. Since a small magnification of the image at the eyepiece end proved optimum, a 16-mm eyepiece was used giving the user a 12-deg apparent field of view.

When a lens forms a real image, the image is inverted. In many optical instruments, there are either additional lenses to re-invert the image, or the light is folded by a pair of prisms. In this instrument, the inversion is accomplished by a 180-deg twist in the fiber optics package.

No focussing of either lens is provided. For the 24-mm objective, anything from a few feet away is in satisfactory focus. The eyepiece is fixed to match a normal relaxed eye so that the assembly can be sealed.



**Fig. 5. Completed fiber optics boresight hardware**



**Fig. 6. Light acceptance of fiber optics channel**

## F. Theoretical Phase Characteristics of Klystron Amplifiers, R. L. Leu

Optimum klystron amplifier performance is obtained when the klystron is operated in saturation at the rated power level and beam voltage. The klystron amplifier is required to operate at a reduced power level during earth orbits, the initial part of a tracking assignment, and for special tests with the spacecraft. The existing transmitter configuration allows only two methods for operation at reduced power levels: (1) beam voltage held constant and reduced RF drive (klystron not in saturation), or (2) reduced beam voltage and RF drive adjusted for the required power level. (Reducing the beam voltage does

not mean that the klystron is operated in saturation at reduced power.)

Operation at reduced beam voltage has a significant effect on the phase characteristics of the klystron amplifier. The phase characteristics are dependent on the electron velocity and the physical length of the klystron from input cavity to output cavity.

It can be shown (Ref. 1) that

$$\frac{\Delta\theta}{\theta} = \frac{1}{2} \frac{\Delta V}{V} \quad (1)$$

where

$\theta$  = electrical length of the klystron in radians

$\Delta\theta$  = variation in electrical length (change of RF phase)

$V$  = dc beam voltage

$\Delta V$  = small variations of beam voltage (less than 200 V)

and the phase pushing factor (PPF) is defined as

$$\text{PPF} = \frac{\Delta\theta}{\Delta V} = \frac{1}{2} \frac{\theta}{V} \quad (2)$$

The transient time of the electrons from input cavity to output cavity is  $T = L/e_v$ , where  $L$  = physical length, and  $e_v$  = electron velocity. If the electrical length of the klystron in cycles is  $fT = fL/e_v$ , where  $f$  is equal to RF frequency in radians, then

$$\theta = 2\pi fT = 2\pi fL/e_v \quad (3)$$

Relativistic corrections are required to compute electron velocity at each beam voltage. The electron velocity is defined (Ref. 2) as

$$e_v = c \frac{2e_c V_1}{2e_c V_1 + m_0 c^2} \quad (4)$$

where

$$V_1 = V + \frac{e_c}{2m_0 c^2} V^2$$

$e_c$  = electron charge

$m_0$  = rest mass of the electron

A computer program was written to compute the PPF and phase length (Eqs. 2 and 3) of a klystron amplifier as functions of beam voltage. Data were compiled for the 10 kW (5KM50SI), 20 kW (5K70SG), 100 kW (5KM300SI), and 400 kW (X3070) klystrons. A summary of the data is recorded in Tables 3-6.

Incidental phase modulation (IPM) is

$$\text{IPM} = \text{PPF} \Delta V \quad (5)$$

The IPM may be expressed in either deg p-p or deg rms depending on the unit of measure of the ripple voltage. This equation is valid either for determination of the total ripple content, or specific frequencies.

Table 3. Klystron 5KM50SI: 10 kW at 18 kV

Beam voltage, kV	Frequency			
	2.110 GHz		2.120 GHz	
	Phase length, rad	PPF, deg/V	Phase length, rad	PPF, deg/V
1	134.61	3.8563	135.25	3.8746
2	95.32	1.3654	95.77	1.3719
3	77.94	0.7443	78.31	0.7478
4	67.60	0.4841	67.92	0.4864
5	60.55	0.3469	60.84	0.3486
6	55.36	0.2643	55.62	0.2656
7	51.32	0.2100	51.57	0.2110
8	58.08	0.1722	48.31	0.1730
9	45.39	0.1444	45.61	0.1452
10	43.13	0.1235	43.33	0.1241
11	41.18	0.1072	41.37	0.1078
12	39.48	0.0932	39.69	0.0947
13	37.99	0.0837	38.17	0.0841
14	36.66	0.0750	36.83	0.0754
15	35.46	0.0677	35.63	0.0681
16	34.39	0.0616	34.55	0.0619
17	33.41	0.0563	33.57	0.0566
18	32.51	0.0517	32.67	0.0520
19	31.69	0.0478	31.84	0.0480
20	30.93	0.0443	31.08	0.0445

Table 4. Klystron 5K70SG: 20 kW at 18 kV

Beam voltage, kV	Frequency			
	2.110 GHz		2.120 GHz	
	Phase length, rad	PPF, deg/V	Phase length, rad	PPF, deg/V
1	184.29	5.2794	185.16	5.3044
2	130.50	1.8693	131.12	1.8781
3	106.70	1.0190	107.21	1.0238
4	92.55	0.6628	92.99	0.6660
5	82.90	0.4750	83.29	0.4772
6	75.78	0.3618	76.14	0.3636
7	70.26	0.2876	70.60	0.2889
8	65.82	0.2357	66.13	0.2368
9	62.15	0.1978	62.44	0.1988
10	59.04	0.1691	59.32	0.1699
11	56.37	0.1468	56.64	0.1475
12	54.05	0.1290	54.31	0.1297
13	52.01	0.1146	52.25	0.1151
14	50.19	0.1027	50.42	0.1032
15	48.55	0.0927	48.78	0.0932
16	47.08	0.0843	47.30	0.0847
17	45.74	0.0771	45.95	0.0774
18	44.51	0.0708	44.72	0.0712
19	43.38	0.0654	43.59	0.0657
20	42.35	0.0607	42.55	0.0609

As indicated in Tables 3-6, the phase length of the klystron amplifier is increased as the beam voltage is reduced.

## References

1. *Varian Associates Phase Modulation, Modulation of Klystron Amplifiers Due to Ripple on The Beam Voltage*, AEB 18, Publication 1043, May 1963.
2. *Handbook of Chemistry and Physics: Electron Physics Tables*. Forty-first Edition. Edited by C. E. Hodgman. Chemical Rubber Publishing Co., Cleveland, Ohio, 1959.

**Table 5. Klystron 5KM300SI: 100 kW at 38 kV**

Beam voltage, kV	Frequency			
	2.110 GHz		2.388 GHz	
	Phase length, rad	PPF, deg/V	Phase length, rad	PPF, deg/V
5	83.02	0.4757	93.96	0.5383
10	59.13	0.1694	66.92	0.1917
15	48.62	0.0929	55.03	0.1051
20	42.41	0.0607	47.99	0.0687
25	38.20	0.0438	43.23	0.0495
30	35.11	0.0335	39.74	0.0379
35	32.73	0.0268	37.04	0.0303
38	31.54	0.0238	35.69	0.0269
40	30.82	0.0221	34.88	0.0250

**Table 6. Klystron X3070: 450 kW at 63 kV**

Beam voltage, kV	Frequency, 2.388 GHz	
	Phase length, rad	PPF, deg/V
5	157.89	0.9046
10	112.45	0.3222
15	92.48	0.1766
20	80.65	0.1155
25	72.64	0.0832
30	66.77	0.0638
35	62.24	0.0509
40	58.62	0.0420
45	55.64	0.0354
50	53.13	0.0304
55	50.99	0.0266
60	49.14	0.0235
63	48.14	0.0219

## G. 500-kW Klystron Development, C. P. Wiggins

A broad-band, fixed-tuned klystron having a 500 kW RF output is being developed for use as the final power amplifier in the mark III, 500 kW DSN transmitting system. The klystron has a center frequency of 2.110 GHz and an electronic bandwidth of 25 MHz total at the 1 dB points. This will allow support of space projects operating in the manned space frequency band as well as in the DSN band. Fixed tuning will simplify operation and

improve the reliability of the klystron. The minimum saturated gain of 46 dB allows use of an off-the-shelf traveling-wave tube for a buffer amplifier.

The contractor has completed the initial design and verified the required bandwidth by computer analysis. The first three cavities will have factory-set trimming-adjustment tuners that will not be accessible to the user. Since tuners employ corrugated diaphragms or bellows to transmit motion through the vacuum wall, consideration must be given to the attendant cooling problems and metal fatigue due to a number of tuning cycles. Elimination of tuners on the last two cavities (operating at high power levels) reduces the cooling problem; restriction of tuning to factory setting will eliminate bellows failure from fatigue.

It is standard practice to prove the design by cold testing models of critical parts either at low power or with pulses. Models of the cavities and output coupler are being fabricated. Berillium-oxide windows are on order for cold testing.

Some of the components to be used in the new klystron, including the electron gun and collector, were developed for the 450 kW, 2.388 GHz tunable klystron now in use at Venus DSS. Fabrication of these components is in process.

Major components of the high-voltage power supply and cooling system to be used with this klystron are on hand at Mars DSS awaiting the construction of concrete foundations, trenches, and a transformer vault.

The new klystron will be physically longer than the 2.388 GHz unit since it will operate at a lower frequency and have the same electrical length. The klystron cabinet frame design has been modified by JPL to accommodate the longer tube. The rigidity of the re-designed cabinet has been tested by computer program to assure that excessive external loads will not be transmitted to the waveguide window of the klystron. It is expected that a contract will be awarded for completion of design details and fabrication of a cabinet to house the new klystron.

Subsystem testing is scheduled for the second half of 1969 in order to support a January 1, 1970 operational readiness date. The new klystron will first be used in support of the solar occultation portion of the *Mariner* Mars 1969 mission.

## H. Traveling-Wave Tube Amplifier, B. W. Harness

The new 500 kW klystron, fixed tuned at 2.110 GHz  $\pm 12.5$  MHz at 1 dB points, will require at least 10 W of drive at the input connector of the klystron. Since the power available to any klystron from the DSN exciter is less than 1 W, it is obvious that the klystron drive power must be increased.

One method of increasing drive power is to add a traveling-wave tube amplifier (TWTA) to the exciter drive chain. The addition of a 20-W TWTA to the exciter chain will increase the drive at the klystron to the required 10 W.

Since there was some concern that addition of a TWTA would contribute to the incidental phase modulation (IPM) of the 500 kW transmitter subsystem and degrade the transmitted spectrum, extensive tests were conducted on three different TWTA's. All were 20-W tubes manufactured by Watkins Johnson Laboratories.

The IPM produced by a TWTA covers spurious components in the output signal of the amplifier. Since the IPM produced by a TWTA is not expected to exceed 2 deg p-p, IPM measurement presents a problem.

A sensitive device for IPM measurement is described in SPS 37-25, Vol. III, pp. 31-33 and shown in Fig. 7. The

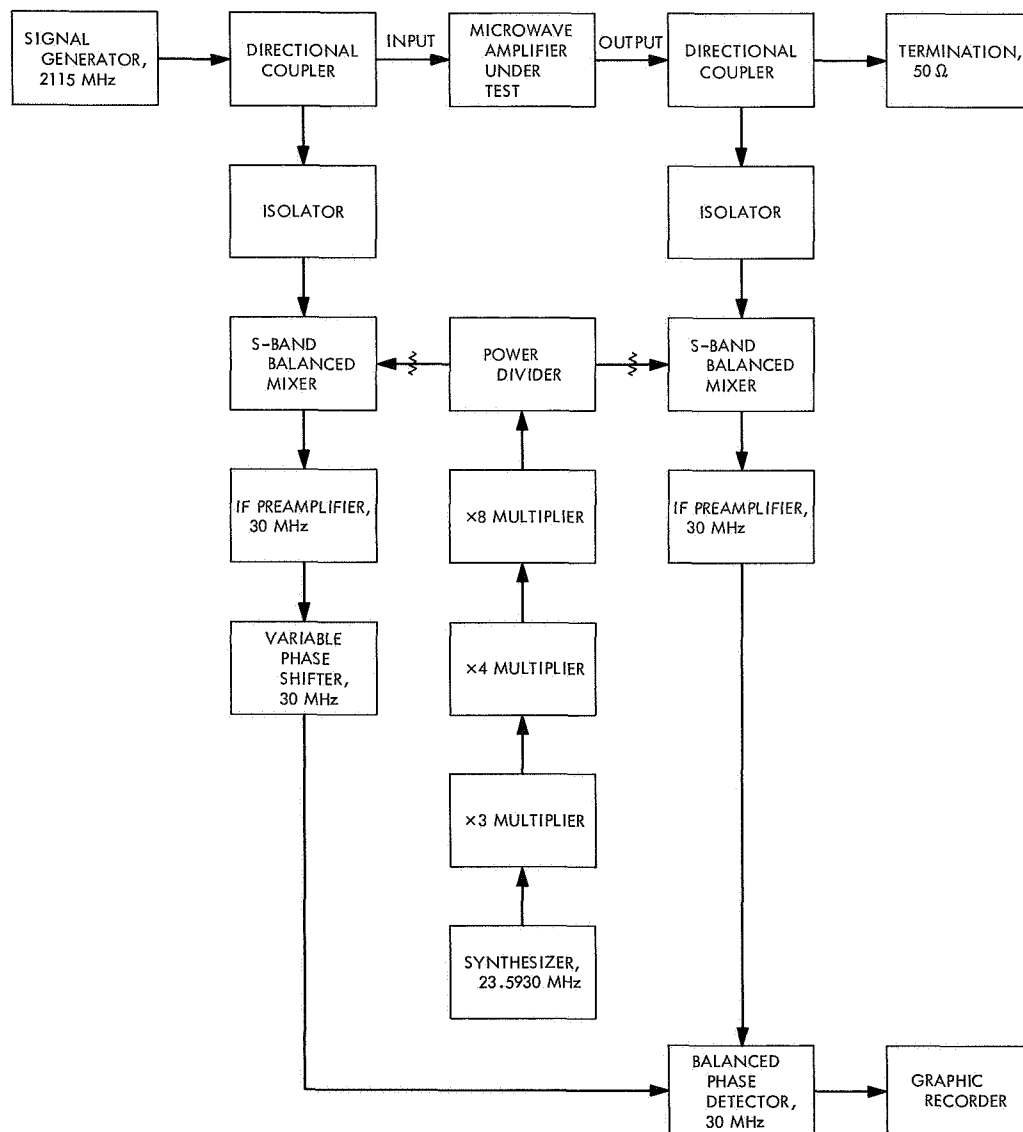


Fig. 7. IPM test unit

residual noise instability of the circuit is 0.045 deg p-p. A common local oscillator supplies two coaxial balanced mixers. A portion of the input signal to the microwave amplifier under test is coupled into one mixer through a directional coupler. Similarly, a part of the output of the device under test is applied to the other mixer. The two signals are heterodyned to 30 MHz, amplified, and compared in a phase detector. The phase shifter serves to calibrate the measurement device and to zero-out fixed phase shifts in the system. The output of the detector is fed into a Sanborne recorder.

The results of the IPM tests of the three TWTAs are displayed in Table 7 and Figs. 8, 9, 10, and 11. The (a) portion of each figure shows a graphic recording of the residual instability of the measuring system when the TWT drive signal was supplied to both mixers simultaneously. The (b) portion of each figure presents the IPM of the TWT.

**Table 7. IPM test results of three 20-W TWTAs**

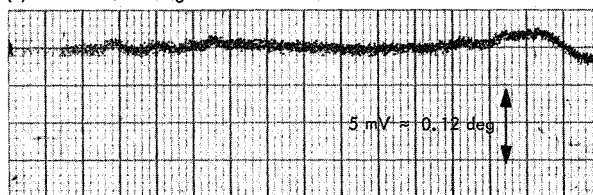
TWT	Residual phase modulation, <sup>a</sup> deg p-p	IPM, <sup>b</sup> deg p-p	Fig. Ref.
274-1 (S/N 31)	0.024	0.14	8
274-1 <sup>c</sup> (S/N 31)	0.096	0.29	11
274-1 (S/N 29)	0.048	0.14	9
274-6 (S/N 3)	0.048	0.14	10

<sup>a</sup>IPM test unit using drive signal of TWT under test.

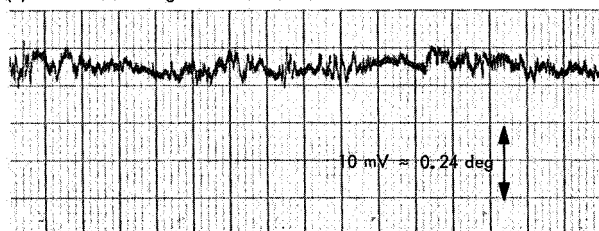
<sup>b</sup>Including the residual IPM.

<sup>c</sup>Including 20-ft signal cables.

(a) IPM = 0.024 deg PEAK-TO-PEAK

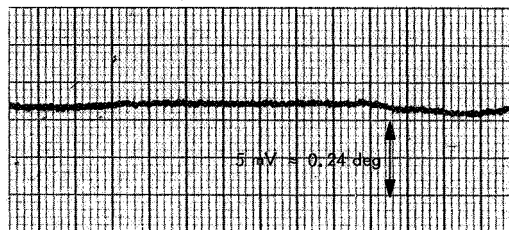


(b) IPM = 0.14 deg PEAK-TO-PEAK

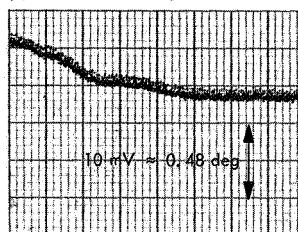


**Fig. 8. IPM test results for TWT 274-1 S/N 31**

(a) IPM = 0.048 deg PEAK-TO-PEAK

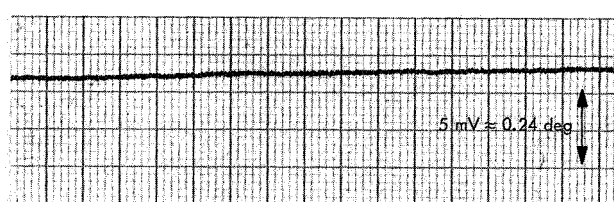


(b) IPM = 0.14 deg PEAK-TO-PEAK

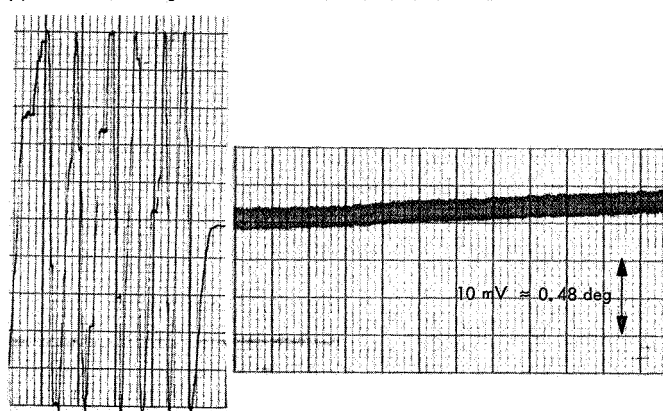


**Fig. 9. IPM test results for TWT 274-1 S/N 29**

(a) IPM = 0.048 deg PEAK-TO-PEAK



(b) IPM = 0.14 deg PEAK-TO-PEAK CALIBRATION CURVE



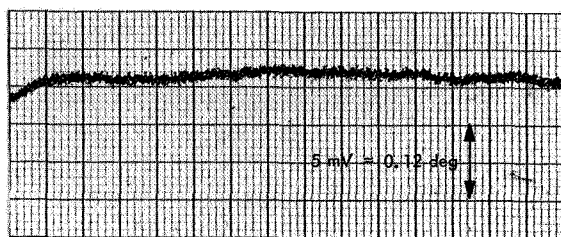
CALIBRATION DATA, deg

0.50 V = 180.0	0.05 V = 12.0
0.20 V = 48.0	0.02 V = 4.8
0.10 V = 24.0	0.01 V = 2.4

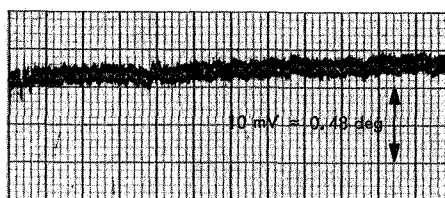
**Fig. 10. IPM test results for TWT 274-6 S/N 3**

The S-band drive signal to two of the TWTAs was obtained from a crystal voltage-controlled oscillator and a spacecraft multiplier chain. The drive to the other TWT

(a) IPM = 0.024 deg PEAK-TO-PEAK



(b) IPM = 0.29 deg PEAK-TO-PEAK



**Fig. 11. IPS test results for TWTA 274-1 S/N 31 with 20-ft signal cables attached**

was supplied by a similar chain except that a 10-W TWTA of the type flown in *Mariner IV* was included in the drive chain.

Some conclusions drawn from the results of the TWTA tests are as follows:

- (1) The worst-case IPM for the tested TWTAs was 0.29 deg p-p.
- (2) The best IPM results obtained were 0.14 deg p-p.
- (3) Although the conditions for IPM measurement were ideal, since the tests were conducted in an environmental laboratory, the IPM contribution of a TWTA should not degrade the spectral purity of the present DSN transmitted up-link signal.

## I. Equipment Maintenance Facilities, R. Smith

A worldwide network of maintenance facilities has been established to perform the calibration, repair, and replacement of DSIF equipment required by the DSSs to assure complete and accurate collection of tracking data. The attainment of a high degree of accuracy and repeatability of measurements performed at different times and places in the DSIF is accomplished by calibrating the equipment to known and accurate standards. The validity of the accuracies is based on the principle of record traceability, which directly relates equipment calibration to these standards.

The basic maintenance function includes the following two categories:

- (1) Preventive — periodic service to forestall normal equipment wear or performance degradation or to verify performance level. Includes calibration, lubrication, and adjustment of unit.
- (2) Corrective — nonperiodic service to correct equipment damage, failure, or loss of adequate performance. Includes repair or replacement of unit.

The network of maintenance facilities is divided into three echelons (Table 8): class-A depot, class-B depot, and area maintenance facility. There is one class-A depot (Goldstone DSCC) that services three class-B depots (Goldstone, Canberra, and Madrid DSCCs) and their associated area maintenance facilities (Cape Kennedy, Woomera, and Johannesburg, respectively). Each DSS and compatibility station is serviced either by a class-B depot or by its own area maintenance facility. Each class-B depot, in addition to servicing one or more stations, supports the area maintenance facility with which it is associated. This support includes calibration of area maintenance facility standards, distribution of documentation, control of spares, and servicing of certain subsystem equipment.

The facilities in all three echelons differ very little in organization. Each facility consists of three service departments: technical, engineering, and administrative support. As a result of their organizational and physical similarities, an area maintenance facility can be easily expanded to a class-B depot should the need arise.

**Table 8. Echelon and geographic grouping of DSIF equipment maintenance facilities**

Class-A depot: Goldstone DSCC		
Class-B depot		
Goldstone DSCC	Canberra DSCC	Madrid DSCC
Pioneer DSS	Tidbinbilla DSS	Robledo DSS
Echo DSS		Cebreros DSS
Mars DSS		
JPL Compatibility Test Area		
Area maintenance facility		
Cape Kennedy Spacecraft Compatibility Station	Woomera DSS	Johannesburg DSS

Subsequent articles will deal with the formation of the class-A and class-B depots at Goldstone DSCC, DSIF standards and traceability, and specific measurement disciplines in the DSIF class-A depot.

#### **J. Workmanship Assurance Program, R. Durham**

A workmanship assurance (WA) program is being established to provide inspection and certification support to all maintenance facilities and stations in the DSIF. Trained inspectors will be located permanently at each activity to support all installation, rework, and repair. The primary goals of the WA program are to maintain the reliability of newly certified equipment and, where possible, to improve the reliability of existing hardware.

Implementation of this program presently consists of three tasks; (1) training inspection personnel, (2) publishing documentation, and (3) writing a computer program.

A series of Scientific Research Associates tests were given to each candidate for the school and final selection of students was based on test scores and background. In February 1968, 11 students started the first 12-week training course and, upon completion, returned to their respective stations to begin the inspection work.

Since formal procedural and inspection criteria documents were not available at the start of the program, a number of interim documents were adapted to support the program until the implementation phase is completed. Preparation of the formal documentation was started in February 1968 and has continued during the past seven months. Nine of the primary documents are presently being prepared at Goldstone DSCC. The "second draft" of each document is being "use-tested."

A computer will perform routine segments of statistical data analysis for use by the entire DSIF in analyzing WA program results. Initial programming is being prepared at the Goldstone DSCC.

## IX. Development and Implementation of Technical Structures and Utilities

### A. Cebreros DSS Antenna Reflector Damage and Repair, V. B. Lobb

#### 1. General

On August 29 the reflector dish of the Cebreros DSS antenna was driven into a "high ranger" service vehicle (Fig. 1). Preliminary inspection indicated significant damage to the reflector panels and their backup structure, and minor damage to the high ranger. DSN Operations Control Center was immediately notified of the matter, and a detailed damage report was subsequently sent to JPL to facilitate planning of the repair.

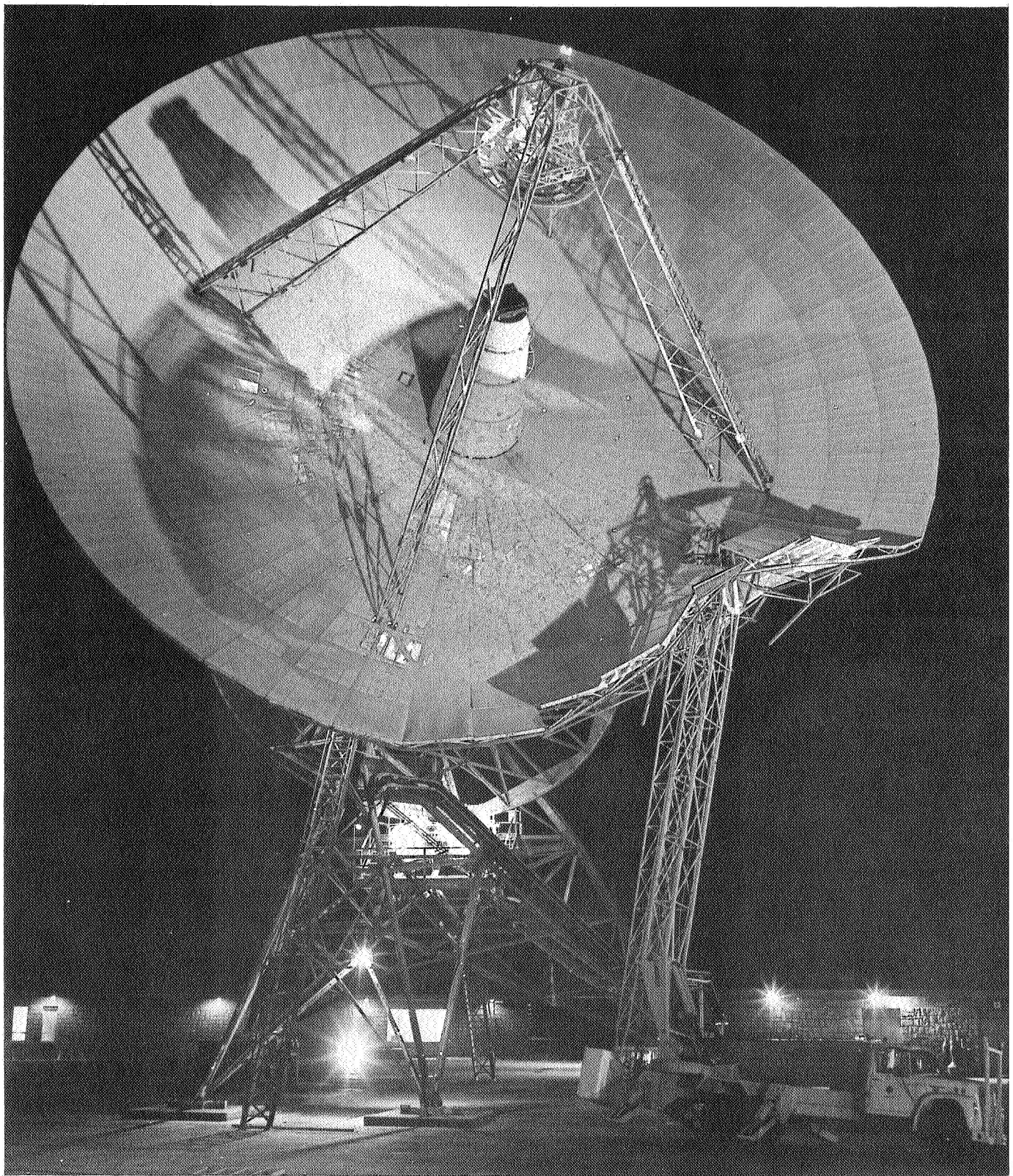
Material, tool, and personnel resources were immediately organized to accomplish repair as quickly as possible because of the *Pioneer VIII* tracking commitment and to prevent additional damage from possible high winds. Structural material was purchased in Spain; metal forming tools were supplied by a Spanish iron contractor; panel setting hardware was shipped from JPL; the work crew consisted of personnel from the Cebreros and Robledo stations and JPL, in addition to personnel from two Spanish iron contractors.

All repair and refabrication work was done on-site. All damaged panels were repaired, while some of the backup-

structure members were beyond repair and new parts were fabricated using undamaged antenna parts as templates. Damaged fasteners were replaced.

The antenna was out of service for 6 days while the damaged panels and backup structure were removed, repaired (or refabricated), and reinstalled; the backup structure was sandblasted and prime painted prior to installation of the repaired panels. *Pioneer VIII* tracking, which had been interrupted, was resumed for 3 days without the panels set to a parabola. During this time, temporary fitup bolts were replaced with the final structural fasteners. *Pioneer VIII* tracking was again stopped for the next 3 days while the cone assembly was removed, theodolite installed, surface panels set to a parabola and measured, and the cone assembly reinstalled. *Pioneer VIII* tracking was again resumed; panel edge angles were installed on an off-shift basis. Tracking was completed at the end of the following 3 days and extensive RF testing was begun.

The high ranger repair consisted of: (1) straightening one of the main cable pulleys at the knee of the boom, (2) straightening, reinforcing, and rewelding boom bracing at the knee, and (3) replacing the hydraulic control lines at the knee. The repair was completed on the first day of work.



**Fig. 1. Cebrenros DSS damaged antenna**

## 2. Damage Assessment

Initial damage assessment indicated that 32 surface panels were damaged, 12 of them beyond repair. However, an inspection of the panels after their removal from the antenna indicated that all but two of the panels could be repaired. It was later found that these two were also repairable.

Nine partial ribs and three partial rows of hoops and braces of the reflector backup structure were damaged beyond repair.

An antenna structural integrity check of the damaged area was made along a hoop line by using a dial indicator and a pipe clamped to the structure to measure elongation and hysteresis in the damaged area as the antenna was moved east to west to east. The elongation was 0.105 in., which was equivalent to a yield stress deflection in the original member. The hysteresis was 0.030 in. From this information it was concluded that limited antenna movement could be allowed during the repair operation. The hysteresis measurement also indicated that damage extended somewhat beyond the visually damaged area. This was verified when hoops which had appeared undamaged were removed and bolt holes were found to be damaged.

## 3. Material Removal and Repair

Most of the damaged material was removed by unbolting; however, the rib top chords were torch-cut, since they continued well beyond the damaged area. Some material was so severely damaged that it had to be torch-cut to be removed.

All 32 panels were straightened, including the two that initially appeared to be beyond repair. Needed matching aluminum channel sections were obtained from the Cebreros DSS storage yard.

One hundred thirty-three new pieces were fabricated. Some of the new fabricated pieces were formed (curved) and others were straight. Twelve curved pieces were made ranging in length from 15 to 23 ft. Eighty-one straight pieces were made ranging in length from 3 to 20 ft. Forty connection angles were made. The bearing bolts that were removed were sorted and saved for later reinstallation.

The newly fabricated and erected structural material in the repaired area of the antenna was sand-blasted and

primed with zinc chromate and later top-coated with an aluminum finish coat.

## 4. Reinstallation

The new pieces and removed template pieces were reinstalled with the antenna in the east service position. Temporary fitup bolts were used. These were later changed by reinstalling the once-used structural fasteners (bearing bolts). "Turn-of-the-nut" bolt tensioning method was used to ensure that proper bolt clamp force was obtained.

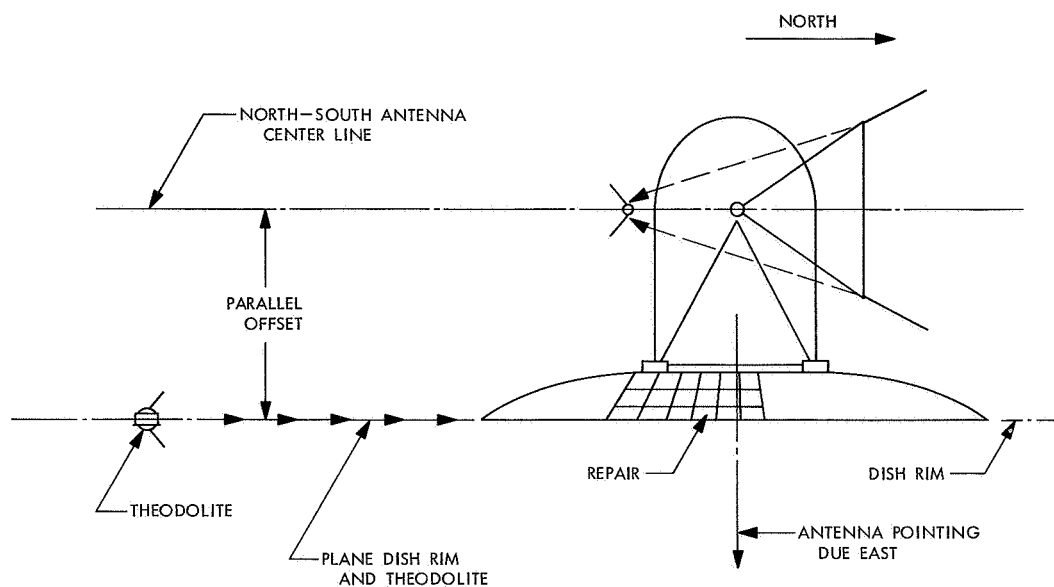
A theodolite on the ground was used to ensure that the new steel was erected to the same plane as the existing structure. The instrument was placed parallel to the antenna north-south center line, but with an offset equal to the rim of the dish offset from the polar axis. The antenna was placed in the 90-deg due-east position so that the instrument and the dish rim were in a plane (Fig. 2).

After completion of the sand blasting and prime painting, the surface panels and attachment hardware were installed with 0.25 in. of shims under the straightened and repaired panels. The installed repaired panels were drilled for installation of optical targets using metal strap gages to locate the target holes. Targets were installed, and these panels were set to a parabolic contour by shimming.

## 5. RF Performance Tests

Three antenna RF performance tests were run: (1) immediately after the accident, (2) after the structural repair was completed and the panels were installed but not set, (3) after the repaired panels were set. A summary of the results is shown in Table 1.

The antenna performance after the accident has been restored to the same level as it was before. On June 21 the reflector surface was measured, and it deviated from a true parabola by 0.0188 in. rms. After the accident, the rms deviation of the dish was 0.0349 in. The change in the rms value was caused by the rim of the dish being higher after the repair than before. The dish was repaired at the east service position, where the ribs are deflected forward by gravity. The new outside channel hoop and main ribs were erected to this plane of the dish, which is actually deflected forward. Then the balance of the hoops and bracing was installed, which held the dish with the rim in this higher position. The final total rms



**Fig. 2. Theodolite set to establish reference plane for steel placement**

**Table 1. Results of antenna performance tests**

Parameter	Performance			
	Normal	After accident	After repair	After panel setting
System temperature maser—receiver 1	$41.5 \pm 2^\circ\text{K}$	$43 \pm 1^\circ\text{K}$	$37.73^\circ\text{K}$	$39.34^\circ\text{K}$
RF boresight (with collimation tower)				
Hour angle	80.740 deg	80.764 deg		
Declination	359.196 deg	359.202 deg		
Signal level (with collimation tower transponder)	$-102 \pm 0.05 \text{ dBmW}$	$-103 \text{ dBmW}$	$-102.9 \text{ dBmW}$	$-102.7 \text{ dBmW}$
Antenna patterns in hour angle and declination (with collimation tower)				
(1) Symmetry	Very good	Reasonable	Very good	Very good
(2) Offset between error null and sum maximum	None	$\approx 0.030 \text{ deg}$	HA: none dec: $0.010 \text{ deg}$	None
Signal level	—	Aug. 28: $-157.3 \text{ dBmW}$ Aug. 30: $-157.5 \text{ dBmW}$	Aug. 26: $-156.7 \text{ dBmW}$ Sept. 15: $-156.7 \text{ dBmW}$	Aug. 26: $-156.7 \text{ dBmW}$ Sept. 18: $-156.5 \text{ dBmW}$
Angle tracking offset (with respect to predicts)				
(1) Hour angle	$-0.040 \pm 0.010 \text{ deg}$	$-0.300 \pm 0.010 \text{ deg}$	$-0.040 \pm 0.010 \text{ deg}$	$-0.040 \pm 0.010 \text{ deg}$
(2) Declination	$-0.030 \pm 0.010 \text{ deg}$	—	$-0.030 \pm 0.010 \text{ deg}$	$-0.030 \pm 0.010 \text{ deg}$

deviation is below the required specified total 0.093 in. rms. The present rms deviation is better than the minimum needed for good antenna performance at S-band frequency. No additional surface reset, new panels, or structural changes are needed or anticipated. If, in the future, a higher frequency were to be used (such as X-band) a surface reset and 32 new panels would be needed.

## **B. Pioneer DSS Antenna Mechanical Upgrade,**

*J. Carpenter and J. Carlucci*

The structural upgrade at the Pioneer DSS was implemented to attain a more stable structure, improve pointing accuracy, increase tracking coverage, and bring the antenna mechanical subsystem up to the required specification levels for the phase II GSDS configuration.

This upgrade began on July 22, 1968 and completion was scheduled for October 12; however, due to a possible manned *Apollo* moon orbit in December the completion was accelerated, and work was finished on October 5.

The upgrade work covered the following:

- (1) Addition of structural steel in critical stress areas of the antenna pedestal and bracing members in the hour-angle and declination-angle wheels.
- (2) Replacement and alignment of all drive skids and resetting of drive gears.
- (3) Replacement of all cables and cable trays.
- (4) Rebolting of complete structure with ASTM A-490 high-strength bolts.
- (5) Rerouting and replacement of all transmitter and air-conditioning coolant lines.
- (6) Reworking or replacement of all antenna-mounted equipment.
- (7) Resetting of antenna surface panels to an rms deviation of less than 0.100 in.
- (8) Optical alignment of cassegrain system.
- (9) Installation of optical targets to a gravity reference for future verification measurements of surface rms deviation.